

ENGINEERED FERRITE SUPERSTRATE  
BASED SCAN CHARACTERISTICS OF  
FABRY-PEROT CAVITY ANTENNA

BY

**FAROOQ SULTAN**

A Dissertation Presented to the  
DEANSHIP OF GRADUATE STUDIES

**KING FAHD UNIVERSITY OF PETROLEUM & MINERALS**

DHAHRAN, SAUDI ARABIA

In Partial Fulfillment of the  
Requirements for the Degree of

**DOCTOR OF PHILOSOPHY**

In

**ELECTRICAL ENGINEERING**

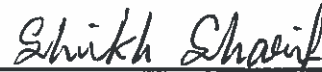
**JANUARY 2015**

KING FAHD UNIVERSITY OF PETROLEUM & MINERALS  
DHAHRAN 31261, SAUDI ARABIA

DEANSHIP OF GRADUATE STUDIES

This dissertation, written by FAROOQ SULTAN under the direction of his thesis advisor and approved by his thesis committee, has been presented to and accepted by the Dean of Graduate Studies, in partial fulfillment of the requirements for the degree of DOCTOR OF PHILOSOPHY IN ELECTRICAL ENGINEERING.

Dissertation Committee



Dr. Sheikh Sharif Iqbal (Advisor)



Dr. Mohammad S. Sharawi (Co-advisor)



Dr. Mohammad A. Alsunaidi (Member)



Dr. Ali A. Al-Shaikhi  
Department Chairman



Dr. Salam A. Zummo  
Dean of Graduate Studies



 3-5-2015

Dr. Hussain M. Masoudi (Member)



Dr. Raj Mitra (Member)



Date

*Dedicated to my parents, my sisters and my wife*

# ACKNOWLEDGEMENTS

All praises to All-mighty Allah for giving me the courage and the ability to successfully complete the assigned tasks of this dissertation. I would like to express my gratitude to King Abdulaziz City of Science and Technology (KACST) for providing the necessary funding for conducting this research. I would also like to thank King Fahd University of Petroleum and Minerals (KFUPM) in general and the Electrical Engineering (EE) department in particular for providing state-of-the-art labs for the design and specially the fabrication of the different antennas done in this work.

I am thankful to my dissertation committee for critically reviewing my thesis and providing their ever so helpful comments that resulted in this final form. Special thanks to Prof. Raj Mitra for taking time off his busy schedule and coming all the way from the US to attend the defense. My dissertation advisor, Dr. Sheikh Sharif Iqbal's contribution to this work cannot be overlooked, his innovative ideas and the countless hours of discussion has made this dissertation possible as it is. I would like to thank Mr. Amjad Awan from the EE department for helping in fabricating the PCBs as they were a vital part of this research. Last, but not the least, I would like to express my gratitude to all the RA/Lecturer-B, specifically Mr. Umar Khan, Mr. Rifaqat Hussain and Mr. Ali Al-Reshaid, for their helpful comments and suggestions in making this dissertation presentable and in its final printed form.

# TABLE OF CONTENTS

<b>ACKNOWLEDGEMENTS .....</b>	<b>iv</b>
<b>LIST OF TABLES .....</b>	<b>viii</b>
<b>LIST OF FIGURES .....</b>	<b>ix</b>
<b>ABSTRACT .....</b>	<b>xii</b>
<b>ملخص بحث.....</b>	<b>xiv</b>
<b>CHAPTER 1: INTRODUCTION.....</b>	<b>1</b>
1.1 Problem Formulation.....	3
1.2 Modeling Approach.....	6
1.3 Rationale.....	7
1.4 Scope of the Dissertation.....	8
1.5 Dissertation layout.....	10
<b>CHAPTER 2: LITERATURE SURVEY .....</b>	<b>11</b>
2.1 Background on Antennas.....	11
2.1.1 Antenna Fundamentals.....	11
2.1.2 Beam Scanning of Phased Antenna Arrays .....	13
2.2 Cavity Based Antennas.....	16
2.3 Ferrite based Antennas.....	20
2.4 Conclusion.....	22
<b>CHAPTER 3: MICROWAVE FERRITES .....</b>	<b>24</b>
3.1 Magnetic Properties of Ferrites .....	25
3.2 Motion of Electron within Magnetized Ferrites .....	29
3.3 Polder Permeability Tensor .....	32

3.4 Operating Conditions for Magnetized Ferrite Rods .....	35
3.4.1 Characteristic Equation of a Ferrite Rod with Magnetic Side-Wall .....	36
3.4.2 Operating Regions of Axially Magnetized Ferrite Rod .....	37
3.5 Gyro-Magnetic Properties of Magnetized Ferrite .....	39
3.5.1 Variation of Ferrite Cylinder Radius ( $r$ ) .....	44
3.5.2 Variation of Ferrite Cylinder Length ( $l$ ) .....	46
3.6 Conclusion .....	48
<b>CHAPTER 4: FERRITE SUPERSTRATE BASED PHASE CONTROL OF RADIATED WAVE .....</b>	<b>49</b>
4.1 Phase Properties of the Radiated Wave .....	50
4.2 Ferrite Superstrate loaded Microstrip Antenna .....	51
4.2.1 Design of Ferrite Loaded Microstrip Patch Antenna .....	51
4.2.2 Radiation Response of the Ferrite Loaded Microstrip Antenna .....	53
4.2.3 Results .....	56
4.3 Design of Ferrite Loaded FPC Excited by MPA .....	63
4.3.1 Results .....	64
4.4 Conclusion .....	67
<b>CHAPTER 5: FERRITE LOADED FPC ANTENNA EXCITED BY AN ARRAY</b>	<b>69</b>
5.1 Fabry-Perot Cavities (FPC) .....	70
5.1.1 Characterization of an FPC Excited by an RF source .....	70
5.1.2 Traditional Scanning of FPC antenna .....	72
5.2 Simulated and Measured Results .....	76
5.2.1 Beam Scanning 2- Patch FPC Antenna with Uniform Superstrate .....	76
5.2.3 Side-Lobe Suppression .....	82
5.3 Conclusion .....	85

<b>CHAPTER 6: FERRITE SUPERSTRATE WITH INTEGRATED SPLIT-RING RESONATOR .....</b>	<b>87</b>
6.1 Split-Ring Resonators (SRR) .....	88
6.2 Design of a 10 GHz Split-Ring Resonator .....	89
6.3 Single MPA with SRR Integrated Ferrite Superstrate.....	95
6.4 Ferrite Loaded FPC Antenna Array with Integrated SRRs .....	99
6.5 Performance Comparison .....	102
6.6 Conclusion.....	103
<b>CHAPTER 7: CONCLUSION.....</b>	<b>104</b>
7.1 Contribution.....	104
7.2 Future Work .....	107
<b>APPENDIX.....</b>	<b>109</b>
A. Derivation of Equation of Motion.....	109
B. Derivation of Polder Permeability Matrix.....	111
C. Characteristic Equation Derivation for Magnetized Ferrite Rod .....	112
<b>REFERENCES.....</b>	<b>129</b>
<b>VITAE .....</b>	<b>137</b>

# LIST OF TABLES

Table 1. Beam scan and maximum gain as a function of the magnetizing field – one biased ferrite rod only.....	56
Table 2. Beam scan and maximum gain as a function of the magnetizing field – both ferrite rods biased. ....	57
Table 3. Comparison of the measured HPBW and directivity with $H_{01} = H_{02} = 0$ .....	62
Table 4. Radiation characteristics comparison for the three different MPA designs. ....	65
Table 5. Maximum directivity and beam scan for $H_{01} = 0$ variable $H_{02}$ . ....	96
Table 6. Beam scan and maximum directivity values for the 2-Patch FPC antenna with integrated ferrite superstrate with varying $H_{02}$ and $H_{01} = 0T$ . ....	100
Table 7. Performance comparison of the different FPC configurations. ....	102

# LIST OF FIGURES

Figure 1. Side view of an FPC antenna.....	4
Figure 2. Array antenna designed and fabricated in reference [16] (a) Top view, (b) bottom view.....	14
Figure 3. FP etalon with multiple reflections between partially reflecting cavity [33]....	17
Figure 4. 2-element miniaturized MIMO antenna over a ferrite substrate. ....	20
Figure 5. Schematic representation of B-H curve for diamagnetic and paramagnetic materials. ....	27
Figure 6. Graphical representation of magnetic moment of atoms for (a) paramagnetic, (b) ferromagnetic, (c) anti-ferromagnetic and (d) ferrimagnetic materials – the direction of the arrow indicates the direction of the magnetic moment and the length indicates its magnitude. ....	28
Figure 7. Spinning electron under the influence of an external magnetizing field, $H_0$ ....	29
Figure 8. Mode chart for the Y220 ferrite cylinder with $R = 3\text{mm}$ , $M_s = 155 \text{ kA/m}$ , $\Delta H=10 \text{ Oe}$ and $\epsilon_r=15.4$ . ....	37
Figure 9. $\beta(\text{rad/sec})$ – $f$ curve for a fixed external magnetizing field of $200 \text{ kA/m}$ for an axially magnetized Y220 ferrite rod with $\epsilon_r=15.4$ , $M_s=155.181 \text{ KA/m}$ and $R=3\text{mm}$ . ....	38
Figure 10. $\beta(\text{rad/sec})$ – $f$ curve for a fixed external magnetizing field of $200 \text{ kA/m}$ for an axially magnetized Y220 ferrite rod with $\epsilon_r=15.4$ , $M_s=155.181 \text{ KA/m}$ and $R=3\text{mm}$ . ....	39
Figure 11. HFSS simulation model for setup 1 with ferrite cylinder inside a $10 \text{ GHz}$ waveguide (a) Side view and, (b) Cross-sectional view. ....	40
Figure 12. HFSS simulation model for setup 2 - ferrite rod in free space between waveguides. ....	41
Figure 13. Magnitude of transmission ( $S_{21}$ ) and reflection ( $S_{11}$ ) coefficients for the Waveguide.....	41
Figure 14. Magnitude and phase of the transmission coefficient for a rectangular waveguide, (a) case 1 – ferrite cylinder inside the waveguide, (b) Case 2 – ferrite cylinder in free-space.....	43
Figure 15. Transmission coefficient ( $S_{21}$ ) for a ferrite loaded waveguide (a) Magnitude and (b) Phase - for ferrite cylinder having fixed length, $l = 20\text{mm}$ and variable radius, $r$ . ....	45
Figure 16. Transmission coefficient ( $S_{21}$ ) for a ferrite loaded waveguide (a) Magnitude and (b) Phase - for ferrite cylinder having fixed radius, $r = 3\text{mm}$ and variable length, $l$ . ....	47
Figure 17. E-field phase distribution for different directions of the main beam for a 2-element PAA. ....	51
Figure 18. Magnetized ferrite loaded patch antenna (non-FPC) (a) Top view, and (b) Side view. ....	52
Figure 19. Simulated reflection characteristics of loaded and simple microstrip patch antenna (MPA).....	53

Figure 20. Amount of beam scan (degrees) and the maximum gain for variation in (a) $d_f$ (b) $h_f$ (c) $h$ and (d) $x_f$ , dotted green line for gain and solid blue line for beam scan angle.....	54
Figure 21. $E_y$ phase distribution on the radiated signal just above the MPA for different beam scan angles.....	57
Figure 22. Simulated broad side radiation patterns of the ferrite loaded MPA with variable biasing conditions.....	58
Figure 23. Fabricated 10 GHz single MPA with ferrite superstrate, (a) with biasing coils and (b) with Styrofoam packing.....	59
Figure 24. Simulated and experimental $S_{11}$ responses of the ferrite loaded MPA.....	59
Figure 25. 2D radiation pattern measurement setup for the designed antennas.....	60
Figure 26. Comparison of measured and simulated 2D radiation patterns (a) $\theta=90^\circ$ for $H_{01}=H_{02}=0$ (b) $\theta=64^\circ$ for $H_{01}=0$ and $H_{02}=0.19T$ and (c) $\theta=118^\circ$ for $H_{01}=0.19T$ and $H_{02}=0T$ .....	62
Figure 27. FPC filled with magnetized ferrite rods excited by a 10 GHz MPA, (a) Top view, and (b) Side view.....	63
Figure 28. Simulated reflection responses of magnetized ferrite loaded FPC and ferrite superstrate loaded (non-FPC) 10 GHz MPA.....	64
Figure 29. Simulated radiation patterns for maximum beam scans for the magnetized ferrite loaded FPC and the ferrite loaded 10 GHz MPA (a) $H_{01}=0$ and $H_{02}=0.19T$ , (b) for $H_{01}=0.19T$ and $H_{02}=0T$ , and (c) $H_{01}=0$ and $H_{02}=0$ .....	66
Figure 37. Ferrite loaded FPC (a) $E_y$ magnitude along the observation line (b) $E_y$ phase along the observation line.....	79
Figure 38. Simulated radiation patterns for the ferrite loaded FPC antenna for different biasing fields.....	80
Figure 39. Measured S-parameters for both elements of the thinned 2-patch antenna array.....	80
Figure 40. Normalized measured radiation patterns for the FPC excited by thinned 2-patch antenna array.....	81
Figure 41. Snapshot of the fabricated ferrite loaded FPC excited by a thinned 2-patch antenna array with (a) Styrofoam packing, and (b) only biasing coils of the two ferrite rods.....	81
Figure 42. Schematic of an FPC antenna with air-ferrite and stepped dielectric superstrate layers.....	82
Figure 43. Parametric sweeps for the selection of stepped superstrate dimension, $L_{d1}$ , when $H_2 = 150$ kA/m (a) Maximum directivity and beam scan and (b) Maximum SLL and beam scan.....	83
Figure 44. Improved simulated radiation patterns of the FPC antenna with tapered dielectric superstrate, (a) unbiased ferrite and (b) ferrite biased with external magnetizing field of $H_2 = 200$ kA/m.....	85
Figure 45. A single SRR unit-cell with an equivalent LC circuit representation.....	88
Figure 46. Schematic of double ring based SRR with $Gap_o = 0.3mm$ , $Gap_i = 0.3mm$ , $L_{out} = 2mm$ , $L_{in} = 1.5mm$ , $d = 0.15mm$ , $T_{in} = 0.2mm$ and $T_{out} = 0.1mm$ .....	90
Figure 47. Simulated transmission characteristics, $S_{11}$ and $S_{21}$ , for the SRR.....	91
Figure 48. Simulated permeability for the SRR unit-cell over a frequency sweep.....	92

Figure 49. Simulation setup for SRR integrated ferrite rods excited by plane waves (a) SRR configurations, C1 and C2, and (b) Two simulations scenarios; senario 1 – same SRR configuration C1 on both sides of the ferrite rod, senario 2 – different SRR combinations on both sides. ....	93
Figure 50. Simulated transmission characteristics for the different SRR configurations (a) magnitude, and (b) phase. ....	94
Figure 51. HFSS simulation models for 10 GHz MPA with superstrate comprising of two ferrite rods with integrated SRRs at $h = 2\text{mm}$ (a) case 1 - single SRR per side, and (b) case 2 - two SRRs per side of each ferrite rod. ....	95
Figure 52. Simulated S11 response for both cases of the MPA with SRR integrated ferrite rods. ....	97
Figure 53. Simulated 2-D directivity patterns for the E-plane for maximum beam scan for case 1 – one SRR per side of the ferrite rod, and (b) case 2 – two SRRs per each side of the ferrite rod. ....	98
Figure 54. Simulated E-plane directivity patterns for maximum beam scan for case 2 – two SRRs per each side of the ferrite rod. ....	98
Figure 55. HFSS simulation models for the 2-patch FPC with SRR integrated ferrite superstrate, (a) Case 1- single SRR on each side, and (b) Case 2 – two SRRs on each side of both ferrite rods. ....	99
Figure 56. Simulated 2-D radiation patterns for FPC with SRR integrated ferrite rods (case 1) for no beam scan and maximum beam scan conditions. ....	101
Figure 57. Simulated 2-D radiation patterns for FPC with SRR integrated ferrite rods (case 2) for no beam scan and maximum beam scan conditions. ....	101

# ABSTRACT

**FULL NAME OF STUDENT:** FAROOQ SULTAN

**TITLE OF STUDY:** ENGINEERED FERRITE SUPERSTRATE BASED SCAN  
CHARACTERISTICS OF FABRY-PEROT CAVITY ANTENNA.

**MAJOR FIELD:** ELECTRICAL ENGINEERING

**DATE OF DEGREE:** JANUARY 2015

In radars and wireless communication devices, phased array antennas are widely used to steer the direction of the main beam. Typically, array of radiating patches with progressively phased excitation are used to realize beam scan, resulting in complex antenna structures.

In this dissertation, two different techniques to scan the main beam of a Fabry-Perot cavity (FPC) antenna without using phased excitation signals are presented. These alternative scanning mechanisms use a multilayered dielectric-ferrite superstrate to control the E-field distribution of the radiation path. Low-loss operating regions of the ferrite rods are analytically identified from the characteristic equation and are used in the simulations and measurements.

Using the first technique, a single 10 GHz microstrip patch antenna (MPA) is loaded with a foam-ferrite superstrate to demonstrate a measured beam scan of  $\pm 30^\circ$  for a

differential biasing field of  $H_0=0.1875$  T. By integrating an additional dielectric layer, the resulting FPC excited with an MPA shows a 1.4 dB increase in directivity at the cost of reduced scanning angle. To optimize the design, the FPC antenna with multilayer superstrate is excited with a thinned 2-patch linear array. The foam-ferrite layer of the superstrate, now with three axially magnetized ferrite rods, is optimized to control  $E_y$ -phase taper needed for the beam scan. By individually biasing the ferrite rods, the main beam of the structure is scanned up to  $\pm 12^\circ$  for a differential magnetization field of 0.182T ( $H_0=150$  kA/m). This method also reduces the side lobe level by 3.56 dB for maximum scan angle; which is important as typical FPC antenna demonstrates an increase in side lobe level with increasing scan angle.

The second technique involves integrating the ferrite superstrate with split-ring resonators (SRR) to decrease the biasing field requirements. Two different configurations, with one or two SRR integrated ferrite rods, are designed and simulated. The resulting structures demonstrate equivalent beam scans at significantly lower biasing fields with reduced cavity heights as well. Although the presented designs are not low-profile, use of low temperature co-fired ceramics (LTCC) can reduce the cavity heights and also help incorporating the biasing coils within the ferrite rods.

# ملخص بحث درجة الدكتوراه فى الفلسفة

الاسم: فاروق سلطان

عنوان الرسالة: المهندسة الفريت SUPERSTRATE خصائص المسح الضوئي يستند إلى هوائي فابري بيرو تجويف

الختصاص: الهندسة الكهربائية

تاريخ التخرج: يناير 2015

يتم استخدام المصفوفات الهوائية ذات الزوايا المتتالية بشكل شائع في الإتصالات اللاسلكية والرادارات لتوجيه الشعاع الصادر من الهوائيات بالإتجاه المطلوب. عادة ما يتم تغذية المصفوفات المستطيلة بأطوار تتزايد تدريجياً لتحقيق المسح الإشعاعي، وبسبب ذلك يكون بناء الهوائيات مرأً معقداً.

سيتم تقديم تقنيتين في هذي الرسالة لتوجيه المسح الإشعاعي للتجويف الهوائي "فابري-بيروت" (FPC) من دون التغذية المتدرجة للهوائيات. إن الطريقة لتوجيه المسح الإشعاعي سيكون عبر استخدام عازل متعدد الطبقات من مادة "فرايت" للتحكم بتوزيع الحقل الكهربائي من مسار الإشعاع. سيتم التعرف تحليلياً إلى مناطق خسارة الطاقة القليلة في أعمدة الفرايت باستخدام المعادلات الشرطية وسيتم استخدامها في نتائج برنامج المحاكاة والقياسات المخبرية.

في الطريقة الأولى، تم توصيل مصفوفة هوائية مستطيلة مبنية على نمط خطوط المايكرو (MPA) برغوة الـ"فرايت" العازلة على تردد 10 فيقاهرتز لتوضيح الإشعاع المقاس على درجات  $\pm 30^\circ$  تحت تأثير حقل مغناطيسي متحامل بمقدار 0.1875 تيسلا. إن تغذية تجويف "فابري بيروت" بواسطة هوائي مستطيل بعد إضافة طبقة عازلة أدى إلى زيادة قوة الإشعاع بمقدار 1.4 dB ولكن بالمقابل انخفض مقدار زاوية محيط المسح الإشعاعي. لتحسين الأداء، سيتم تغذية التجويف بمصفوفة هوائيات مستطيلة ذات عنصرين. إن طبقة رغوة الـ"فرايت" تتحكم بالإتجاه الصادي للحقل الكهربائي المسؤول عن تدوير إتجاه الإشعاع بمساعدة قضبان "فرايت" محورية. عند القيام بتحميل وتغذية قضبان الفرايت لوحدها بحقل مغناطيسي بمقدار 0.182 تيسلا، فإن مجموع زاوية الإشعاع يكون بمقدار  $\pm 12^\circ$ . هذه الطريقة تقلل الإشعاع الجانبي بمقدار 3.56 dB وتوفر الزاوية الأكبر لمنطقة المسح الإشعاعي، وهذه نقطة مهمة كون هوائي مصفوفة "فابري بيروت" يؤدي إلى زيادة الإشعاع الجانبي وليس تقليله كما تم إنجاز بهذه الرسالة.

التقنية لاثانية تتضمن تزويد طبقة الفرايت العازلة بحلقات رنانة مقطوعة (SRR) لتقليل الحاجة إلى الحقل المغناطيسي المساعد للتوجيه. سيتم تصميم ومحاكاة طريقتين بناء باستخدام حلقة أو حلقتين من الحلقات الرنانة المقطوعة. إن التصميم قدم زاوية مسح إشعاعي متقاربة مع الطريقة الأولى بمتطلبات تغذية مغناطيسية أقل وحجم تجويف أقل. لكن التصميمات المقدمة ليست بالحجم الصغير وتحتاج بعض الطاقة الإضافية للتشغيل بسبب الحقول الإضافية. إن استخدام طبقات السيراميك منخفض الحرارة قد يساعد على تصغير حجم التجويف ويساعد على إضافة لفائف التغذية الموصلة مع قضبان الفرايت.

## CHAPTER 1

# INTRODUCTION

In the most basic of forms, an antenna is defined as a device that transforms electrical energy into electromagnetic (EM) waves. Historically, Joseph Henry, a philosophy professor at Princeton, is considered to be the first to utilize a "wire" as a medium to capture EM energy. He initially observed that by injecting current into a wire, he could "attract" metallic needles in his basement, some 30 feet away. He also used metallic wires installed on his roof to detect lightning strikes over long distances. As interest in this field grew, numerous antenna designs emerged; vertical grounded antennas in 1875, dipole antennas and antenna arrays in 1889. In recent years, miniaturization of electronic devices motivated antenna designers to come up with compact and low-profile antennas that would fit the mobility requirements of the communication devices.

Radar systems used in civilian and military applications [1] transmit a directive microwave signal towards a moving object and analyze the reflected signal from the illuminated object to detect its position and speed [2]. Historically, the radar antennas were mechanically rotated to monitor the required azimuthal or elevation plane. As the antenna

fabrication and microcontroller technology progressed, electronic beam scanning came into being [3] [4]. The idea of electronic beam scan involves an antenna array, where the radiating elements are excited with signals having progressive phase distribution [5]. Depending on the type of the phased array antenna (linear, planar etc.), variation of the progressive phase shift steered the main beam along the azimuth or the elevation planes. Directive beam forming antennas used in recent communication devices often use microstrip arrays with patch separation distance of half a wavelength ( $d \leq \lambda/2$ ) and excitation signals with a phase progression of  $\beta$  [6]. Such a design process is considerably complicated for large antenna arrays, where realizing the phase progression requires large number of phase shifters [7]. In addition, improvement of the main-lobe to side-lobe ratio requires controlled amplitude of the patch excitation signals based on the Binomial or Dolph-Chebyshev weighting algorithm [8]. Thus, efficient design of an array feeder to implement controlled amplitude and phase of excitations of the radiating elements remains a challenge for the array antenna designer.

One popular method to overcome the feed complexity and attaining higher directivity is to use optimally excited Fabry-Perot cavity (FPC) [9] [10]. Based on the Fabry-Perot (FP) interferometer, the directivity of the FPC is improved by exciting the cavity, formed between the ground plane and the partially reflecting superstrate. Typically, thinned microstrip array, with patch separation distance of  $d > \lambda/2$ , is used to optimally excite the FPC. The FPC with simple array feeder also demonstrates limited beam scanning capabilities due to larger patch separation distance ( $d$ ) [11] [12]. Larger “ $d$ ” introduces bigger side lobes and even grating lobes (for large scan angle), when phased array technique is used to steer the main beam of the FPC.

## 1.1 Problem Formulation

Designing a working antenna system involves an understanding of the basic design parameters; gain/directivity, radiation efficiency, physical size, beam scanning abilities and side lobe levels (SLL). Ideally speaking, one would want an antenna offering maximum gain and efficiency, the least size and minimum SLLs to ensure maximum input power is radiated in the direction of interest. Thus, instead of using a single radiator, antenna arrays with multiple radiating elements are often preferred to provide higher gain and scan capabilities of the main beam. These advantages, however, come at the cost of large antenna apertures and complicated feed mechanisms that often limit their applications. Mathematically speaking the total E-field of an antenna array can be calculated by using pattern multiplication principle [5] as;

$$E(\text{Total}) = E(\text{Single Element}) \times AF \quad (1)$$

The  $AF$  is the array factor and is a function of the antenna array geometry (separation between radiating elements,  $d$ ) and the excitation phases of the radiating elements. Thus, by varying the separation between the array elements and introducing the progressive phase shift ( $\beta$ ), the direction of the main beam can be controlled. Mathematically, for an  $N$  element linear antenna array the  $AF$  is given as [5] [13]:

$$AF = \sum_{i=1}^N a_i e^{j(i-1)\psi} \quad (2)$$

$$\text{where } \psi = \frac{2\pi d}{\lambda} \cos \theta_0 + \beta \quad \text{and} \quad \beta = kd \cos \theta_0 \quad (3)$$

For a uniform phased array antenna, changing the main beam of the antenna to  $\theta_0^\circ$  requires introducing patch excitation signals with a uniform amplitude and progressive phase shift ( $\beta$ ). Typically, this phase shift is produced by integrating analog/digital phase shifters within the feed lines of the array antenna.

The concept of FPC allows the design of a highly directive antenna without complicated feed mechanism or considerably large antenna aperture. Optimal excitation of the FPC requires thinned microstrip array with element separation distance  $d \geq 0.5\lambda$ , which reduces the feed complexity but introduces SLL. When traditional phased array technique is used to scan the main beam of an FPC, the SLL becomes proportional to scan angle and can even produce grating lobes.

Fig. 1 shows the side view of a typical FPC. As the signal radiates within the cavity, it bounces between the superstrate and the ground plane multiple times. For a well-designed FPC, the multiple reflections within the cavity combine constructively and produce a stronger signal that exits the superstrate, resulting in a higher gain of the antenna in a certain direction. The cavity height,  $h$ , is a function of the radiating signal wavelength and thus tends to increase the antenna profile for low frequency designs. The radiation properties of the structure can be varied depending on the choice of the partially reflecting superstrate.

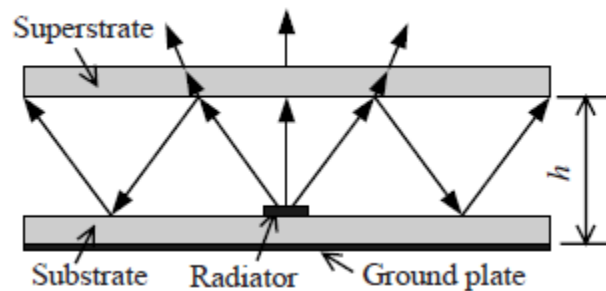


Figure 1. Side view of an FPC antenna.

As mentioned earlier, exciting an FPC with a thinned antenna array can increase the antenna gain at the cost of increased SLL. When phase array technique is used for scanning the main beam of this FPC, the already high SLL is further amplified by the coherent addition of the reflected waves within the cavity. The result is a scanned main beam with larger side lobes or even grating lobes for high scan angles. Moreover, the array feeder with integrated phase shifters, needed to realize progressive phase shift, introduces undesired coupling and signal loss.

The limitations in beam scanning and the presence of higher SLLs have kept the FPC an area of interest. An enlarged superstrate consisting of frequency selective surfaces (FSS) can even introduce beam tilting, as shown in [14]. Recently, it is demonstrated that using magneto-dielectric superstrate decreases the wavelength in the media, leading to a lower profile antenna, with thickness less than half wavelength [15].

This thesis provides a unique method to scan the main beam of an FPC by perturbing the radiated fields of the antenna instead of the traditional phased array method. Biased ferrite rods are placed inside the cavity to introduce controlled phase delay of the radiated radio frequency (RF) signal introducing phase taper needed for beam tilting. A partially reflecting superstrate with stepped dielectric constants is used to reduce the SLLs. A complete mathematical analysis is carried out to understand the interaction of the radiated EM-wave and the externally biased gyro-magnetic properties of ferrite rods. Split-ring resonators (SRRs) are integrated with the ferrite rods to provide better beam scan for reduced biasing requirements due to constructive coupling between the resonances of the SRR and the precessing dipoles of the ferrite material. Professional software (HFSS) is

used to optimize the designed antenna before fabricating the prototype. The simulated beam scanning characteristics of the FPC are also verified experimentally.

## 1.2 Modeling Approach

This work is based on the interaction of the radiated EM-wave of the thinned array and the magnetized ferrite dipoles placed within the cavity. The methodology for the design of the FPC with beams scanning properties is as follows:

- The characteristic equation of the ferrite cylinder is derived to determine the low loss operating regions where a sharp change in the insertion phase occurs with respect to changing magnetizing field ( $H_0$ ). This also identifies the lossy resonance region, where most of the energy from EM-wave is absorbed by the ferrite material.
- HFSS models of the axially magnetized ferrite rod; (i) centrally positioned within a rectangular waveguide and (ii) placed in free space, are created to simulate the effects of magnetized ferrite material on the propagating EM wave. A comparison of the analytical and the simulated cut-offs is presented to verify the excitation and meshing of the simulated model. The transmitted signal magnitude and phase is monitored as the radius and the length of the ferrite rod is varied. This gives rise to multiple transmission regions where steep changes in the signal phase are observed.
- To understand the relationship between the controlled phase delay of the radiated E-fields and the beam scanning characteristics of the antenna, a 10GHz MPA with a foam-ferrite superstrate is designed. Foam material is used to optimally position the

ferrite rods in the radiation path of the MPA. A comprehensive parametric study is done to find out the best position, dimensions and biasing of the ferrite rods that produces beam scan with minimum effect on the radiation efficiency. Once the superstrate based beam scanning of this FPC antenna is observed, an additional dielectric layer is integrated to the superstrate to improve its directivity.

- To further improve the antenna, a 2-patch thinned microstrip array ( $d = 0.8\lambda$ ) is designed to optimally excite the ferrite loaded FPC. Multiple ferrite rods are placed inside the cavity and successful beam scan is observed by providing a differential magnetic biasing to the rods. Additionally, the uniform dielectric superstrate of the FPC is replaced with a stepped dielectric superstrate to reduce SLLs while maintaining the desired degree of beam scan.
- To reduce the external magnetic biasing needed for beam scan, SRRs are integrated onto the ferrite rods of the superstrate. Two different SRR integrated ferrite superstrate are investigated.
- Fabrication and measurements of both the single patch and the 2-patch thinned antenna array are done. Using the network analyzer and the radiation pattern measurement systems, the measured results are compared to the simulated ones.

### **1.3 Rationale**

Traditional beam scan involves inducing progressive phase shift between the adjacent antenna array elements. This phase shift results in an E-field phase taper of the radiated

signal leading to a change in the main beam direction. In order to achieve beam scan without progressive phase shift, the same amount of phase taper in the radiated signal has to be produced by some other method. Biased ferrite superstrate possess the ability to introduce externally controllable phase delay to the propagating EM-wave. This concept is initially proven by placing two separately magnetized ferrite rods above a 10GHz patch antenna to introduce beam scan. This allowed the determination of the correct biasing levels, dimensions, shape and the different design parameters of the ferrite-superstrate for acceptable beam scan. Then an FPC, excited by thinned 2x1 microstrip array, is loaded with separately magnetized ferrite rods to introduce superstrate based beam scanning. Biasing the ferrite rods requires the use of coils or electromagnets to generate the DC magnetic fields ( $H_0$ ). Increasing coil size with large biasing needs often limits this type of design. In this research work, split ring resonators SRRs are designed and integrated with the ferrite material. The interaction between the magnetized ferrite material and the SRR is optimized to reduce the external magnetizing field ( $H_0$ ) needed for scanning the main beam of the FPC.

## **1.4 Scope of the Dissertation**

Ferrite material has been used in microwave devices for a number of different reasons. A detailed discussion along with references and performance specifications of a number of such devices is presented in Chapter 2. As far as ferrite applications in antennas are concerned, researchers have used ferrite substrate based antennas to achieve reconfigurable radiation patterns in addition to tunable resonant frequency and impedance bandwidth.

However, all the existing work has used phased array technique to modify the amplitude and/or phase of the patch excitation signals to realize beam scan. In addition, FPC with this beam scan technique introduces large side lobes that are proportional to scan angle.

A novel beam scanning mechanism of the FPC, different from that of phased array, is presented in this thesis. This dielectric-ferrite superstrate based beam scanning technique demonstrates low SLL for high scan angles ( $30^\circ$ ), even though the FPC is excited with thinned microstrip array. In this technique, a stepped dielectric partially reflecting superstrate is used to reduce the SLL and the FPC is loaded with axially magnetized ferrite rods to generate controlled phase delay of the radiated EM-wave required for scanning the main beam. Ansoft HFSS is used to individually simulate and optimize the FPC with thinned array exciters and the ferrite geometries before analyzing the beam scanning properties of FPC.

MATLAB simulations have been used to solve the derived characteristic equations of the related ferrite rod to identify its operating regions. Based on the operating mode, the lossy ferrimagnetic resonance region is identified and avoided to allow any transmission through the material. Initially, a single 10GHz patch antenna is loaded with a ferrite superstrate and beam scan is achieved as a proof of concept. This design is then extended to a ferrite loaded FPC, excited with a thinned array. Using the superstrate based beam scanning, an externally controllable beam scan is demonstrated with acceptable SLL. Finally, SRRs are integrated with the ferrite rods of the FPC to reduce the magnetic biasing fields needed for realizing certain beam scan. Simulated results are corroborated with experimental results.

## 1.5 Dissertation layout

This dissertation has seven chapters; Chapter 2 presents a detailed literature review on FPC, thinned antenna arrays and ferrite based antenna designs. Operation parameters like gain/directivity, impedance bandwidth, and half-power beam width (HPBW) and scan angles of the reviewed designs are mentioned.

Chapter 3 presents an investigation into the workings of the ferrite material and its interactions with the RF signals. The characteristic equation related to an axially magnetized ferrite rod is derived and related mode charts are analytically calculated.

Chapter 4 presents the design and simulation details of the beam-scannable single patch antenna using a ferrite rod based superstrate. The analytical operation regions of the ferrite rod are simulated in a controlled environment to set bench-marks for the simulations to follow. Measured and simulated antenna parameters are compared for validity.

Chapter 5 discusses the design and simulated responses of the ferrite loaded FPC, excited with thinned microstrip array. Simulated as well as measured externally controllable beam scanning characteristics of the FPC are presented.

Chapter 6 presents the design and simulated results of split ring resonators (SRRs) and their integration process with the ferrite rods. FPC loaded with the SRR integrated ferrites demonstrates lower magnetic biasing to achieve a certain beam scan.

Chapter 7 concludes the dissertation providing major achievements of the presented research and suggestions for future work.

## CHAPTER 2

# LITERATURE SURVEY

This chapter presents a literature review of the existing methods related to the directive beam scanning of a printed antenna. Section 2.1 presents the basics of antennas and the work focusing on traditional beam scanning techniques of phased array antennas. Section 2.2 discusses cavity based antenna designs, followed by Section 2.3 where the details of ferrite based antenna designs are discussed.

## **2.1 Background on Antennas**

### **2.1.1 Antenna Fundamentals**

Antennas act as an interface for propagating electromagnetic energy between the free space and the guided medium. Different types of antennas, namely wire antennas, aperture antennas, lens antennas etc. have been designed and used in literature. With the recent advancement in electronics, printed antennas have taken the center stage. These antennas are easy to design, fabricate and test, offering quick solutions to transmission needs.

Working with antennas requires a know-how of the basic design parameters [5], a review of which, is presented in this section.

Antenna gain is defined as the radiation intensity ( $U$ ) of an antenna in a given direction relative to a hypothetical lossless isotropic antenna. Mathematically, antenna gain is related to the input power ( $P_{in}$ ) of the antenna as [5],

$$Gain = 4\pi \frac{U}{P_{in}} \quad (4)$$

Peak directivity of an antenna is defined as the ratio of an antenna's radiation intensity in a given direction to its radiation intensity in all directions [5] of the far-field infinite sphere. Mathematically,

$$Directivity = 4\pi \frac{U}{P_{rad}} \quad (5)$$

where  $P_{rad}$  is the total radiated power of the antenna.

Antenna bandwidth is defined as the range of frequencies over with acceptable levels of performance can be achieved. Depending of antenna application, -6 dB and -10 dB are considered as standard when referring or calculating operational bandwidths in literature.

Radiated power is the amount of power in watts exiting an antenna. Mathematically, radiated power, in terms of the electric field,  $E$  and the magnetic field,  $H$ , over a surface is computed as [5],

$$P_{rad} = Re \left\{ \int E \times H^* \cdot ds \right\} \quad (6)$$

Incident power is the total amount of power incident on all port boundaries of an antenna structure. For a single port loss-less antenna, the incident power, in terms of the complex modal excitation  $a$ , is mathematically given as,

$$P_{incident} = |a|^2 \quad (7)$$

Radiation efficiency represents the antenna's ability to radiate any amount of accepted power,  $P_{acc}$ . Mathematically,

$$Efficiency = \frac{P_{rad}}{P_{acc}} \quad (8)$$

### 2.1.2 Beam Scanning of Phased Antenna Arrays

In traditional antenna arrays, multiple radiating elements are needed to change the direction of the main beam. The total E-field of a microstrip phased antenna array can be calculated by using pattern multiplication [5] as;

$$E(Total) = E(Single Element) \times AF \quad (9)$$

where,  $AF$  is the array factor, which is a function of patch separation distance and the progressive phase distribution of the patch excitation signal. Thus, by varying the separation between the array elements and introducing the progressive phase shift ( $\beta$ ), the direction of the main beam can be controlled. Mathematically, for an  $N$  element linear antenna array the AF is given as [5] [13]:

$$AF = \sum_{i=1}^N a_i e^{j(i-1)\psi} \quad (10)$$

where,  $\psi = \frac{2\pi d}{\lambda} \cos \theta_0 + \beta$ ,  $\theta_0$  is the direction of main beam,  $a_i$  is the amplitude of the exciting signal and  $d$  is the separation between adjacent patch antenna elements.

To maximize the array factor,  $\psi = 0$ , hence,

$$\beta = kd \cos \theta_0 \quad (11)$$

For a uniform phased array antenna, with  $a_i = 1$ , introducing a progressive phase shift requires phase shifters to be integrated with the array feeder. In reference [16], Goel presented the design of an X-band four-element microstrip array, where all the monolithic phase shifters and the radiating patches are fabricated on a single substrate. The design is really complex, as variable degrees of phase shift have been realized by integrating shunt resistors within the substrate, and external DC voltage are used to provide tuning ability. A snap shot of the fabricated antenna array is shown in Fig. 2, where  $10^\circ$  beam scan required an external voltage of 125V to be applied to the voltage divider network.

In reference [17], a coplanar waveguide continuous transverse stub (CPW-CTS) is used to steer the main beam of a 2-element antenna array by  $\pm 20^\circ$ . The dielectric layer used in this work consists of alternating layers of ferrite and  $\text{SiO}_2$  making the antenna array less lossy and providing good impedance matching. Chauraya et al. in [18] have used optically illuminated electronic band gap structures (EBG) [19] to realize phase shifter network for a 4-patch rectangular antenna array. The fabricated antenna array shows a change in the

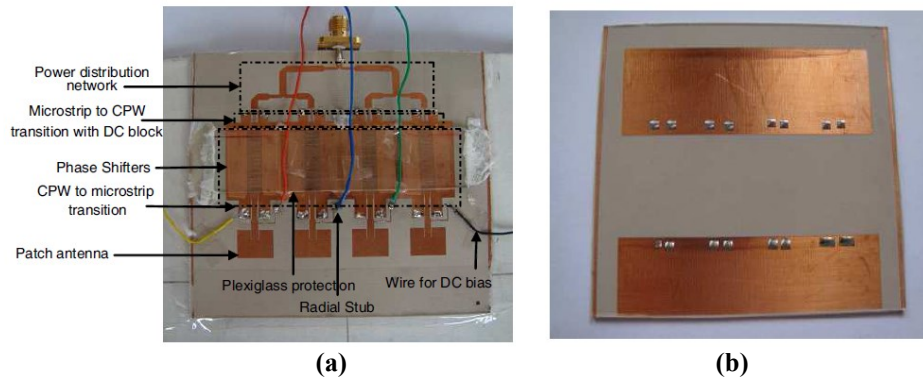


**Figure 2. Array antenna designed and fabricated in reference [16] (a) Top view, (b) bottom view.**

main beam direction by  $15^\circ$ , when the EBG based phase shifter is illuminated by light emitting diodes (LEDs). Maximum power requirements for the optical phase shifter are tested to be 22 mW at 1.65 V. Unlike the above mentioned techniques, Hu et al. in [20] have presented the design of a phased antenna array, whereby the main beam is scanned by integrating voltage control oscillators (VCOs). By adjusting the free running frequencies of the VCOs, the main beam can be scanned between  $-26^\circ$  to  $+10^\circ$  in the azimuthal plane.

A number of analog beam forming techniques involving the use of embedded resistive and reactive components are presented in the literature [21]. These designs provide beam/null scanning without the use of phase shifters. Electrically steerable passive array radiator (ESPAR) antennas, consisting of a single active element and multiple adjacent passive elements, are studied comprehensively in [22]. The reactance of the passive elements is changed using varactor diodes to induce a phase shift causing a change in the direction of the main beam. In [23], Dinger presented the design of a reactively steered adaptive array (RSAA). The presented design comprises of one radiating element along with two adjacent parasitic elements. The direction of the null (or the main beam) is steered by controlling the varactor diodes that act as the reactive terminations of the parasitic elements. A  $40^\circ$  beam scan using a 3-element ESPAR operating at 3 GHz is presented in [24]. Rectangular patches are used as the antenna elements, where the center element is active and the others are passive. Chip capacitors with pre-calculated capacitances are used to reactively load the passive elements in order to steer the main beam. Kim et al. in [25] have used 3-element circular ESPAR antenna array, which provides a wider half power beam width (HPBW) and scan angles of  $\pm 37^\circ$ . As opposed to the cited work on antenna

arrays, Cao et al. in [26] achieved beam scan using a single patch antenna by defecting the ground plane. A complementary split ring resonator (CSRR) is placed in the ground plane to change the E-field phase, causing the main beam to change direction.

The above mentioned designs constitute only a fraction of all the studies available on beam steering of phased antenna systems. Since the work presented in this thesis involves the design of a linear array antenna, all the references cited so far involve beam scanning in one plane (usually the E-plane). Multidirectional beam steering involving planar arrays is also investigated by researchers in [27] [28] [29] [30] [31]. For the sake of simplicity and the absence of multidirectional beam scanning in our work, the design details of planar phased array antennas is not included.

A large number of the linear phase antenna array systems cited above use phase shifters to attain the required progressive phase difference between the radiating elements. The phase shifter-less designs found in literature either use passive elements (ESPARs) or VCOs to change the E-field distribution of the radiating elements and cause the main beam to change direction.

## **2.2 Cavity Based Antennas**

C. Fabry and A. Perot devised an interferometer in 1899, which became known as the Fabry-Perot (FP) interferometer or the FP etalon. The FP resonator was developed for optical systems and comprises of a cavity formed between two partially reflecting surfaces [32]. The light entering the etalon is reflected multiple times between the two mirrors. The light passes through only when the multiple reflected waves combine in-phase and the

constructively coupled light beam becomes strong enough to pass through the other surface of the etalon. A diagram indicating the working of the FP etalon is shown in Fig. 3.

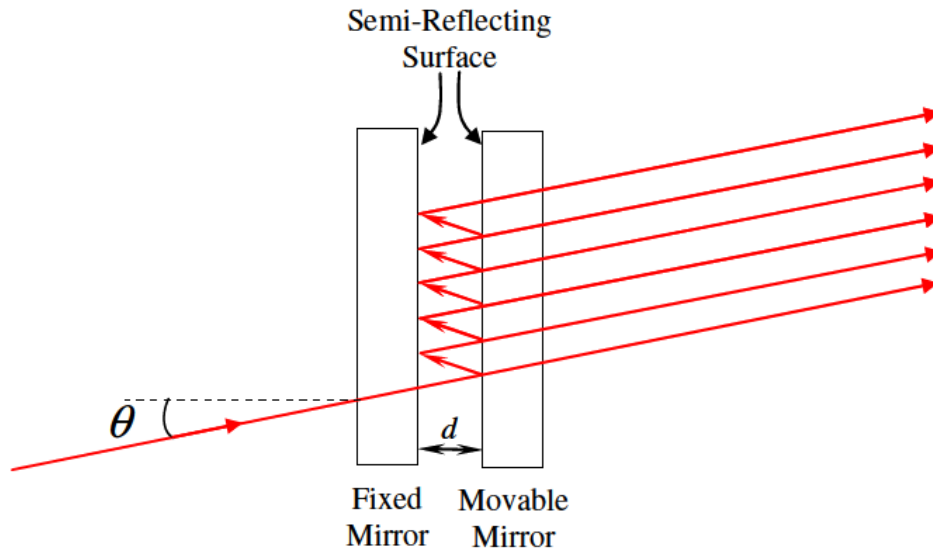


**Figure 3. FP etalon with multiple reflections between partially reflecting cavity [33].**

The concept of FPC was first used with antennas by Trentini [34]. He demonstrated an increase in directivity when a partially reflecting plate was placed in the radiation path of an open ended waveguide. Since Trentini, interest in the application of FP cavities for microwave applications has increased considerably. In addition to directivity enhancement, FPCs are also used for multi-frequency resonance. Fig. 1 shows a schematic side view of an FPC. The top layer, known as the superstrate, can be specially designed to achieve the different purposes mentioned earlier. Based on the leaky wave theorem, gain enhancement using a dielectric superstrate is proposed in [35], where mathematical relationships are derived to explain the radiation mechanism through superstrate. In [36], complete mathematical analysis of the FPC is performed by Liu for different boundary conditions. Directivity enhancement by using a uniform permittivity dielectric superstrate has been presented in [37], where an enhancement of 10 dB was achieved as compared to an ordinary

patch working at 3 GHz. A further increase in directivity by 1.8 dB was achieved by using a graded-index permittivity superstrate. The FPC design presented in [38] is excited by a 7-patch array and used a superstrate layer consisting of dipole unit-cells. The results demonstrated an increase of 3.16 dB in the directivity of the main beam in the E-plane.

The FPC does provide an enhancement in the directivity of the antenna but at the cost of the antenna bandwidth. Hence, enhancing the directivity leads to extremely narrow bandwidth antennas, which remain very sensitive to the input system frequency. The trade-off between the directivity and the bandwidth suggests the usage of sparse antenna arrays to provide a moderate increase in directivity, while preserving the operational bandwidth [39] [40] [41]. Sparse or thinned antennas consist of lesser radiating elements with larger inter-element spacing, which leads to simpler feed networks and lesser mutual coupling between radiators. Thus, optimal excitation of an FPC using a thinned or sparse microstrip linear array can considerably improve the antenna performances.

Using traditional phased array technique, the main beam of an FPC antenna can be steered or scanned by exciting the cavity with uniform microstrip array with progressive patch excitation phases ( $\beta$ ). In the literature, Guo et al. have used an FPC array to scan the main beam in the E-plane [42]. Varactor diodes are integrated into the ground plane to obtain a beam scan of  $35^\circ$ , when powered between 4V to 18V. Attia et al. in [43] have used a single patch antenna to excite an FPC with multilayer superstrate. He has scanned the main beam of the FPC by unevenly positioning the superstrate. A high dielectric constant superstrate, when physically moved along the E-plane of the antenna, caused the main beam to steer  $\pm 12^\circ$ . Liu et al. in [44] have used tapered superstrate layers to enhance the operational bandwidth of the antenna array by 7.9 %. In another design [45], tapered

dielectric superstrate is used to design an ultra-wideband UWB antenna to excite the FPC. This, in addition to Meta-material based superstrate, produced a directive beam scan with limited scan angle. A meta-material based double-sided superstrate has been employed in [46] to achieve beam scan. The superstrate comprises of a capacitive grid on one side and an inductive grid on the other. The simulation and measurement results provided in the paper show a sharp beam scan with optimized superstrate dimension.

Apart from FPC based antenna designs, a number of cavity based antennas have been presented in literature that use the concept of cavity resonance. Foroozesh et. al in [47] have presented the design of a highly reflective superstrate layer comprising of periodically placed patches. A dipole antenna has been used to excite this cavity and a complete analysis of the design and performance specifications of the said antenna has been done. The designed antenna demonstrated an increased directivity of up to 20.07 dBi for the different designs operating between 8.2 GHz to 8.9 GHz. The sole purpose of using a superstrate in this work was to enhance the directivity of the antenna while providing frequency selective operation. Ning et. al in [48] have presented the design of a bow-tie antenna operating in the terahertz frequency range of 0.996 THz and 1.177 THz. By designing and placing a silicon based hemispherical lens superstrate over the bow-tie antenna, a directivity enhancement of 2 dBi.

## 2.3 Ferrite based Antennas

Magnetized ferrite has been used as a substrate for a number of antenna designs found in literature. The high magnetic permeability of unbiased ferrite leads to smaller patch antenna dimensions resulting in antenna miniaturization. Magnetized ferrite can be used to provide beam steering, frequency tuning, gain and bandwidth enhancements and switching ability [49].

Lee et. al in [50] and [51] have used the ferrite substrate for miniaturizing microstrip antennas. A 2-element multiple-input multiple-output (MIMO) antenna specifically designed for LTE applications has been miniaturized in [50]. The required separation between the radiating elements for MIMO is achieved by using a high dielectric constant and high permeability magnetic superstrate. A snap shot of the designed antenna is provided in Fig. 4. The primary use of the ferrite substrate in this design was for antenna miniaturization. Hence the substrate has been kept unbiased resulting in no tuning of the operating characteristics. The results show a slight decrease in the gain of the radiators due to the losses associated with the ferrite material.

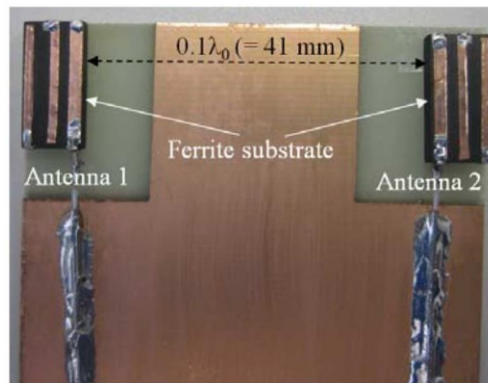


Figure 4. 2-element miniaturized MIMO antenna over a ferrite substrate [50].

Using the same concept of miniaturization, a chip antenna has been presented in [51]. The authors have shown that by inherently high ferromagnetic resonance frequency provided by hexaferrites, even low permeability values can be used to achieve miniaturization. Kitra et. al in [52] have used unbiased ferrite substrates to realize small antennas suitable for handheld devices. In addition, an 88% reduction in the SAR has been observed by employing ferrite substrate. Placement of a thin ferrite layer above a printed monopole antenna has been shown to provide tunable impedance bandwidth in [53]. The authors have demonstrated a 200% increase in the impedance bandwidth by placing a Ba-Co ferrite film above the patch surface of a monopole antenna operating in the X-band.

Sigalov et. al in [54] have used tiny ferrite disks inside the substrate of a single MPA to introduce frequency tunability along with polarization adjustment. It has been shown that by changing the dimensions and the magnetic biasing of the ferrite disks, different designs show frequency tunability of between 2.8 GHz to 3.2 GHz. A number of other antenna designs [55] [56] have also used magnetized ferrite disks inside the substrate to realize frequency tunability while providing complete mathematical analysis of the radiated fields of the designed structure.

One of the earliest designs incorporating beam scanning using ferrite superstrate was presented by Henderson et. al in [57]. The design used a ferrite slab placed directly over the single radiating patch antenna. A beam scan of up to  $15^\circ$  was achieved when the ferrite superstrate was biased. Additionally, the authors also noted that placing the ferrite slab directly above the radiating patch degraded the antenna gain unless the ferrite was biased. Thus, an initial biasing was necessary to ensure the antenna gain was not affected. A 2-patch antenna array with the feed network fabricated on ferrite is presented in [58]. Biasing

the ferrite substrate of the feeding network changes the phase of the feed signal, resulting in a progressive phase shift fed to the radiating elements. A beam scan of up to  $40^\circ$  is achieved using this design.

More recently, 3D ceramic substrates called low-temperature co-fired ceramics (LTCC) [59] have come into use for antenna applications [60]. Shamim et. al in [61] have presented the design of single patch antenna based on an LTCC ferrite substrate. Use of the LTCC enables embedding the biasing coils inside the substrate, resulting in a 95% decrease in the dimensions of the antenna. The authors in [61] have used ferrite to tune the frequency of the designed antenna.

## **2.4 Conclusion**

Among the numerous beam scanning antennas found in literature, majority of the techniques involve traditional phased array mechanism. The issue of integrating phase change circuitry onto the antenna substrate presents serious coupling issues and extremely proper design is required for accurate performance. A number of designs have been presented where passive components have been embedded inside the substrate of the antennas for additional control of the signal phase. This method requires specialized fabrication facilities to achieve the goal of phase control. Cavity based antennas have been thoroughly investigated before, however, the main function of the cavities has been enhancement in directivity, operation bandwidth or the efficiency of the antennas. Although thinned FPC have been studied in literature, beam scan has always been achieved by, either using traditional technique or by employing mechanically moving superstrates. Due to the high SLLs seen with scanning FPCs, beam scanning using the traditional method

is not generally preferred. High permeability ferrite has been used for miniaturization as well as frequency and bandwidth tuning. Use of LTCC-ferrite coils have shown to reduce external biasing issues but no design with embedded LTCCs for antenna arrays is available. From the literature search done in this chapter, no FPC with ferrite superstrates was found.

## CHAPTER 3

# MICROWAVE FERRITES

Externally magnetized ferrite control devices rely on the interaction of the microwave (MW) signal and the spinning electrons of ferrites. This gyromagnetic interaction mainly depends on the external magnetizing field and can change the insertion magnitude and phase of the MW signal. A thorough understanding of the physical phenomenon related to gyromagnetic interaction is essential in developing the mathematical expressions of,

- 1- The relationship between the magnetizing field and the spinning electron in the form of an equation of motion.
- 2- The MW propagation within the magnetized anisotropic ferrite material having a tensor permeability and scalar permittivity.
- 3- The characteristic equations of a magnetized ferrite geometry (disk or rod), commonly used in microwave control devices, like circulators, phase shifters etc.

This chapter aims to provide a review of the mathematical derivations related to above steps. Section 3.1 details an overview of the types of magnetism provided by magnetized

microwave ferrites. Section 3.2 derives the equation of motion related to magnetized ferrite material. Sections 3.3 and 3.4 presents the characteristic equation of an axially magnetized ferrite rod, derived by substituting the permeability tensor and the boundary conditions within the Maxwell's equation and mode charts are also plotted. Section 3.5 presents a parametric simulation of magnetized ferrite rods in controlled environment providing a link between the analytical results of Section 3.4 and the simulation models. MATLAB codes are developed to solve the characteristic equation and plot the mode charts of the magnetized ferrite rod. This allowed the determination of the optimum (low-loss) operating region for the ferrite material and avoid the lossy resonance region. These analytically calculated mode charts are later used to validate the related HFSS model of the ferrite geometry.

### **3.1 Magnetic Properties of Ferrites**

The presented work relies heavily on the application of magnetized ferrite material and its interaction with MW signals. Hence, it is of utmost importance to understand the fundamentals associated with the magnetic properties of ferrites.

Magnetism relates to the magnetic moment of a free atom [62], which, in turn depends on orbital and the spin motion of the valence electrons of a material and the way the electrons interact with each other with respect to their own spin. There are three fundamental forces that constitute the magnetic moment of an atom; namely, the spin of the electrons, the angular momentum of the electron circling the nucleus, and the orbital momentum induced by an external magnetic field. Magnetic materials are classified on the

basis of their response to an applied magnetic field, either AC or DC. The extent of magnetism is determined by how the individual magnetic moments interact as the applied magnetic field persists over time. Mathematically, the magnetization ( $M$ ) is defined as the magnetic moment per unit volume and is related to the magnetic susceptibility,  $\chi$ , through equation (12), where  $B$  is the magnetic field intensity.

$$\chi = \frac{M}{B} \quad (12)$$

Magnetic behavior of materials can be classified into four classes: diamagnetic, paramagnetic, ferromagnetic, and ferrimagnetic. Diamagnetism, although very weak, is a fundamental property of all matter [63]. It is a temporary phenomenon, which exists only as long as an external magnetic field is applied. Individual atoms inside a diamagnetic substance have no net magnetic moments; no free/unbounded electrons exist. Magnetic moments inside a diamagnetic material are very weak and pointed in a direction opposite to that of the applied field, resulting in negative values of the magnetization vector. Diamagnetic materials are generally characterized by constant negative susceptibility values, resulting due to a negative magnetism produced under the action of an external magnetizing field. Physically speaking, ionic crystals and inert gases are diamagnetic, because of the absence of any valence electrons, where magnetization is due to the orbital motion of the electrons. All nonmagnetic materials including semiconductors like Si, Ge, GaAs, etc. are diamagnetic, unless doping with excessive  $n$ - or  $p$ -type materials is done.

Para-magnetism arises due to the presence of an odd number of valence electrons in an atom, resulting in a net spin moment [64]. According to Langevin's theory [65], under the action of an external magnetic field, the randomly oriented individual atomic magnetic

moments spirally align with the applied DC magnetizing field. Consequently, a paramagnetic material demonstrates low magnetization in the direction of the applied field, hence yielding a small but positive  $\chi$ . Magnetism in diamagnetic and paramagnetic materials exists only as long as the external magnetic field persists, hence, such type of materials are generally considered as non-magnetic in nature. Transition metals like cobalt, iron and nickel are examples of naturally occurring paramagnetic materials. Like the diamagnetic materials, paramagnetic materials show a linear relationship between  $B$  and  $H$  with a comparatively higher slope as show in Fig. 5.

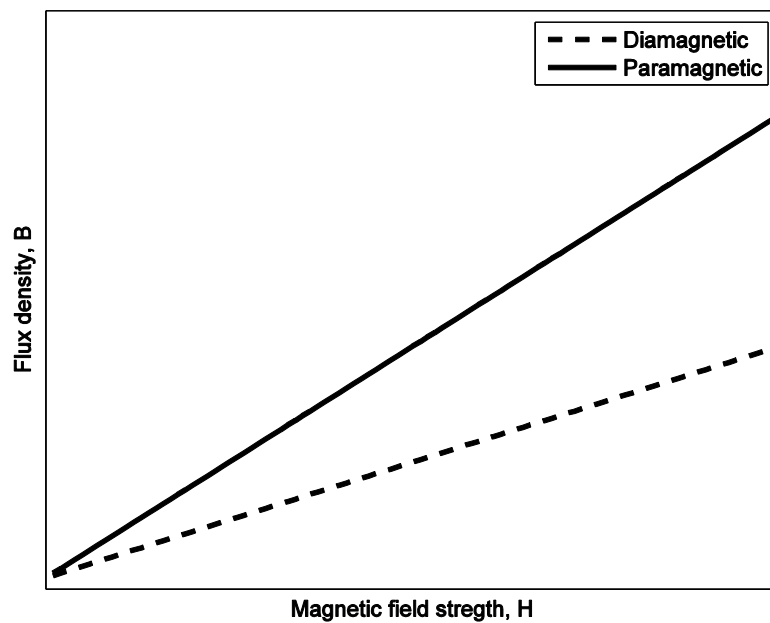


**Figure 5. Schematic representation of B-H curve for diamagnetic and paramagnetic materials.**

Ferromagnetism exists in materials with an inherent lattice shape molecular structure, such that a net magnetization exists even in the absence of an external magnetic field. Mutual coupling interactions between the magnetic moments of adjacent atoms inside a ferromagnetic material result in a net magnetic moment even when no external field is applied. The individual magnetic moments inside a ferromagnetic material interact

strongly with each other in the presence of an external magnetizing field and result in large values of  $\chi$ . At or below certain temperature (Curie temperature,  $T_c$ ), naturally occurring elements like iron, cobalt and nickel show ferromagnetic behavior, which changes to paramagnetism beyond  $T_c$ . In some materials, the alignment of magnetic moments of adjacent atoms is completely opposite and tend to cancel each other, resulting in *antiferromagnetism*. Manganese oxide (MnO) shows antiferromagnetic behavior below its respective  $T_c$ . The molecular arrangement of this compound is such that the  $O^{2-}$  ions have no net magnetic moment, the  $Mn^{2+}$  ions, however, have a crystal arrangement such that the magnetic moments of adjacent atoms are anti-parallel resulting in no net moment.

Ferrimagnetic materials, such as, ferrites ( $Fe_2O_3$ ) exhibit similar magnetic properties to ferromagnetic materials. The complex molecular structure of ferrimagnetic materials allows the atomic moments to parallelly align themselves in some parts of the sub-lattice, whereas in other parts show anti-parallel alignment. These different alignment regions result in magnetic domains within a ferrimagnetic material. The factor that differentiates these materials is that the domains inside a ferrimagnetic material show a net positive moment resulting in comparatively lower saturation magnetization values ( $M_s$ ), as compared to ferromagnetic materials. Fig. 6 shows a pictorial representation of the atomic moments inside the different type of magnetic materials.

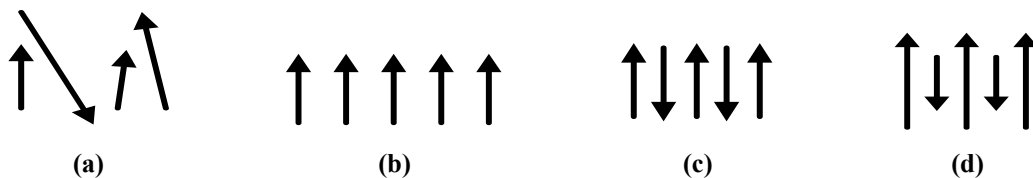


**Figure 6. Graphical representation of magnetic moment of atoms for (a) paramagnetic, (b) ferromagnetic, (c) anti-ferromagnetic and (d) ferrimagnetic materials – the direction of the arrow indicates the direction of the magnetic moment and the length indicates its magnitude.**

### 3.2 Motion of Electron within Magnetized Ferrites

Based on the torque and the angular momentum of a spinning electron, the general equation of motion within a magnetized ferrite material is derived in this Section. When magnetized with an external DC biasing field ( $H_0$ ), the magnetic moments resulting from the spinning electrons spirally align towards the axis of  $H_0$ , as shown in Fig. 7.

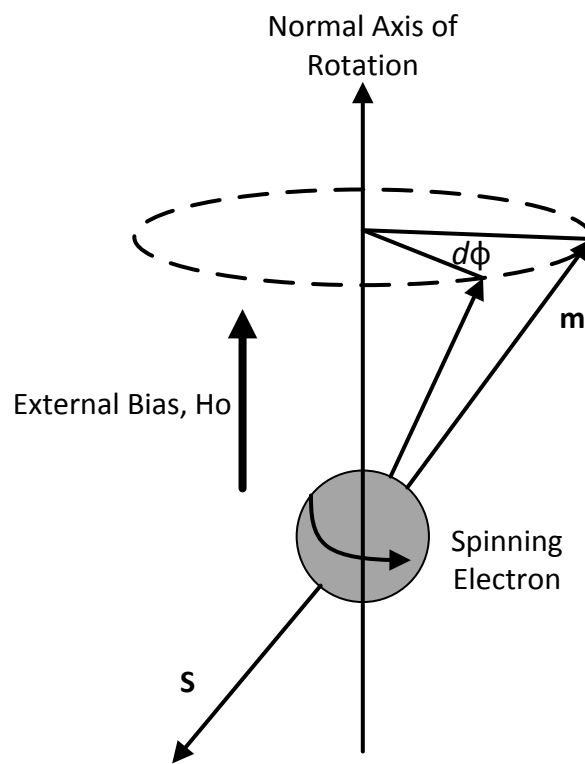


Figure 7. Spinning electron under the influence of an external magnetizing field,  $H_0$ .

In the absence of  $H_0$ , the electron spins around its normal axis of rotation with the magnetic moment,  $m$ , directed along the axis. Under the application of an external magnetic field,  $H_0$ , in a plane perpendicular to the plane of the spinning electron, a net torque acts on the electron causing  $m$  to change direction resulting in a precessional motion of the spinning electron. Fig. 7 depicts the precessional motion of the electron under  $H_0$ . The

torque on a spinning electron due to  $H_o$  is a cross product of the magnetic moment and the applied DC field [66]. Mathematically, the vector representation of torque is given by (13) as,

$$\mathbf{T} = \mu_o \mathbf{m} \times \mathbf{H}_o \quad (13)$$

The spin angular momentum of a spinning electron,  $\mathbf{S}$ , is given by,

$$\mathbf{S} = \frac{\hbar}{2} \quad (14)$$

Where  $\hbar$  is the reduced Plank's constant with a numerical value,  $\hbar = 1.054 \times 10^{-34}$  J.s.

The magnetic moment,  $m$ , and the spin angular momentum,  $\mathbf{S}$ , are related through a constant  $\gamma$  as,

$$\mathbf{m} = -\gamma \mathbf{S} \quad (15)$$

The negative sign shows that the angular momentum is in opposite direction to that of the magnetic moment as shown in Fig. 7 as well. Rewriting (13) in terms of  $\mathbf{S}$ ,

$$\mathbf{T} = -\mu_o \gamma \mathbf{S} \times \mathbf{H}_o \quad (16)$$

$$\frac{d\mathbf{m}}{dt} = -\mu_o \mathbf{m} \times \mathbf{H}_o \quad (17)$$

For (17), the fact that torque is the rate of change of angular momentum ( $\mathbf{T} = \frac{d\mathbf{S}}{dt} = -\frac{1}{\gamma} \frac{d\mathbf{m}}{dt}$ ) has been used. Using Cartesian coordinate system and with the

supposition that the applied DC magnetic bias,  $H_o$ , is directed along the z-axis, solution of (17) yields the following system of second order homogeneous differential equations.

Intermediate steps have been skipped here and can be found in Appendix A-1.

$$\begin{aligned} \frac{d^2 m_x}{dt^2} + \omega_o^2 m_x &= 0 \\ \frac{d^2 m_y}{dt^2} + \omega_o^2 m_y &= 0 \end{aligned} \quad (18)$$

Solution of (18) yields the respective components of the magnetic moment of the single electron as,

$$\begin{aligned} m_x &= A \cos \omega_o t \\ m_y &= A \sin \omega_o t \\ m_z &= B \end{aligned} \quad (19)$$

$A$  and  $B$  are constants and  $\omega_o$  is the natural precession frequency of the electron and is a function of the ferrite material.

Assuming  $N$  number of individual electrons inside the ferrite material, each having distinct magnetic moment  $m_i$  (for  $i = 1, 2, \dots, N$ ), the net magnetization of the material per unit volume,  $V$ , is given by (20),

$$\mathbf{M} = \frac{\sum_{i=1}^N \mathbf{m}_i}{\Delta V} \quad (20)$$

Under the influence of a strong enough  $H_o$ , all magnetic moments ( $m_i$ 's) tend to align themselves with the direction of the externally applied DC field. At saturation, the magnitude as well as the directions of all the individual magnetic moments will be the same, thus generalizing (20) as,

$$\mathbf{M} = N\mathbf{m} \quad (21)$$

Hence the macroscopic form of the general equation of motion is written as,

$$\frac{d\mathbf{M}}{dt} = -\mu_o \gamma \mathbf{M} \times \mathbf{H} \quad (22)$$

where  $\mathbf{H}$  represents both the AC and DC components of the magnetic field. When placed in the path of a transmitting RF signal, the magnetic field of the RF signal contributes to the AC part of  $\mathbf{H}$ .

When the operating frequency of the transmitting RF signal matches the natural precession frequency of the ferrite material, maximum energy transfer occurs. This condition gives rise to the lossy resonance region of the ferrite material. So, for any meaningful control of the propagating MW signal, ferrites are magnetized to operate either below or above resonance regions.

### 3.3 Polder Permeability Tensor

Permeability of any material represents its reaction to an applied magnetic field. Generally, permeability is defined as the ratio between the magnetic flux,  $\mathbf{B}$ , and the magnetic field,  $\mathbf{H}$ . Mathematically,

$$\mathbf{B} = \mu_0\mu_r\mathbf{H} \quad (23)$$

where  $\mu_0$  and  $\mu_r$  are the respective permeability in free space and the relative permeability of the material. Due to the changing direction of the magnetic moment, ferrite materials exhibit anisotropic behavior with respect to the applied external DC biasing. Because of this inherent anisotropy, the permeability of ferrite is no longer a scalar value. Mathematically the relation in (23), for ferrites, can be expressed as,

$$\mathbf{B} = [\mu]\mathbf{H} \quad (24)$$

where  $[\mu]$  represents a matrix. When a biased ferrite is placed in the path of transmitting RF signals, the RF signal tends to disturb the natural precession motion of the atoms. Mathematically, the total magnetic field,  $\mathbf{H}_t$ , and the total magnetization,  $\mathbf{M}_t$ , for a ferrite material biased by a DC field acting in the  $\hat{\mathbf{z}}$  (axial) direction can be represented by (25),

$$\begin{aligned}\mathbf{H}_t &= H_0\hat{\mathbf{z}} + \mathbf{h} \\ \mathbf{M}_t &= M_0\hat{\mathbf{z}} + \mathbf{m}\end{aligned}\quad (25)$$

where  $H_0$  is the external DC field,  $\mathbf{h}$  is the magnetic field contribution from the RF signal,  $M_0$  is the DC magnetization and  $\mathbf{m}$  is the AC magnetization caused as a result of  $\mathbf{h}$ . Substituting (25) into the general equation of motion (22) derived in Section 3.2 we get,

$$\frac{d\mathbf{M}}{dt} = -\mu_0\gamma(M_0\hat{\mathbf{z}} + \mathbf{m}) \times (H_0\hat{\mathbf{z}} + \mathbf{h}) \quad (26)$$

Assuming  $h_z \ll H_0$  and  $m_z \ll M_0$  and ignoring the cross component product terms due to negligible amplitudes, (26) can be simplified as,

$$\begin{aligned}\frac{dM_x}{dt} &= -\omega_0 M_y + \omega_m H_y \\ \frac{dM_y}{dt} &= \omega_0 M_x - \omega_m H_x \\ \frac{dM_z}{dt} &= 0\end{aligned}\quad (27)$$

where,  $M_x$ ,  $M_y$  and  $M_z$  are the x-, y- and the z-components of the magnetic moment,  $\omega_0 = \mu_0\gamma H_0$  and  $\omega_m = \mu_0\gamma M_0$ . A detailed step-by-step derivation is provided in Appendix A-2.

For time-varying  $\mathbf{H}$  and  $\mathbf{M}$ , (27) can be transformed as,

$$\begin{aligned}j\omega M_x &= -\omega_0 M_y + \omega_m H_y \\ j\omega M_y &= \omega_0 M_x - \omega_m H_x \\ j\omega M_z &= 0\end{aligned}\quad (28)$$

Simultaneous solution of the linear systems of equations in (28) yields the following results,

$$\begin{aligned}
 M_x &= \frac{\omega_0 \omega_m}{\omega_0^2 - \omega^2} H_x + j \frac{\omega \omega_m}{\omega_0^2 - \omega^2} H_y \\
 M_y &= -j \frac{\omega \omega_m}{\omega_0^2 - \omega^2} H_x + \frac{\omega_0 \omega_m}{\omega_0^2 - \omega^2} H_y
 \end{aligned} \tag{29}$$

$$M_z = 0$$

Using the internal magnetic components derived in (29), the tensor permeability or the Polder permeability matrix can be derived by using the general relationship of (30) for ferrite materials,

$$\mathbf{B} = \mu_o (\mathbf{M} + \mathbf{H}) \tag{30}$$

$$\mathbf{B} = \mu_o \left( \begin{bmatrix} M_x \\ M_y \\ M_z \end{bmatrix} + \mathbf{H} \right)$$

$$\mathbf{B} = \mu_o \left( \begin{bmatrix} \frac{\omega_0 \omega_m}{\omega_0^2 - \omega^2} & j \frac{\omega \omega_m}{\omega_0^2 - \omega^2} & 0 \\ -j \frac{\omega \omega_m}{\omega_0^2 - \omega^2} & \frac{\omega_0 \omega_m}{\omega_0^2 - \omega^2} & 0 \\ 0 & 0 & 0 \end{bmatrix} \mathbf{H} + \mathbf{H} \right) \tag{31}$$

For simplicity, substituting  $\boldsymbol{\chi} = \begin{bmatrix} \frac{\omega_0 \omega_m}{\omega_0^2 - \omega^2} & j \frac{\omega \omega_m}{\omega_0^2 - \omega^2} & 0 \\ -j \frac{\omega \omega_m}{\omega_0^2 - \omega^2} & \frac{\omega_0 \omega_m}{\omega_0^2 - \omega^2} & 0 \\ 0 & 0 & 0 \end{bmatrix}$  in (31),

$$\mathbf{B} = \mu_o (\boldsymbol{\chi} + \mathbf{I}) \mathbf{H} \tag{32}$$

Hence, the permeability matrix,  $[\boldsymbol{\mu}] = \mu_o (\boldsymbol{\chi} + \mathbf{I})$

$$[\boldsymbol{\mu}] = \mu_o \begin{bmatrix} \left(1 + \frac{\omega_0 \omega_m}{\omega_0^2 - \omega^2}\right) & j \frac{\omega \omega_m}{\omega_0^2 - \omega^2} & 0 \\ -j \frac{\omega \omega_m}{\omega_0^2 - \omega^2} & \left(1 + \frac{\omega_0 \omega_m}{\omega_0^2 - \omega^2}\right) & 0 \\ 0 & 0 & 1 \end{bmatrix} \quad (33)$$

Substituting  $\mu = 1 + \frac{\omega_0 \omega_m}{\omega_0^2 - \omega^2}$  and  $\kappa = \frac{\omega \omega_m}{\omega_0^2 - \omega^2}$  in (33) gives us the general Polder permeability matrix for a ferrite material in (34) [66],

$$[\boldsymbol{\mu}] = \mu_o \begin{bmatrix} \mu & j\kappa & 0 \\ -j\kappa & \mu & 0 \\ 0 & 0 & 1 \end{bmatrix} \quad (34)$$

The permeability tensor of (34) is derived for the assumption that the applied DC magnetic field,  $H_o$  is axially directed along the z-axis. Any change in the direction of  $H_o$  would result in a different mathematical analysis producing a different permeability matrix. As observed from the values of  $\mu$  and  $\kappa$ , the permeability of ferrite depends on the DC biasing field, the frequency of the RF signal and the natural precession frequency of the material.

### 3.4 Operating Conditions for Magnetized Ferrite Rods

In order to use the ferrite material (either rods or disks) to control the EM wave propagation, its low-loss operating regions needs to be identified to avoid lossy resonance region. As per Section 3.3, changing the magnetizing field allows controlling EM wave propagation through ferrite material, when it is operating away from lossy resonance region. Thus, for adequate transmission of EM wave through the ferrite material, it needs to be magnetized in the low loss operating region, either below or above the ferromagnetic

resonance. In this research work, a ferrite rod is used to introduce controlled phase delay to the propagating microwave (MW) signal. So characteristic equations related to axially magnetized ferrite rod is reproduced for magnetic side wall boundary.

### 3.4.1 Characteristic Equation of a Ferrite Rod with Magnetic Side-Wall

This section provides the derivation details of the characteristic equation and also provides the theoretical resonance regions for the ferrite material. To keep the text concise, some of the mathematical steps have been skipped here but can be found in Appendix A-3. For a plane wave travelling in the +z-direction, using the Suhl and Walker [67] [68] technique to split up the field vectors into transverse and normal components gives us the following field equations,

$$\begin{aligned}
\mathbf{E} &= (\mathbf{E}_t + E_z \hat{\mathbf{z}}) e^{-j\beta z} \\
\mathbf{H} &= (\mathbf{H}_t + H_z \hat{\mathbf{z}}) e^{-j\beta z} \\
\mathbf{B} &= (\mathbf{B}_t + B_z \hat{\mathbf{z}}) e^{-j\beta z} \\
&= \mu \mathbf{H}_t + j\kappa(\hat{\mathbf{z}} \times \mathbf{H}_t) + \mu_z H_z \hat{\mathbf{z}}
\end{aligned} \tag{35}$$

$$\nabla = \nabla_t - j\beta \hat{\mathbf{z}}$$

Solving (35) with appropriate boundary conditions eventually leads to the characteristic equation as presented in (36) [66], derivation details can be found in Appendix A-3.

$$\begin{aligned}
&\frac{J_n'(s_1 R)}{J_n(s_1 R)} \left\{ s_1 - \left( \frac{K_0^2 \mu_{eff} \epsilon_r - \beta^2}{s_1} \right) \right\} + \frac{J_n'(s_2 R)}{J_n(s_2 R)} \left\{ s_2 - \left( \frac{K_0^2 \mu_{eff} \epsilon_r - \beta^2}{s_2} \right) \right\} \\
&\quad - \frac{\kappa n \beta^2}{\mu R} \left\{ \frac{s_2^2 - s_1^2}{(s_1^2)(s_2^2)} \right\} = 0
\end{aligned} \tag{36}$$

### 3.4.2 Operating Regions of Axially Magnetized Ferrite Rod

In order to select low loss operating regions for a given ferrite material, it is important to look into the field-frequency representation of the mode charts. The mode chart provides a relationship between the interaction of the MW signal and the spinning electrons of the ferrite and allow the selection of the operating regions that provide best compromise between single loss and external tenability. For our work, a low-loss calcium vanadium garnet type of ferrite (Y220) rod with  $\epsilon_r=15.4$ ,  $M_s=155.2$  KA/m,  $\Delta H=10$  Oe and  $R=3$ mm has been selected. Using the characteristic equation (36) derived in Section 3.4.1, a cut-off related to Y220 ferrite rod has been plotted in Fig. 8. The yellow marked region in Fig. 8, indicates the lossy resonance region of the ferrite material. For an operating frequency of 10 GHz, analytical solutions of Fig. 8 clearly illustrate that the resonance region starts from 285 kA/m and continues till 440 kA/m. Hence, a lossless operation can be achieved if the ferrite is magnetized to operate either below 285 kA/m or above 440 kA/m.

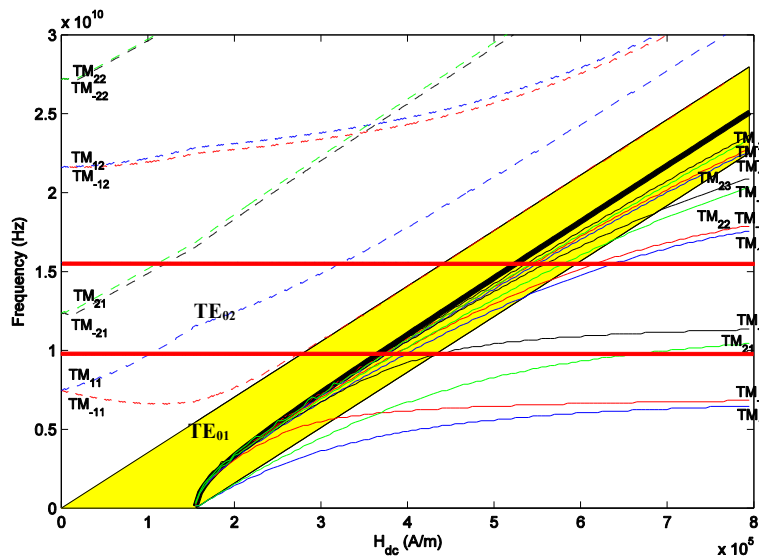
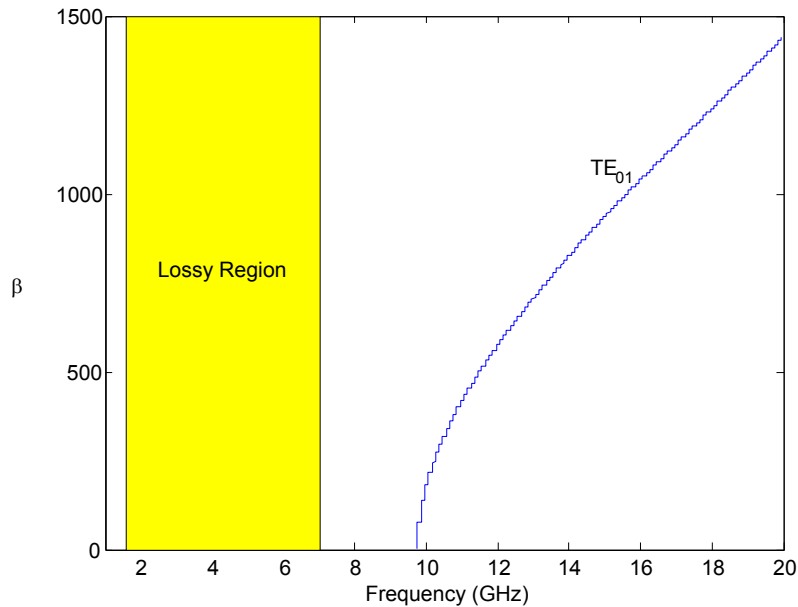
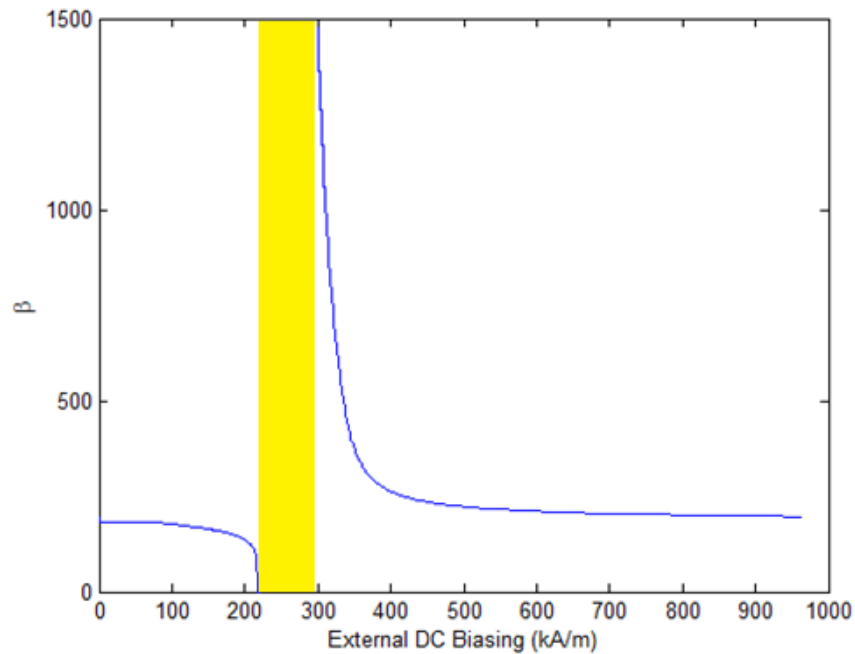


Figure 8. Mode chart for the Y220 ferrite cylinder with  $R = 3$ mm,  $M_s = 155$  kA/m,  $\Delta H=10$  Oe and  $\epsilon_r=15.4$ .

At a fixed  $H_0 = 200$  kA/m (below resonance), the  $\beta$ - $f$  curves for  $TE_{nm}$  modes are plotted in Fig. 9. Note that  $TE_{01}$  mode cuts-off just below 10 GHz, as also predicted by the field-frequency curve of Fig. 8. The changes in phase constant within the ferrite rod with changing operating frequency is clear from this figure. Similar  $\beta$ - $H_0$  curve for a fixed operating frequency of 10 GHz is plotted in Fig. 10. For the selected ferrite material, these charts allow the selection of a low-loss operating region, where larger changes in insertion phase can be achieved with relatively small changes in biasing field. In Fig. 10, the yellow shaded region represents the lossy resonance region, where EM waves are mostly absorbed by the ferrite material through maximum gyro-magnetic interaction. Note that close to resonance region boundaries, the maximum changes in the phase constant ( $\beta$ ) can be produced with minimal changes external biasing field.



**Figure 9.**  $\beta$ (rad/sec)- $f$  curve for a fixed external magnetizing field of 200 kA/m for an axially magnetized Y220 ferrite rod with  $\epsilon_r=15.4$ ,  $M_s=155.181$  KA/m and  $R=3$ mm.



**Figure 10.**  $\beta$ (rad/sec)– $f$  curve for a fixed external magnetizing field of 200 kA/m for an axially magnetized Y220 ferrite rod with  $\epsilon_r=15.4$ ,  $M_s=155.181$  KA/m and  $R=3$ mm.

So selecting the operating region of ferrite material for certain control action needs a compromise between the acceptable losses and the requirement of external magnetizing field. Since large magnetizing field requires large external magnets, often tailored ferrite materials with low resonance region are desired.

### 3.5 Gyro-Magnetic Properties of Magnetized Ferrite

In Section 3.4, characteristic equation of an axially magnetized ferrite rod with magnetic side wall boundaries were used to plot the cutoff charts and phase constants ( $\beta$ ) with respect to changing axial magnetizing fields. These charts are used here to determine the low loss operating region. Since biasing the ferrite cylinders requires the use of electromagnets; optimized solenoid coils are needed to maintain a balance between size of the coil and the input current requirement. To analyze and understand the gyromagnetic

interaction of axially magnetized ferrite rod and propagating EM waves, a biased ferrite rod has been analyzed with the help of a rectangular waveguide. By selecting a waveguide with a very low cut-off frequency, two different HFSS simulations schemes have been used to observe the effect of biased ferrite rod on the transmission characteristics of the RF signal. The first simulation setup (setup 1) involves observing the transmitted signal by placing the ferrite rod inside the chosen waveguide, a schematic diagram of setup 1 is shown in Fig. 11. Simulation setup 2, involves placing the magnetized ferrite rod within a propagating EM wave between two rectangular waveguides, as shown by the schematic in Fig. 12. The simulation results of setup-1 represent guided environment, whereas, setup-2 includes the effects of free space loss and mimics the actual placement of ferrite over the antenna as desired in this work.

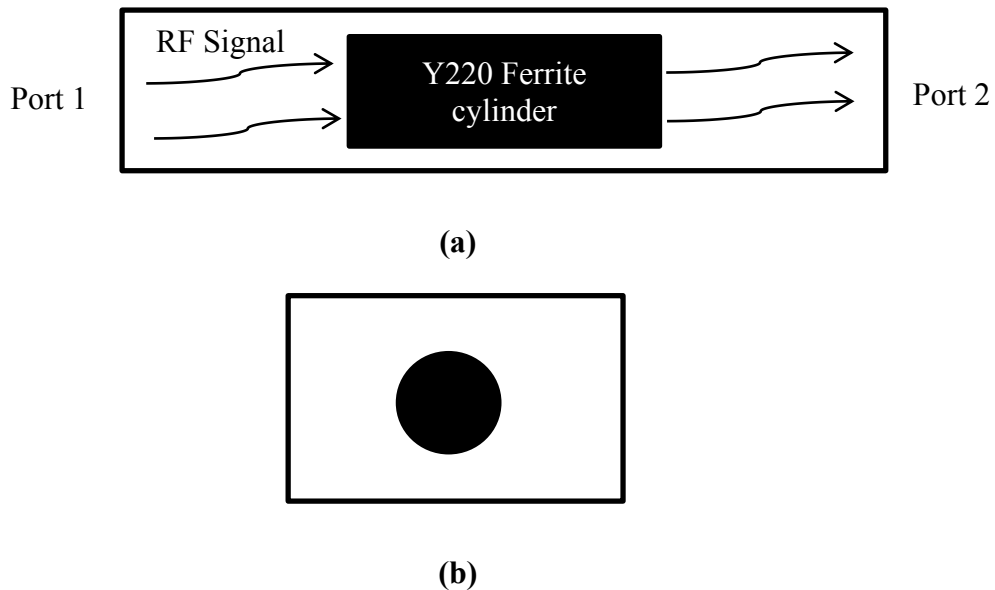


**Figure 11. HFSS simulation model for setup 1 with ferrite cylinder inside a 10 GHz waveguide (a) Side view and, (b) Cross-sectional view.**



**Figure 12. HFSS simulation model for setup 2 - ferrite rod in free space between waveguides.**

A WR110 metallic waveguide with a cutoff frequency of 6.5 GHz is selected for both setups to operate at 10 GHz. The transmission characteristics of the waveguide are shown in Fig. 13.

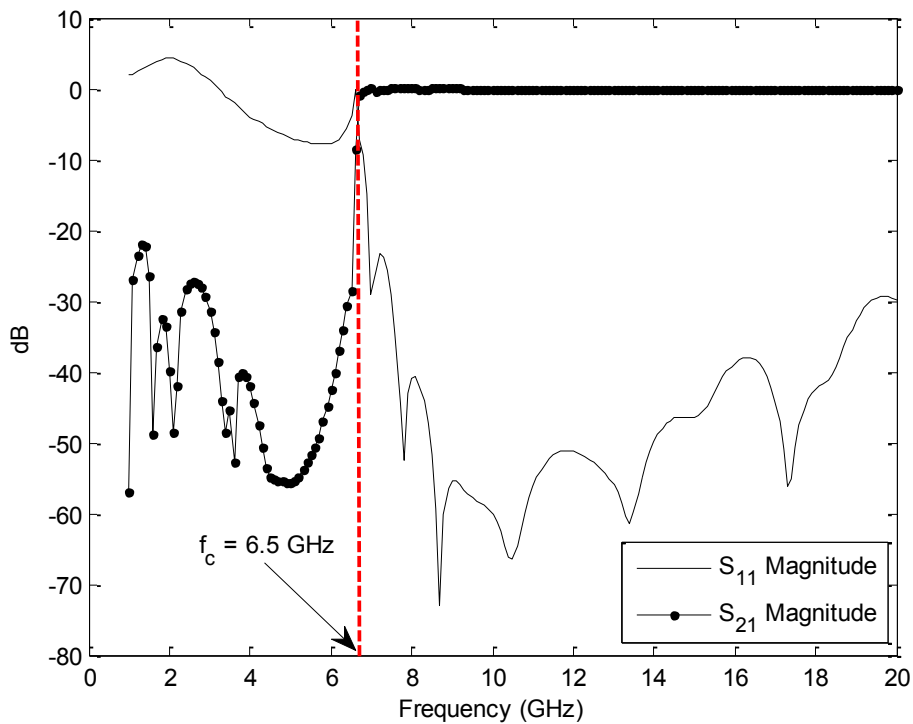
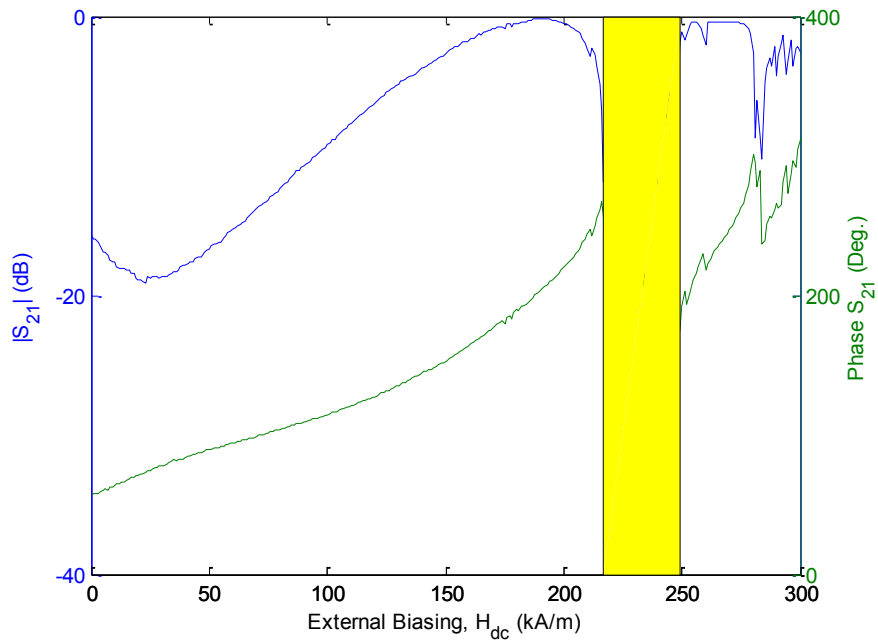


**Figure 13. Magnitude of transmission ( $S_{21}$ ) and reflection ( $S_{11}$ ) coefficients for the Waveguide.**

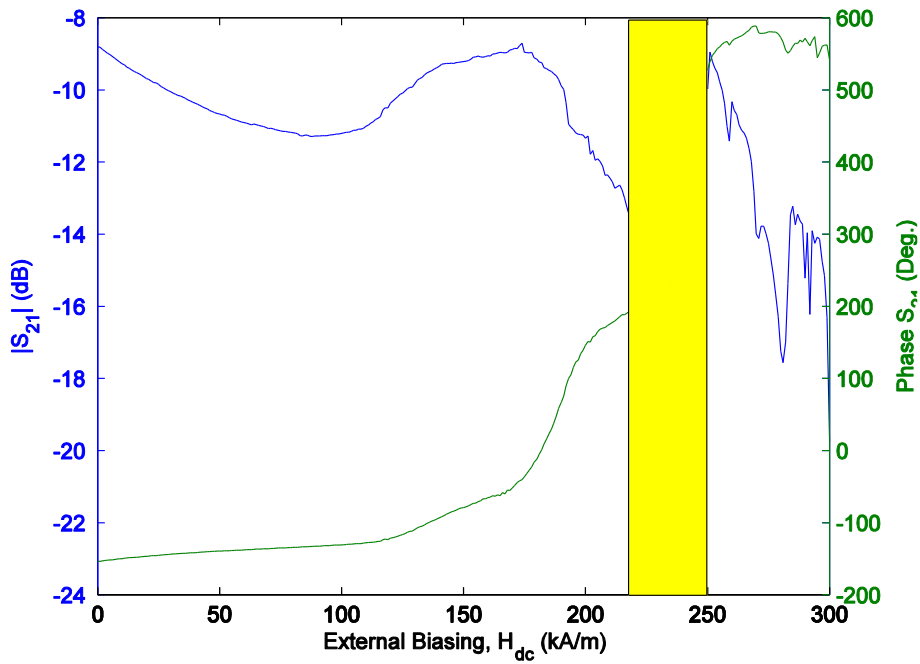
For setup 1, a Y220 ferrite cylinder with radius ' $r$ ' and length ' $l$ ' is suspended in the center of the waveguide using a dielectric material with  $\epsilon_r=1$  (foam). Port 1 is used to excite the waveguide with a 10 GHz signal and the output is observed on Port 2 as indicated in

Fig. 11. Unlike the analytical results presented in Chapter 3, HFSS can only provide  $\beta$  at the ports (port 1 and 2 in our waveguide case). This, unfortunately, is not same as the analytical technique, where the  $\beta$  is calculated at the edge of the ferrite cylinder, which highlights the affects due to the ferrite rod only. To overcome this issue, the transmission coefficient of the waveguide has been taken as a measure of the signal transmitted through the ferrite. Fig. 14 shows the simulated transmission coefficient (magnitude and phase) for both setup-1 and setup-2. Note that between 220kA/m and 250 kA/m, the magnitude as well as the phase of the transmitted signal starts to decline abruptly due to lossy gyromagnetic resonance. This resonance region is also plotted in the analytical results of Chapter 3. The difference between the magnetic biasing corresponding to analytical and simulated resonances of Fig. 10 and Fig. 14 is due to the generation of standing waves within the rectangular waveguide. Note that the best transmission response is observed between magnetic biasing of 150 KA/m and 210 KA/m, where the  $|S_{21}| > 0.905$  dB and the change of phase of  $\angle S_{21} \cong 57^\circ$ .

A complete parametric study of the ferrite cylinder and its effect on the transmitted signal is done in the following sub-sections to determine the optimum dimensions of the ferrite cylinder.



(a)



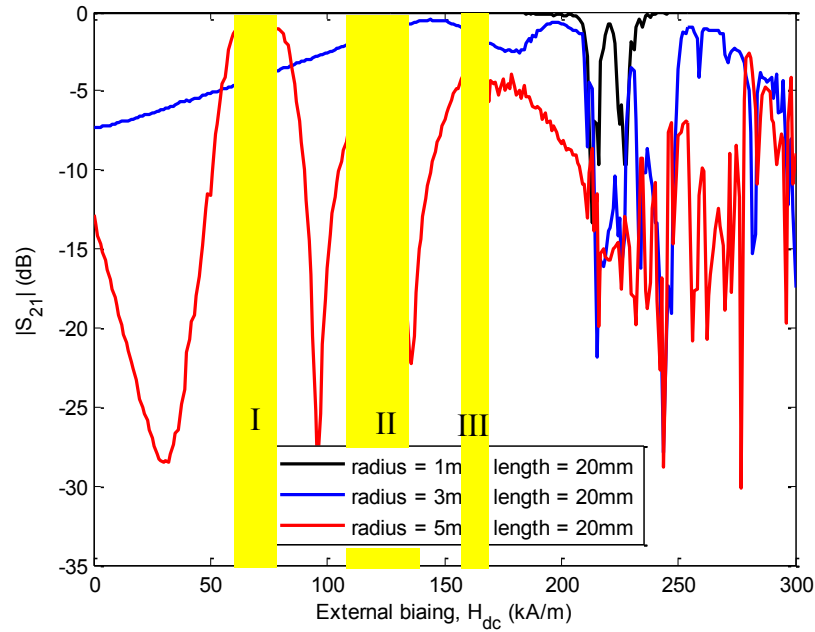
(b)

Figure 14. Magnitude and phase of the transmission coefficient for a rectangular waveguide, (a) case 1 – ferrite cylinder inside the waveguide, (b) Case 2 – ferrite cylinder in free-space.

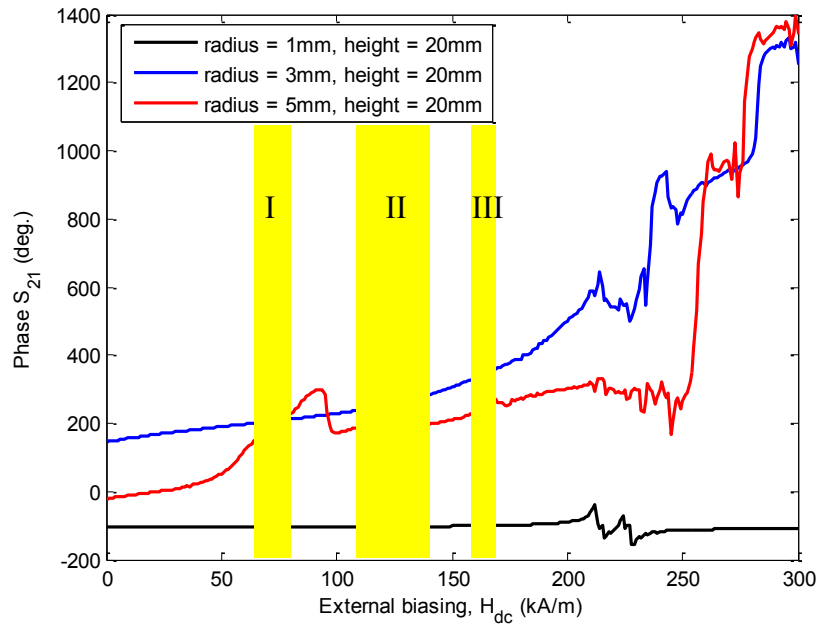
### 3.5.1 Variation of Ferrite Cylinder Radius ( $r$ )

A comparison of the transmission characteristics of the two simulation cases presented in Fig. 14 reveals that the variation in the magnitude as well as the phase follows the same trend. The transmitted signal loss observed in Fig. 14(b) is due to the signal propagation in free space. Considering the simplicity of the simulation setup of case 1, case 1 has been chosen for a thorough investigation of the ferrite behavior. To investigate the effects of the radius, the ferrite cylinder is placed in the center of the waveguide and is axially biased with external DC magnetized field of 0 (unbiased case) to 300 kA/m. The phase and magnitude of the transmitted signal for changing biasing field is plotted in Fig. 15. It is observed that with increasing radius of the ferrite cylinder, the resonance region tends to increase. Such as, for  $r = 1\text{mm}$  resonance region occurs between 210 kA/m to 225 kA/m, whereas for  $r = 5\text{mm}$  the resonance region occurs between 210 kA/m to 290 kA/m. Observing the magnitude curve of Fig. 14(a), it is clear that smaller ferrite ( $r = 1\text{mm}$ ) allows constant transmission in the low-loss region below resonance, whereas increasing radius deteriorates the transmitted signal. The worst case is observed for a thick ferrite ( $r = 5\text{mm}$ ), where several high loss and low loss regions (I, II and III in Fig. 15) are observed below resonance. A view of the  $S_{21}$  phase of Fig. 15(b) shows that for a thinner ferrite cylinder ( $r = 1\text{mm}$ ), the phase of the received signal remains constant throughout the low loss regions. As the radius is increased the phase starts to change smoothly with increasing biasing values. For  $r = 3\text{mm}$ , the phase increases sharply as the biasing approaches the resonance region, which is what is actually required for a practically working system. In other words, when operating closer to the resonance region, a small change in the biasing causes a big variation in the phase of the transmitted signal. This, however, is not the case

when  $r = 5\text{mm}$  is used; multiple regions of sudden increase in phase are observed even at lower  $H_{dc}$  values. Thus a thicker ferrite provides better phase variations at lower  $H_{dc}$  values but also attenuates a large portion of the signal going through it.



(a)

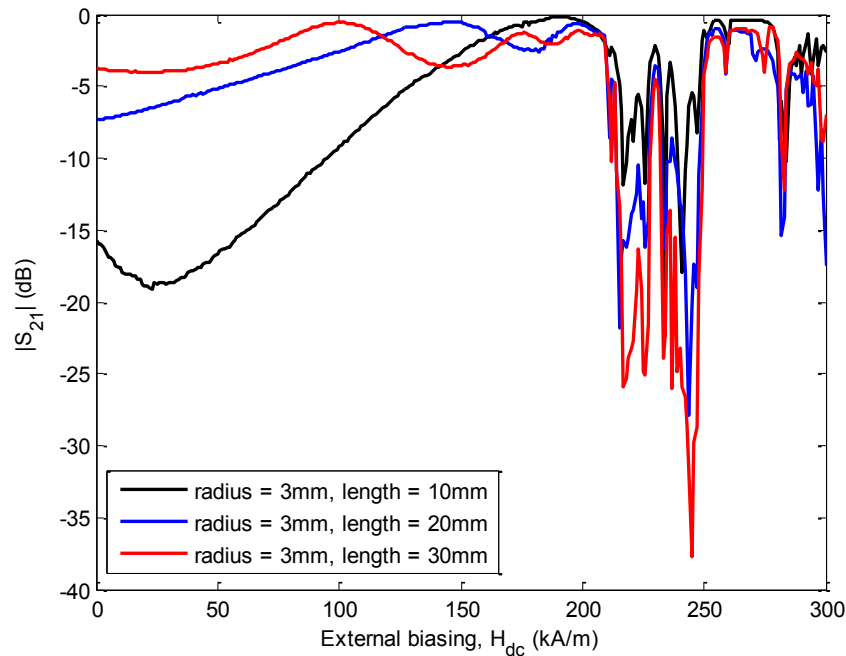


(b)

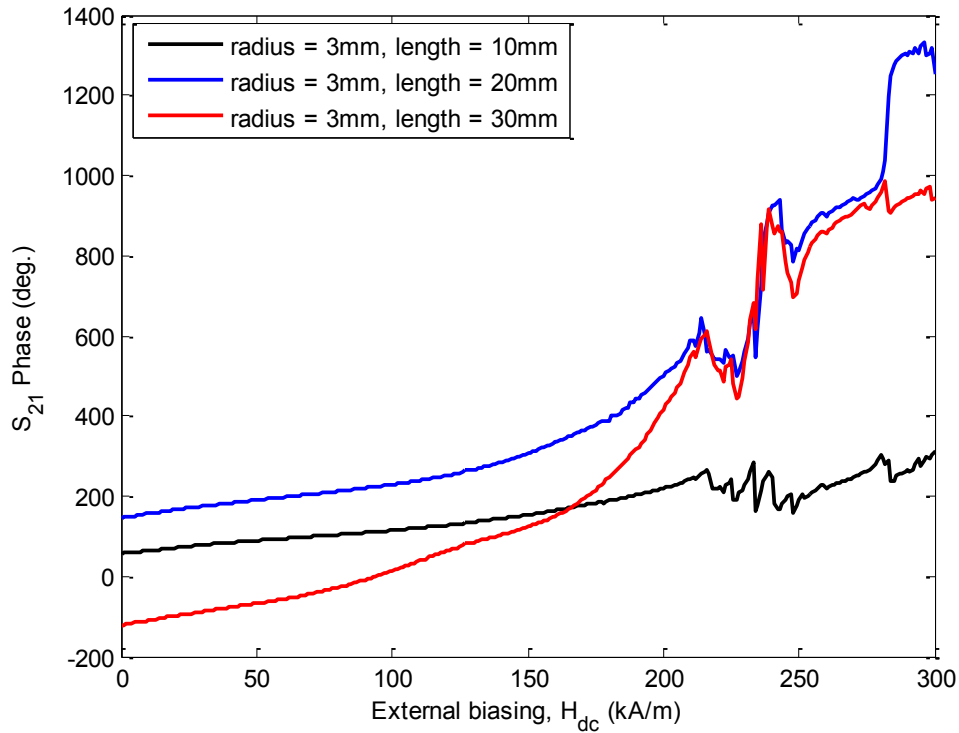
Figure 15. Transmission coefficient ( $S_{21}$ ) for a ferrite loaded waveguide (a) Magnitude and (b) Phase - for ferrite cylinder having fixed length,  $l = 20\text{mm}$  and variable radius,  $r$ .

### 3.5.2 Variation of Ferrite Cylinder Length ( $l$ )

For this study the radius,  $r$ , of the ferrite cylinder is fixed to 3mm and the length,  $l$ , of the cylinder is varied to see its effect on the transmitted signal. Fig. 16 shows the results for this case. With a fixed radius, the resonance region remains the same regardless of the cylinder length; as observed from the analytical expression of (36). Fig. 16 shows that a smaller ferrite cylinder causes higher signal attenuation at lower biasing values and the phase variation in the transmitted signal is also not considerable. As ' $l$ ' is increased, the cylinder starts to transmit higher signal values even at lower biasing and the phase variations also become steep, particularly near the resonance region (Fig. 16(b)). Although a longer cylinder provides the best magnitude and phase response, it is not practically feasible to use large ferrites based superstrate, as the antenna profile increases and makes the design bulky to employ.



(a)



(b)

Figure 16. Transmission coefficient ( $S_{21}$ ) for a ferrite loaded waveguide (a) Magnitude and (b) Phase - for ferrite cylinder having fixed radius,  $r = 3\text{mm}$  and variable length,  $l$ .

The ferrite dimensions that provide maximum signal transmission as well as the highest phase variation at lower biasing values are most desired. From Section 3.5.1, it is observed that a thicker ferrite cylinder provides better transmission and higher phase variation well below the resonance region (indicated by Region I in Fig. 15). Operating regions II and III can be used as well but require significantly higher biasing values for acceptable transmission and meaningful phase variations. Similarly considering the length,  $l$ , variations presented in Fig. 16, it is observed that a longer ferrite provides good transmission at lower biasing values. However, the phase variation is the sharpest near the resonance regions. Based on the above mentioned conclusions, the best choice is to use the thickest (high  $r$ ) and the longest (high  $l$ ) ferrite cylinders. Since ferrites require coils to be

wrapped around them for biasing, a thicker ferrite is usually not desired since most of the signal path is blocked by the winding. Similarly, a taller ferrite cylinder makes the antenna profile larger and bulky and has to be avoided. Based on the pros and cons discussed earlier,  $r = 3\text{mm}$  and  $l = 20\text{mm}$  has been selected with operating regions II and III.

### 3.6 Conclusion

Gyromagnetic interaction between the RF-fields and the ferrite material result in a change in the properties of the signal. The anisotropic behavior of ferrite is characterized by the polder permeability matrix which shows a dependence of permeability on the RF-signal frequency, the saturation magnetization of the ferrite material and the externally applied DC magnetic field. From the characteristic equation of the ferrite rod with a radius  $R$ , mode charts suggesting low-loss biasing regions are obtained. These mode charts suggest highly lossy performance between 285 kA/m to 410 kA/m for a 10 GHz RF signal. Plotting the  $\beta$ -H charts provides the actual analytical operating region to be either below 210 kA/m or above 300 kA/m. A parametric study of the HFSS simulation models of the ferrite rods suggest a change in the transmission magnitude as well as the phase for changing magnetizing field. A thicker ferrite (higher  $R$ ) tends to provide better transmission as well as higher phase variation at lower magnetizing fields, whereas, a longer ferrite rod (high  $l$ ) tends to have steeper phase variation only close to resonance.

## CHAPTER 4

# FERRITE SUPERSTRATE BASED PHASE CONTROL OF RADIATED WAVE

The gyromagnetic interaction between ferrite superstrate and the radiated EM waves can introduce externally controllable phase delay, which in turn can change the radiation characteristics of the antenna. Thus, placing axially magnetized ferrite cylinder on top of a patch antenna can produce beam scan. To achieve maximum scan angle with minimum change in external biasing, the ferrite dimensions and placement of the ferrite disk is essential. This chapter presents a detailed investigation into the gyromagnetic properties of an externally magnetized rod. As a proof of concept, two ferrite rods are used to realize a superstrate that can introduce beam scanning characteristics of a single 10GHz patch antenna. This chapter is organized as follows; Section 4.1 presents the tunable magnitude and phase properties of magnetized ferrite, design of a microstrip patch antenna with a magnetized ferrite superstrate is presented in Section 4.2, design of an FPC excited by a 10 GHz microstrip patch antenna is presented in Section 4.3, and the chapter closes with a conclusion in Section 4.4.

## 4.1 Phase Properties of the Radiated Wave

The parametric study presented in Section 3.5 demonstrates the performance of the longitudinally biased ferrite in a loss-less environment. It is noted that the magnetized ferrite cylinder with dimensions of  $r = 3\text{mm}$  and  $l = 20\text{mm}$  provides the best transmission magnitude and phase response. In order to demonstrate the phase delay properties of the axially magnetized ferrite rod, it is employed as a superstrate of a microstrip patch antenna. The composite ferrite-foam superstrate consisted of two ferrite cylinders embedded within a foam material. The beam scanning capability of this superstrate is investigated for continuously changing external biasing fields.

In a uniform phased array antenna, scanning the main beam requires patch excitation signals with same magnitude and progressive phase ( $\beta$ ) distribution. Typically, phase shifters are used to produce the required  $\beta$  needed to steer the main beam in the direction of  $\theta_0$ , as per standard array factor equations [1]. For a 2-element linear phased array antenna with patch separation of  $0.5\lambda$ , the relationship between main beam directions and the phase distribution of the radiated E-fields are plotted in Fig. 17. This figure shows that a phase taper of  $6.5^\circ$ ,  $14.1^\circ$  and  $99^\circ$  is needed to steer the main beam towards  $\theta = 100^\circ$ ,  $110^\circ$  and  $120^\circ$  in the broadside, respectively. These phase taper values are calculated by taking the difference between the actual phase values at the middle of the patches on the observation lines.

Since the ferrite does change the phase of the signal passing through it, using two biased ferrite cylinders in the radiation region of the antenna can produce the phase taper similar

to the one shown in Fig. 17. Hence the ferrite superstrate has to be carefully designed and placed optimally within the radiation region of the antenna for it to affect the main beam direction.

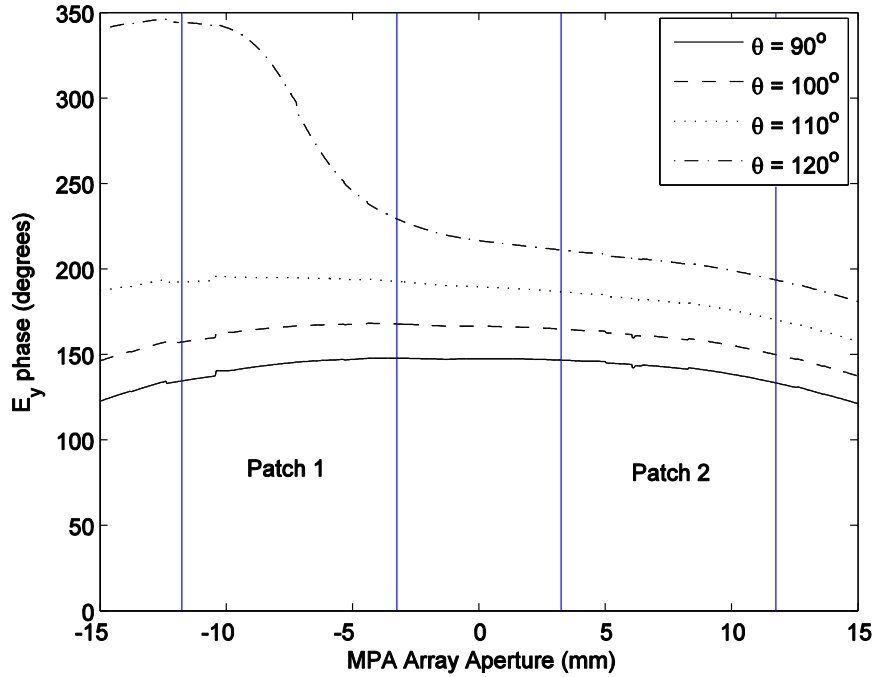


Figure 17. E-field phase distribution for different directions of the main beam for a 2-element PAA.

## 4.2 Ferrite Superstrate loaded Microstrip Antenna

### 4.2.1 Design of Ferrite Loaded Microstrip Patch Antenna

A single coaxially fed MPA is designed to operate at 10GHz. To introduce beam scanning, the MPA is loaded with a superstrate layer comprising of two optimally located magnetized ferrite rods. Fig. 18 shows the designed microstrip antenna on a Duroid substrate ( $\epsilon_r=2.2$ ,  $\mu_r=1$ ) and loaded with two Y220 ferrite rods ( $\epsilon_r=15.4$ ,  $\mu_r \propto H_0$ ) as an air-ferrite superstrate. The optimized dimensions of the antenna are:  $h_{sub} = 1.6$  mm,  $W_{ferr} = 40$ mm,  $L_{ferr} = 40$ mm,  $W_p = 8.5$ mm and  $L_p = 8.72$ mm. Since ferrite loading

introduced a cavity between the air-ferrite superstrate and the patch radiator, minimizing the cavity resonance is important for this non-Fabry-Perot cavity (non-FPC) model. Using professional software (HFSS), the reflection coefficients ( $S_{11}$ ) of the simple MPA and the ferrite superstrate loaded (non-FPC) antenna is plotted in Fig. 19.

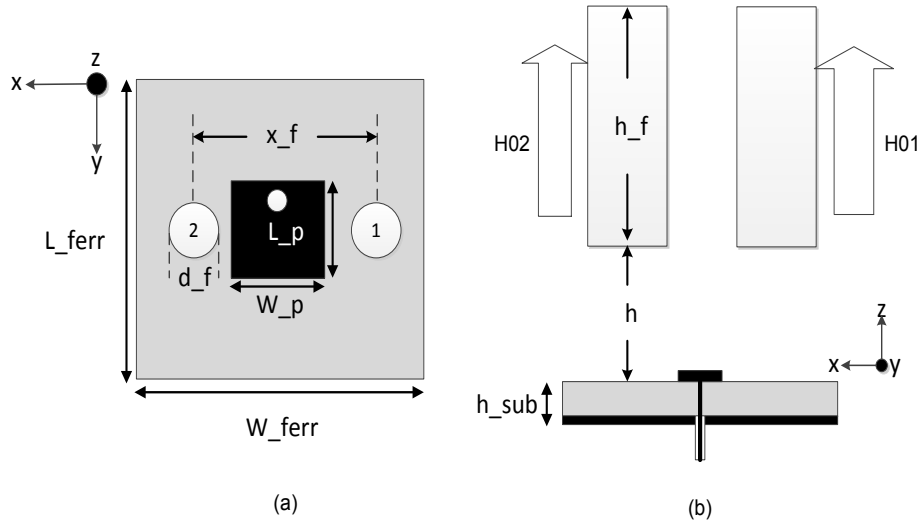


**Figure 18. Magnetized ferrite loaded patch antenna (non-FPC) (a) Top view, and (b) Side view.**

Note that both the antennas demonstrate an impedance bandwidth of 723 MHz, maximum gain of 6.69 dB for the simple MPA and 6.58 dB for the ferrite superstrate loaded MPA in the broad side direction ( $\theta_0=90^\circ$ ) with HPBW of approximately  $60^\circ$  in the E-plane.

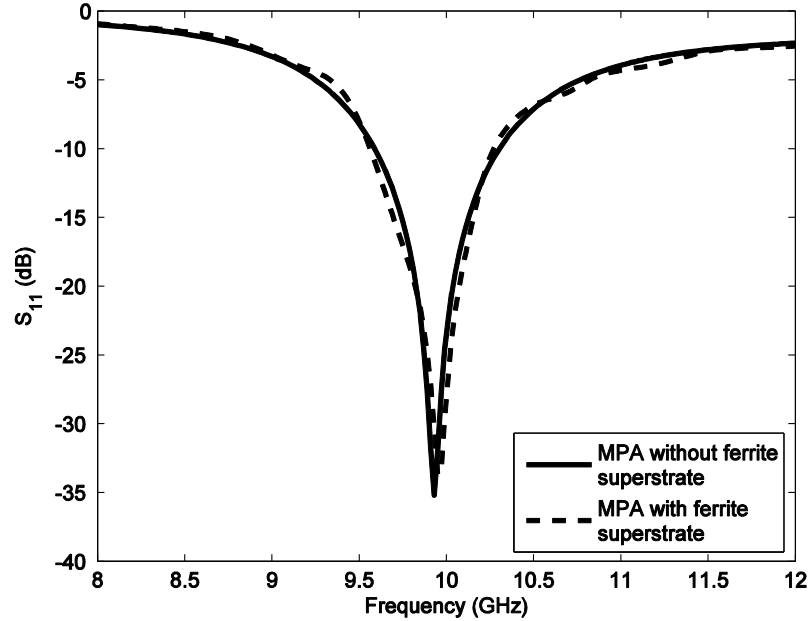
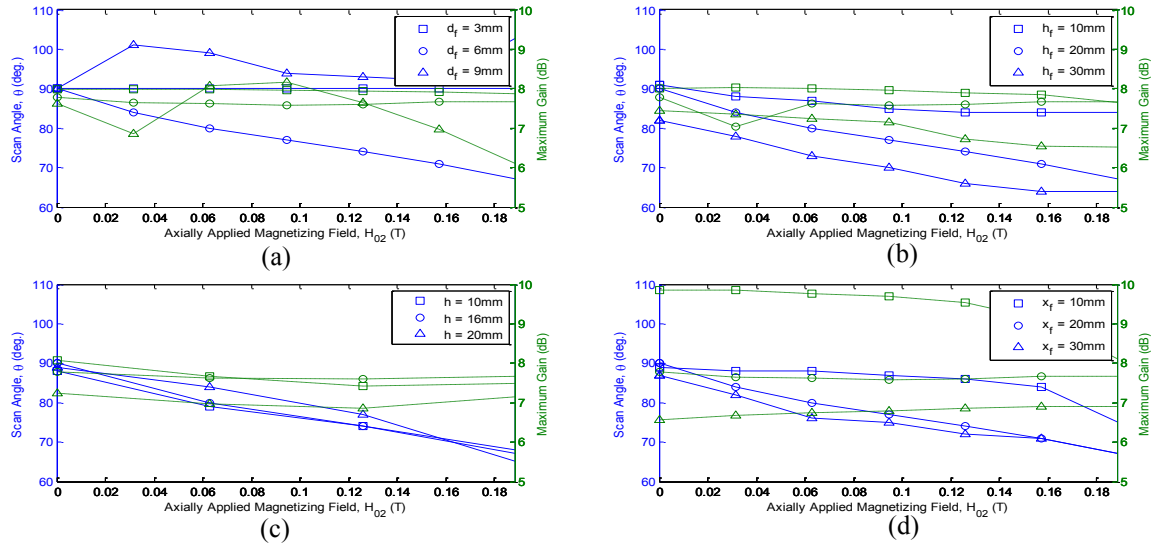


Figure 19. Simulated reflection characteristics of loaded and simple microstrip patch antenna (MPA).

## 4.2.2 Radiation Response of the Ferrite Loaded Microstrip Antenna

Determining the correct location ( $x_f, h$ ) and the dimensions ( $d_f, h_f$ ) of the ferrite rods is important to achieve acceptable gain and required beam scanning properties. For Y220 ferrite material with  $\epsilon_r=15.4$ ,  $4\pi M_s=1950$  Gauss and  $\Delta H=10$  Oe, a comprehensive parametric analysis of the four variables;  $x_f, h, d_f$  and  $h_f$ , is done to determine the best position and dimensions for the ferrite rods. The results of the parametric sweep simulations are provided in Fig. 20. In order to simulate the ferrite loaded structure, both the ferrite rods (1 and 2 in Fig. 18) are biased with an external magnetic field in the + z direction. Biasing both rods 1 and 2 simultaneously with the same amount of  $H_0$  did not produce any beam scan. However, when rods 1 and 2 are biased with different values of



**Figure 20. Amount of beam scan (degrees) and the maximum gain for variation in (a)  $d_f$  (b)  $h_f$  (c)  $h$  and (d)  $x_f$ , dotted green line for gain and solid blue line for beam scan angle.**

magnetic field ( $H_{01}$  and  $H_{02}$ , respectively), a beam scan proportional to the differential magnetic field between  $H_{01}$  and  $H_{02}$  is achieved. So to achieve a notable beam scan, one of the ferrite rods is kept unbiased ( $H_{01}=0$ ), while the other one ( $H_{02}$ ) is varied.

Fig. 20(a) plots the changing radiation parameters of the antenna with varying diameter ( $d_f$ ) of the ferrite rods. For fixed values of the height ( $h_f=20\text{mm}$ ) and separation ( $x_f=20\text{mm}$ ), increasing the diameter of the ferrite rods from 3mm to 6 mm produces a total scan angle of  $26^\circ$  for  $\Delta H_{02}=0.16\text{T}$  (127 kA/m). Note that, the gain of the antenna remains constant for the whole range of the biasing field. But a further increase in  $d_f$  reduced the antenna gain without improving the scan angle. Considering the parametric sweep for ferrite length ( $h_f$ ) in Fig. 20(b), it is clear that a taller ferrite rod offers more beam scan compared to shorter ones. However, this also increases the antenna dimension in addition to reducing the antenna gain for a given value of  $H_{02}$ . As an optimum value,  $h_f=20\text{mm}$  is selected as it produces a maximum beam scan angle of  $26^\circ$  with nearly constant antenna gain of 7.8 dB.

In Fig. 20(c), it is clear that increasing the spacing ‘h’ between the antenna aperture and the ferrite rod tends to decrease the scan angle. This is due to the formation of the partially resonant cavity between the patch aperture and the ferrite rod. Increasing or decreasing the size of this resonant cavity results in excitation of different modes which affects the scan angles of the antenna. The parameter value of  $h = 16\text{mm}$  is chosen as it offers a good beam scan while provided the highest gain throughout our sweep ( $\Delta H_{02}$ ).

Since beam scan of the designed antenna depends on the interaction of the radiated E-fields and the ferrite rods, optimum positioning of the ferrite rods is important to maximize the phase taper and antenna gain. In Fig. 20(d), it is clear that higher value of  $x_f$  or placing the ferrite rods closer to the edges provides higher beam scans at the cost of reduced antenna gain. Note that  $x_f=20\text{mm}$  provides the best compromise between the scan angle and antenna gain for  $\Delta H_{02}= 0.16\text{T}$  (127 kA/m). From the parametric analysis, it is observed that a higher interaction of the RF signal with the ferrite rod results in higher values of beam scan and a relatively higher signal loss as well. Based on the theory of the magnetized ferrite material presented in Section 3.1, the thicker (high  $d_f$ ) or the longer (high  $h_f$ ) the ferrite rod, the higher the number of magnetic dipoles inside the material. A higher number of oriented magnetic dipoles result in an increased interaction with the passing RF signal; resulting in a larger change in the phase of the signal eventually leading to higher beam scan. One of the issues observed with thicker and larger ferrite rods is higher energy transfer from the RF signal to the precessing dipoles causing a decrease in the antenna directivity as noticed in Fig. 20.

Thus, based on the parametric analysis, the chosen values that offer the best scan angle with highest antenna gain are:  $h_f = 20\text{mm}$ ,  $x_f = 20\text{mm}$ ,  $d_f = 6\text{mm}$  and  $h = 16\text{mm}$ . It

must be noted here that although we set  $H_{01} = 0$ , similar but opposite directional beam scan is obtained when varying  $H_{01}$  by setting  $H_{02}=0$ .

### 4.2.3 Results

Before analyzing the beam scan properties of the MPA with ferrite superstrate, the MPA has been simulated with a uniform dielectric superstrate. By creating an FPC above the radiator, a directivity increase of 0.7 dB has been achieved while maintaining the radiating frequency at 10 GHz.

Table 1 shows the achieved beam scan as well as the required DC biasing for both the ferrite cylinders. Changing the biasing field of the 1<sup>st</sup> ferrite ( $H_{01}$ ) produces a broad-side beam scan of +30°. Whereas varying the biasing field of the 2<sup>nd</sup> ferrite ( $H_{02}$ ) produces a beam scan of -30°. It is observed that maximum beam scan is a function of the differential

**Table 1. Beam scan and maximum gain as a function of the magnetizing field – one biased ferrite rod only.**

$H_{01}$ (T)	$H_{02}$ (T)	$\Theta$ (deg.)	Gain (dB)	HPBW (°)
0.22	0	120	7.54	61
0.16	0	110	7.66	61
0.06	0	100	7.64	58.3
0	0	90	7.79	59
0	0.06	80	7.63	58
0	0.16	71	7.67	60
0	0.22	60	7.56	58

DC biasing and not the individual biasing value; this is clearly presented in Table 2. Comparing the results of Table 1 and Table 2, it is evident that for a given value of differential biasing, the amount of beam scan remains the same. The gain does decrease in the case of differential biasing due to the losses incurred because of the magnetized ferrite

cylinders. Fig. 21 shows the  $E_y$  phase distribution above the surface of the structure (patch and the ferrite rods based superstrate combined). As one of the ferrite cylinders starts to get biased, the phase of the RF signal passing through it increases and results in an overall taper (across the structure's aperture) as seen in the curves of Fig. 21. Thus, the biased ferrite tends to increase the differential phase of the signal that passes through it. The 2-D directivity plots of the main radiated beam at  $0^\circ$  and  $\pm 30^\circ$  are shown in Fig. 22.

**Table 2. Beam scan and maximum gain as a function of the magnetizing field – both ferrite rods biased.**

$H_{01}$ (T)	$H_{02}$ (T)	$\Theta$ (deg.)	Gain (dB)	HPBW( $^\circ$ )
0.28	0.06	118	6.93	60
0.22	0.06	109	7.11	58
0.12	0.06	103	7.25	59
0.06	0.06	90	7.38	58
0.06	0.12	79	7.21	61
0.06	0.22	70	7.09	60
0.06	0.28	58	6.97	61

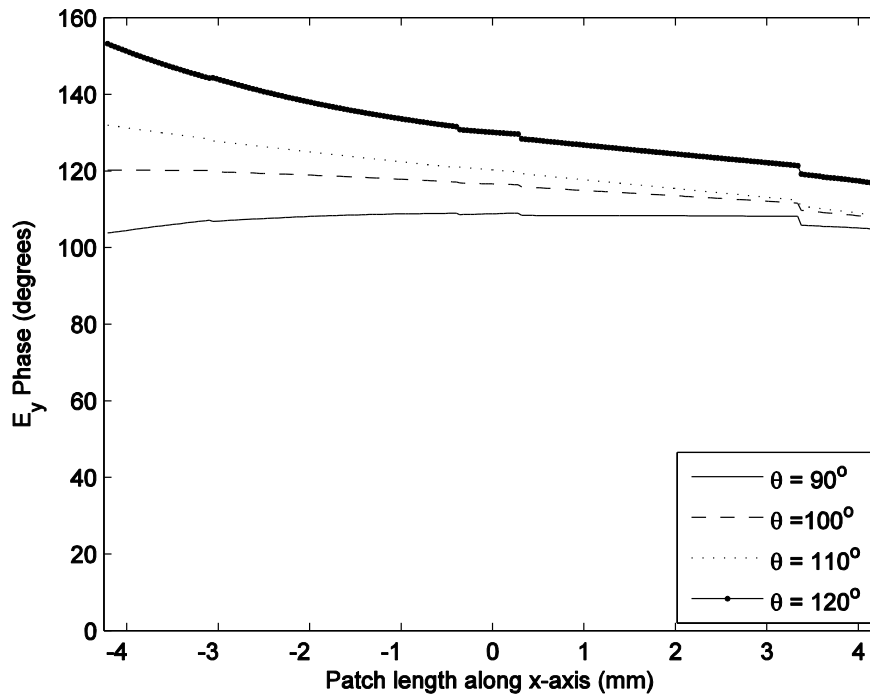


**Figure 21.  $E_y$  phase distribution on the radiated signal just above the MPA for different beam scan angles.**

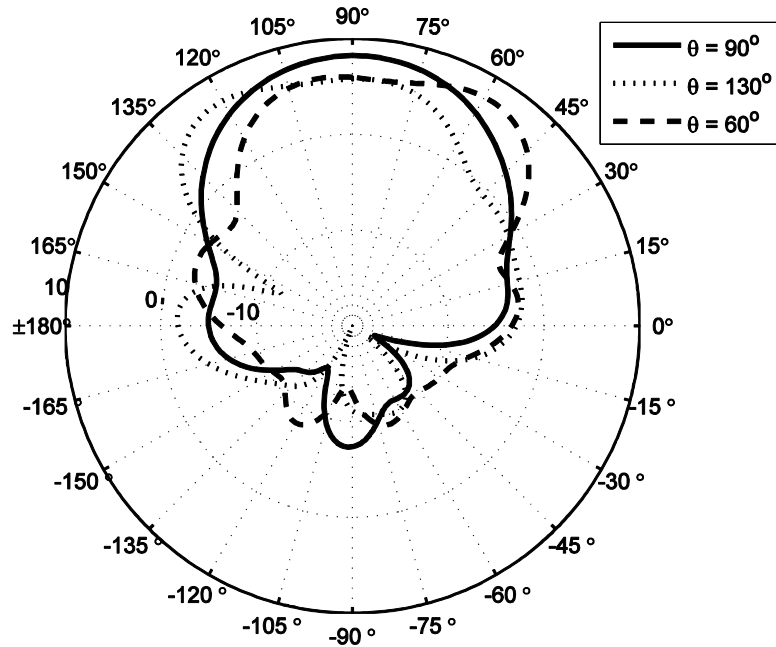
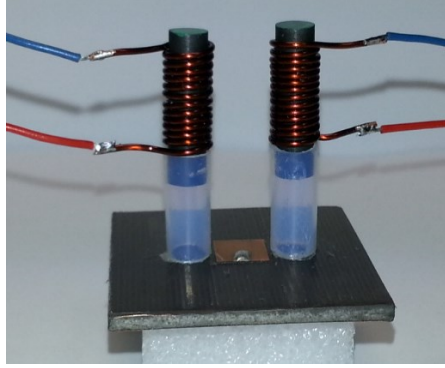
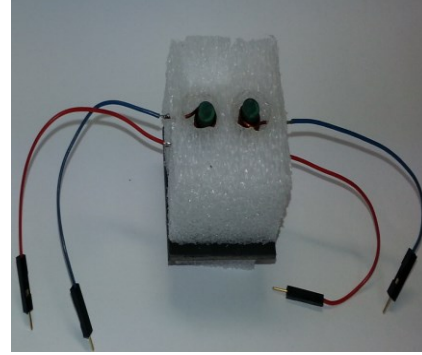


**Figure 22. Simulated broad side radiation patterns of the ferrite loaded MPA with variable biasing conditions.**

The designed antenna along with the superstrate has been fabricated and is shown in Fig. 23. The coils that use variable DC current sources to axially magnetize the ferrite rods are also shown in the figure. Using Tesla meter, the ferrite filled coils have been pre-calibrated to relate the coil currents with induced magnetizing fields. For packaging purposes, the positions of the ferrite rods have been secured by a Styrofoam ( $\epsilon_r \approx 1$ ) cube, as shown in Fig. 23(b). This also allows the removal of the plastic pipes, used to position the ferrite rods in Fig. 23(a).



(a)



(b)

**Figure 23. Fabricated 10 GHz single MPA with ferrite superstrate, (a) with biasing coils and (b) with Styrofoam packing.**

A vector network analyzer is used to measure the reflection response ( $S_{11}$ ) of the ferrite loaded antenna. Fig.24 shows the simulated and experimental  $S_{11}$  responses of the ferrite loaded microstrip patch antenna (MPA). It is observed that separately magnetizing ferrites have no effects on the impedance bandwidth and the resonance of the antenna. Using an antenna measurement setup of Fig. 25, the beam scanning properties of the designed antenna are experimentally observed.

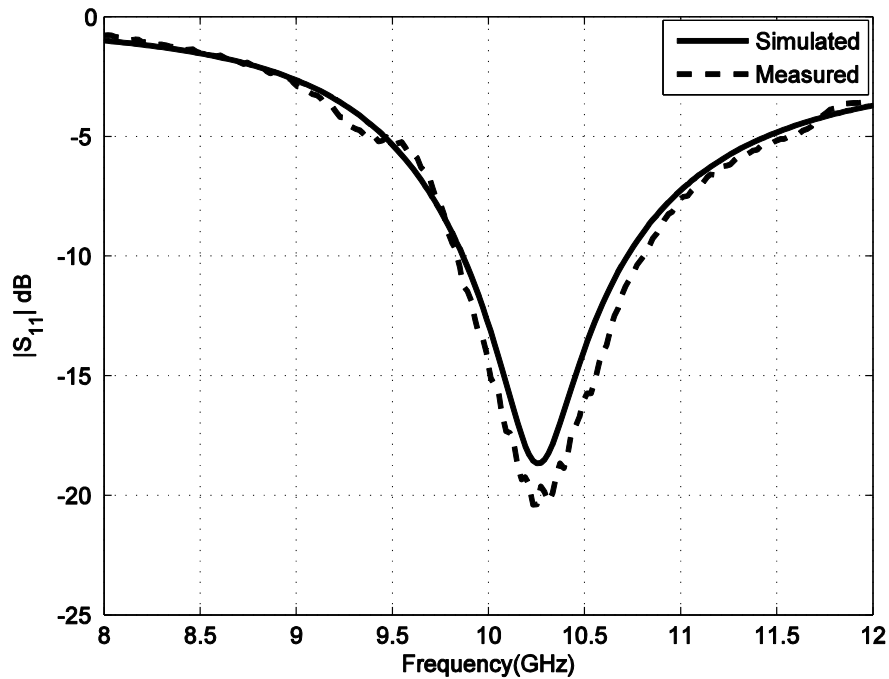


**Figure 24. Simulated and experimental  $S_{11}$  responses of the ferrite loaded MPA.**

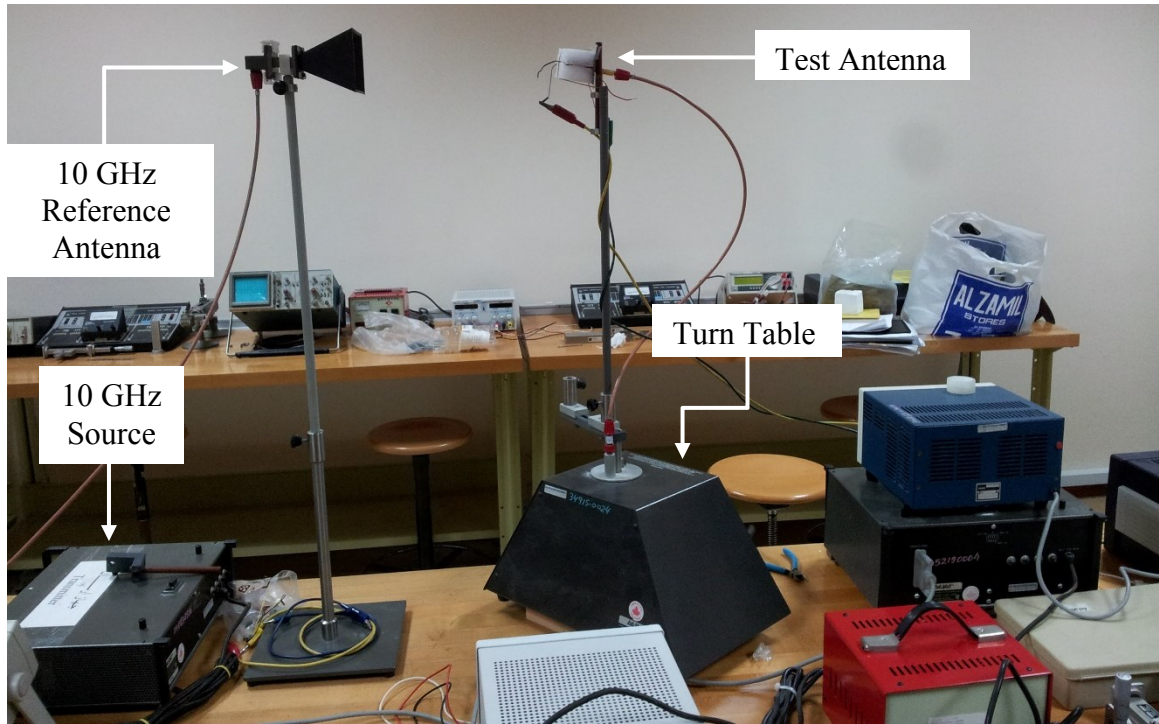
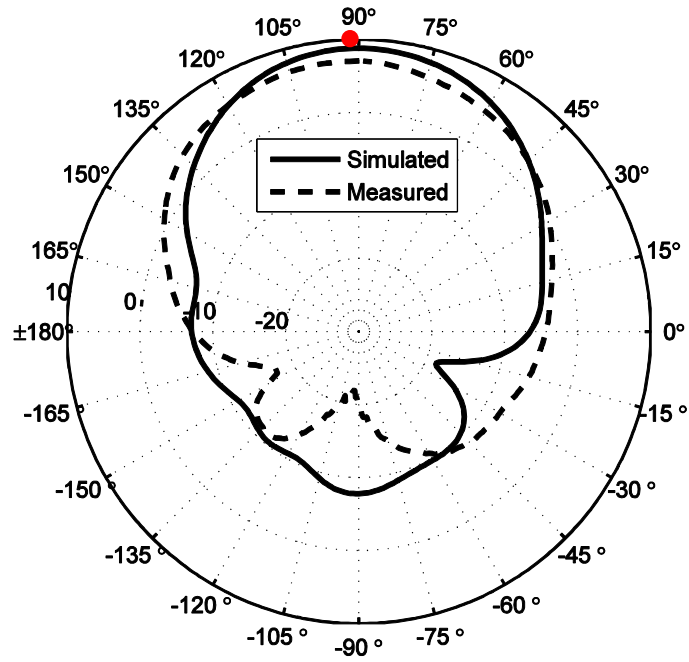
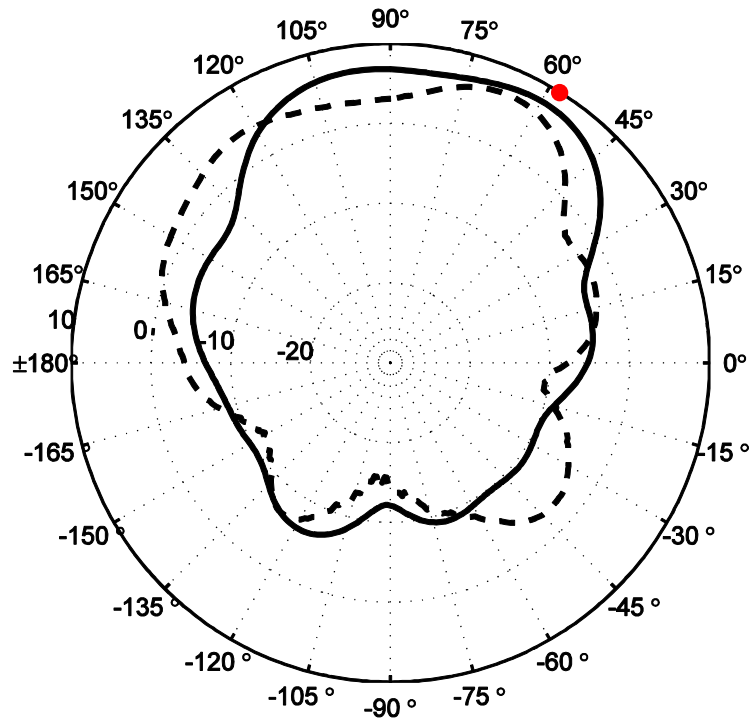


**Figure 25. 2D radiation pattern measurement setup for the designed antennas.**

A comparison of the measured and simulated radiation patterns of the antenna with  $H_{01}=0$  and changing values of  $H_{02}$  are plotted in Fig. 26. Note that maximum simulated scan angles of  $\pm 30^\circ$  are verified by the measured radiation patterns at  $+28^\circ$  and  $-26^\circ$ , respectively. Higher back lobes and minor mismatch between simulated and experimental patterns is due to unwanted reflections normally eliminated by the anechoic chamber. It can be observed from Fig. 26(a) that for no beam scan case, the maximum measured directivity is 7.097 dB and the respective measured directivities at  $64^\circ$  and  $118^\circ$  are 5.255 dB and 6.069 dB. It must be noted that inclusion of ferrite rods and the biasing coils have minimal effect on the radiation properties of the designed antenna, the measured HPBW, directivity and the efficiency values for the MPA without superstrate, with only ferrite and with ferrite and biasing coils is provided in Table 3.



(a)



(b)

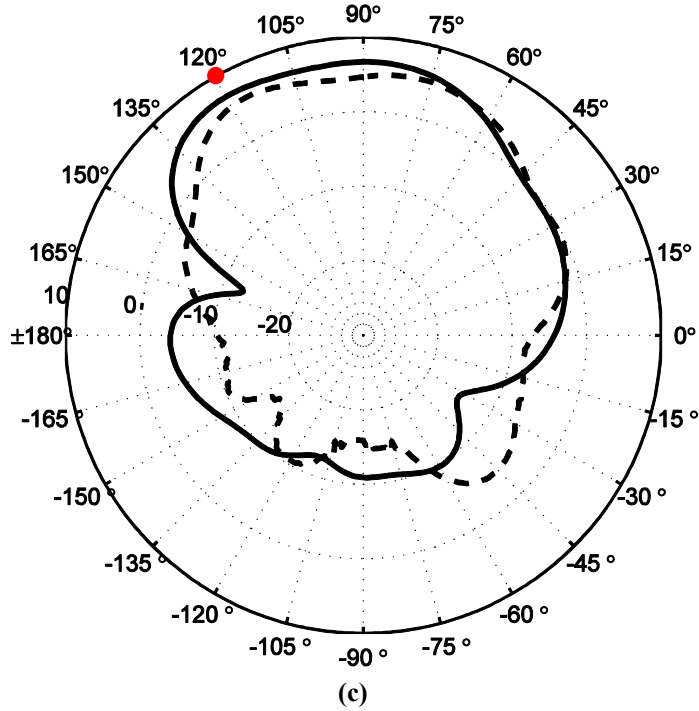


**Figure 26. Comparison of measured and simulated 2D radiation patterns (a)  $\theta=90^\circ$  for  $H_{01}=H_{02}=0$  (b)  $\theta=64^\circ$  for  $H_{01}=0$  and  $H_{02}=0.19T$  and (c)  $\theta=118^\circ$  for  $H_{01}=0.19T$  and  $H_{02}=0T$ .**

When scanning the main beam to either of the maximum scan angles,  $64^\circ$  (Fig. 26(b)) and  $118^\circ$  (Fig. 26(c)), the peak directivity values measured at the respective directions of maximum are 6.69 dB and 6.53 dB. Additionally the directivity measured in the original direction of maximum ( $90^\circ$ ) during beam scanning is 3.091 dB and 5.342 dB for  $64^\circ$  and  $118^\circ$  respectively.

**Table 3. Comparison of the measured HPBW and directivity with  $H_{01}=H_{02}=0$ .**

	<b>HPBW (Deg.)</b>	<b>Directivity (dB)</b>	<b>Efficiency (%)</b>
MPA without superstrate	60	6.687	81.6
MPA with ferrite superstrate, without biasing coils	61.4	7.139	77.83
MPA with ferrite superstrate, with biasing coils	62	7.097	76.19

### 4.3 Design of Ferrite Loaded FPC Excited by MPA

One of the methods to improve the directivity of a MPA is to introduce superstrate and optimally excite the resulted Fabry-Perot-cavity (FPC) between patch and superstrate. As shown by the multiple designs reviewed in Section 2.2, FPCs can produce significant enhancement in the directivity of an antenna. It has also been shown in Section 4.2 that ferrite loaded patch antenna can demonstrate beam scanning. In this section, both of the above concepts are combined to design a FPC antenna with dielectric-ferrite superstrate and excited by a MPA. Fig. 27 shows the schematic diagram of the FPC with multilayer dielectric-ferrite superstrate and excited by a 10 GHz MPA.

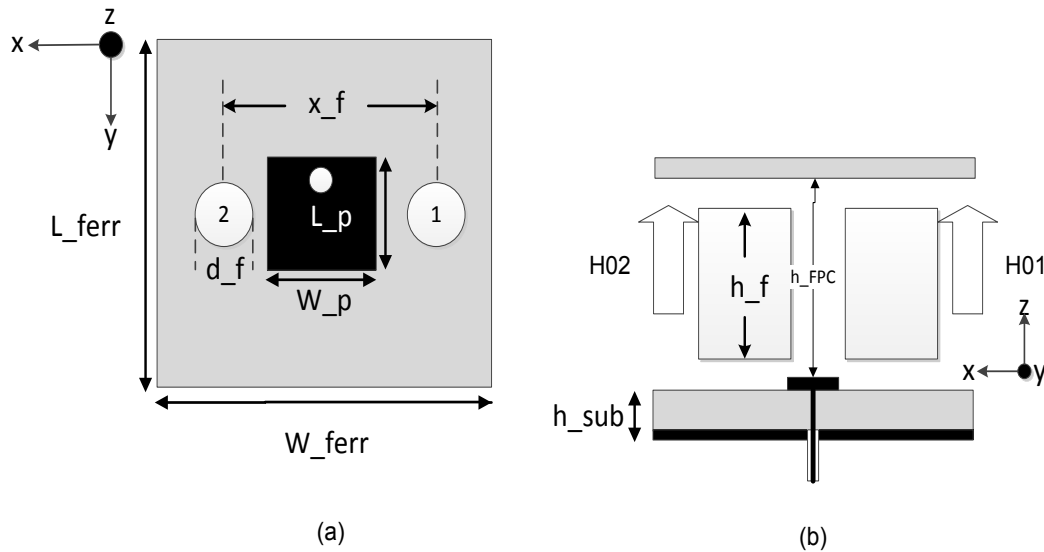


**Figure 27. FPC filled with magnetized ferrite rods excited by a 10 GHz MPA, (a) Top view, and (b) Side view.**

In this design, the FPC is created by placing a Duroid superstrate ( $\epsilon_r=2.2$ , thickness of 0.8mm) at a height,  $h_{FPC} = 16\text{mm}$  above the 10 GHz radiating patch. The two Y220 ferrite cylinders with  $d_f = 6\text{mm}$  and  $h_f = 10\text{mm}$  are then placed inside the newly formed

cavity as lower layer of the superstrate. The rest of the design parameters, shown in Fig. 27, are kept the same according to Section 4.2.1. Fig. 28 shows the simulated reflection characteristics of the designed FPC antenna, in comparison to the ferrite loaded (non-FPC) antenna presented in Section 4.2. As observed, transformation from non-FPC to FPC antenna with optimally excited cavity slightly affects the resonance frequency and the impedance matching of the structure, as seen in Fig. 28.

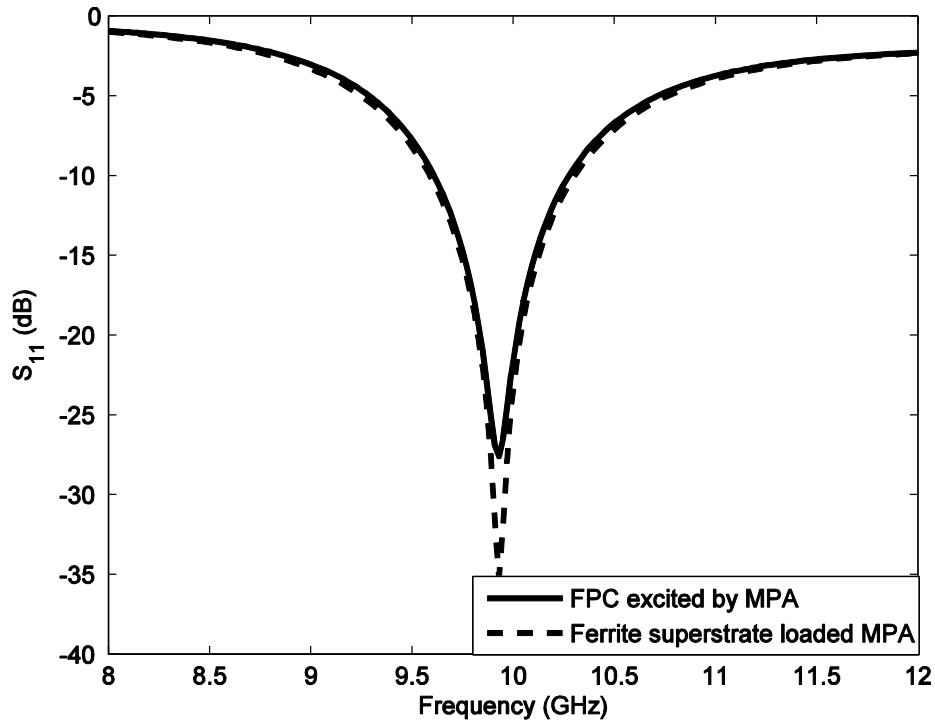


Figure 28. Simulated reflection responses of magnetized ferrite loaded FPC and ferrite superstrate loaded (non-FPC) 10 GHz MPA.

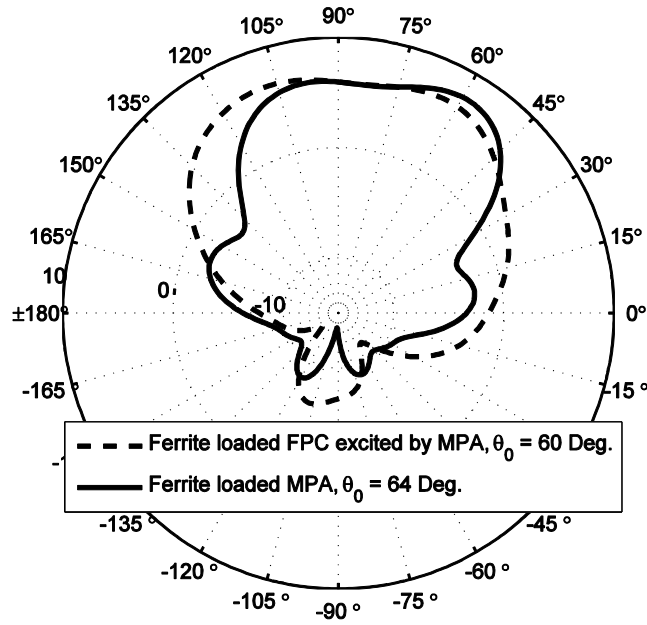
### 4.3.1 Results

The structures presented in Fig. 18 and Fig. 27 are optimized using HFSS software and a comparison of the directivity patterns is presented in Table 4.

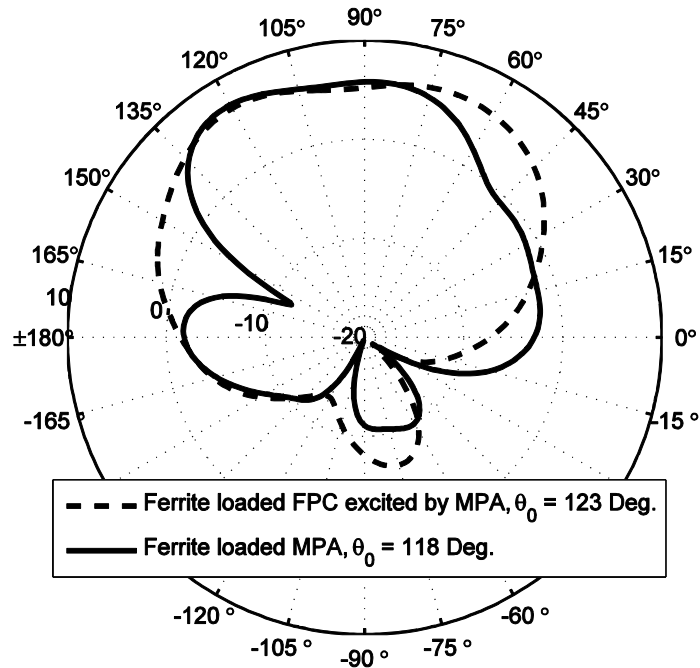
**Table 4. Radiation characteristics comparison for the three different MPA designs.**

	<b>HPBW (Deg.)</b>	<b>Directivity (dB)</b>	<b>Efficiency (%)</b>
MPA (without any loading or superstrate)	60	6.687	81.6
Ferrite Loaded MPA (without dielectric superstrate layer, considered as non-FPC )	61.4	7.139	77.83
Ferrite Loaded FPC excited by MPA (with dielectric superstrate layer)	62.3	7.596	75.46

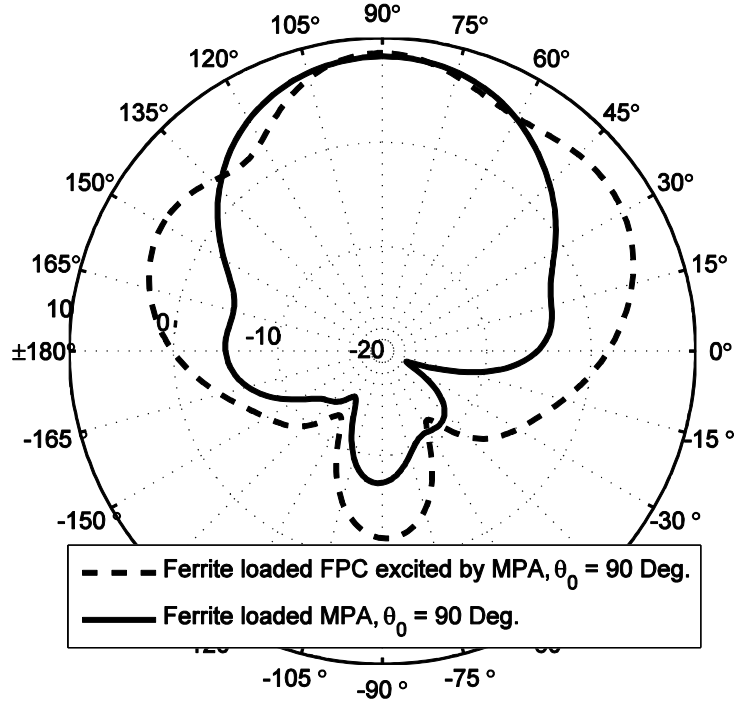
As observed from the results of Table 4, placement of the FPC leads to an immediate increase of 1.39 dB in the directivity of the patch antenna structure. However this slightly reduces the radiation efficiency due to the cavity resonance. Compared to the design of Section 4.2, the ferrite loaded FPC design offers an increase of 0.457 dB in the directivity at the cost 2.37% reduction in antenna efficiency. Magnetizing one of the ferrite rods (H01 or H02) leads to a beam scan, similar to the one observed for the non-FPC case of Section 4.2. Fig. 29 shows a comparison of the simulated directivity patterns for the ferrite loaded MPA (non-FPC) and the ferrite loaded FPC antennas.



(a)



(b)



(c)

Figure 29. Simulated radiation patterns for maximum beam scans for the magnetized ferrite loaded FPC and the ferrite loaded 10 GHz MPA (a)  $H_{01} = 0$  and  $H_{02} = 0.19T$ , (b) for  $H_{01} = 0.19T$  and  $H_{02} = 0T$ , and (c)  $H_{01} = 0$  and  $H_{02} = 0$ .

Note that the scan properties (Fig. 29 a, b) for the ferrite loaded non-FPC design and the FPC design are different due to the cavity resonance. Although the FPC case demonstrates slightly higher directivity (0.4 dB as observed in Fig. 29c) in the broad side direction, its scan behavior becomes ambiguous due to cavity resonance. Moreover, by placing an FPC over the MPA, the overall antenna structure height becomes 16 mm instead of the 36 mm for the non-FPC case shown in Fig. 18. Thus, it is essential to optimize the FPC antenna to improve the scan characteristic. In the following Chapter, a 2x1 thinned array of microstrip patches is used to optimally excite the ferrite loaded FPC antenna.

## 4.4 Conclusion

Magnetic dipoles of a biased ferrite material have the ability to interact with the passing RF signals resulting in a change in the wave properties; phase and magnitude. As observed in a conventional antenna array, where a change in the main beam direction is directly related to the progressive phase shift ( $\beta$ ), which produces a phase taper in the dominant component of the radiated field. For a single patch antenna, progressive phase shift is not realizable and a superstrate based beam scan is necessary. In this chapter, magnetized ferrite-foam based superstrate was designed and used to realize beam scan. Using professional software (HFSS), it is demonstrated that by optimally positioning the ferrite rods, a main beam scan beam scan, proportional to the difference in the axial magnetizing fields can be achieved. The designed 10GHz single patch antenna with ferrite-foam superstrate demonstrated a broadside beam scan of  $\pm 30^\circ$  for a with a half power beam width (HPBW) of  $60^\circ$  for a differential biasing field of  $\Delta H = 0.22T$ . The loss in broadside directivity due to the presence of biased the superstrate is observed to be 0.25 dB. The

fabricated antenna structure showed maximum beam scans of  $+28^\circ$  and  $-26^\circ$  degrees for separate biasing values of  $H_{01} = 0.19\text{T}$  and  $H_{02} = 0.19\text{T}$ , respectively. By placing a multilayer FPC over the radiation path of the MPA, an increase of 1.39 dB in the directivity of the structure is observed. Placing magnetized ferrite rods inside the FPC (as foam-ferrite layer) shows a beam scan of  $+33^\circ$  and  $-30^\circ$  for biasing fields of  $H_{01} = 0.19\text{T}$  and  $H_{02} = 0.19\text{T}$ , respectively. In addition to an increase in the structure's directivity, the FPC based design also results in a low profile (overall height of 16mm) antenna as compared to the non FPC case. The radiation patterns of the FPC excited by the MPA suggest that in order to have well defined directivity patterns and clear beam scan, the ferrite loaded FPC should be optimally excited by multiple sources. This will be investigated in the following chapter.

## CHAPTER 5

# FERRITE LOADED FPC ANTENNA EXCITED BY AN ARRAY

FPC antennas are popular in wireless base stations [69] because of the higher directivity realized without complicated feed mechanism. In an FPC structure, introducing beam scanning using phased array technique results in unacceptable SLLs that increase with the scan angle to become grating lobes. These grating lobes are often due to exciting the FPC with thinned microstrip array with larger inter-patch separation distance ( $d > 0.5\lambda$ ). To avoid the compromise between the optimum excitation and the scan capability of the FPC antenna, the cavity can be loaded with magnetized material to introduce superstrate based beam scanning. This chapter discusses the scan capabilities of a directive FPC antenna with composite superstrate made of dielectric, ferrite and foam materials. Section 5.1 has an overview of FPCs, Section 5.2 presents the results of FPC antenna design with beam scanning abilities as well as side lobe suppression and Section 5.3 concludes this chapter. Professional simulator (HFSS) is used to demonstrate directive beam scan with acceptable

side lobe levels, where magnetized ferrite rods are used to realize the beam scan and stepped dielectric superstrate is used to further reduce the side lobe level.

## 5.1 Fabry-Perot Cavities (FPC)

Traditionally, base station antennas consist of an array of dipole or microstrip patches to improve the antenna directivity and control the beam shaping properties [70]. However, these array antennas require complicated feed networks with unwanted energy loss. Recently, directive cavity antennas with a simpler feeding mechanism have been proposed as an alternative. FPCs generally consists of a half-wave cavity formed between a partially reflecting superstrate and a ground plane and excited by an array of microstrip radiating elements, optimally located within the cavity. By reducing the number of array elements, complexity and losses from the array feeder network can be minimized.

### 5.1.1 Characterization of an FPC Excited by an RF source

Consider an FPC formed between two partially reflecting surfaces (PRS) separated by a distance ' $D$ ' as shown in Fig. 30. Boutayeb et. al in [71] have used the frequency and angular response of this FPC using a plane wave source in the form of a monopole placed in the center of this cavity. The PRS consists of an array of wires with periodicity  $P$  and diameter  $a$ . The plane waves radiated by the source travel in all directions,  $\theta$ , and interact (reflect/transmit) with the PRS giving rise to transmission and reflection coefficients;  $t$  and  $r$  respectively. Assuming  $t$  to be the amplitude of the directly transmitted signal, the once reflected signal from the PRS can be mathematically written as (37) [71],

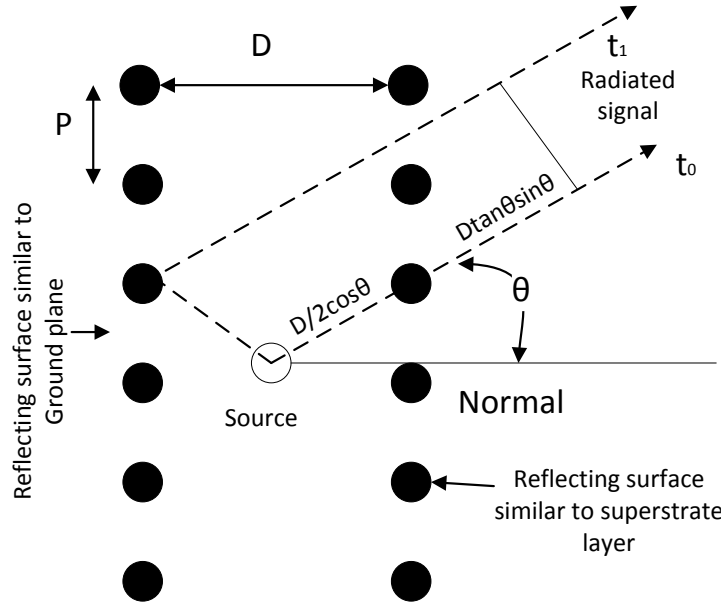


**Figure 30. An FPC formed between two PRS and excited by a monopole antenna placed in the center of the FPC.**

$$t_1 = tr e^{jkD \cos \theta} \quad (37)$$

where  $k = \frac{2\pi}{\lambda}$ ,  $\theta$  is the angle of the transmitted wave with respect to the normal and  $D$  is the cavity length. After  $n$  reflections, the amplitude of the transmitted signal can be written as (38),

$$t_n = tr^n e^{jnkD \cos \theta} \quad (38)$$

The total amplitude of the transmitted signal,  $T$ , can be calculated by summing up all the individual  $t$ 's as in (39),

$$T = \sum_{i=0}^n t_i = \frac{t}{1 - r e^{-jkD \cos \theta}} \quad (39)$$

The total transmitted amplitude of (39) can be used to determine the operating characteristics of this type of a structure

## 5.1.2 Traditional Scanning of FPC antenna

Traditional beam forming using microstrip phased array is well established, where radiating patches are separated by at least half a wavelength ( $d \leq \lambda/2$ ) and excited with signals having constant phase progression ( $\beta$ ). An increase in the directivity can be achieved by increasing 'd', while reducing the number of radiating elements within the same antenna aperture; resulting in thinned antenna arrays. This not only reduces the feed complexity, the additional space between radiating elements of a thinned array enables placement of phase shifter and other circuitry on the antenna aperture. When thinned array is used to excite a FPC, phased array technique fails to realize acceptable beam scanning properties due to the generation of grating lobes.

A highly directive 64x20mm<sup>2</sup> FPC is shown in Fig. 31, where a 16mm cavity ( $\cong \lambda/2$ ) is formed between the GND plane and the partially reflective dielectric superstrate with  $\epsilon_r=2.2$  and  $h=0.8$  mm. The cavity is filled with air-foam composite material with  $\epsilon_r=1.01$ . A thinned 2x1 microstrip linear array on  $\epsilon_r=2.2$  and  $h=1.6$  mm substrate is used to excite the 10 GHz FPC antenna. For optimal excitation, the mutual coupling between the patches is reduced by increasing their separation distance (d). Fig. 32 plots the simulated radiation pattern and the reflection response of the FPC with  $d=0.5\lambda$  and  $0.8\lambda$ . As expected, increasing separation distance (d) improved the directivity of the FPC antenna by 1.6 dB.

To introduce beam scanning using phased array technique, phase shifter network is used to provide phase progression ( $\beta$ ) of the patch excitation signals. Fig. 33 plots the radiation patterns of the designed FPC antenna with  $d=0.8\lambda$ . Note that although  $\beta=\pm 80$  degrees steers the main beam towards  $\theta=\pm 12^\circ$  ( $\theta_0 = 102^\circ$  &  $78^\circ$ ), it increases the side lobe

level by 6.42 dB compared to that of broad side radiation ( $\theta=90^\circ$ ). So, unlike an ordinary 2x1 phased array, SLL of the FPC considerably increases with increasing scan angle of the main beam. The relationship of the patch separation distance and the side lobe level of the FPC antenna are plotted in Fig. 34. It is clear from this figure that increasing patch separation distance improves the directivity but deteriorates the side lobe level during beam steering. Thus, for an FPC antenna, the design parameter that improves the directivity becomes the limiting factor of its beam scanning capabilities.

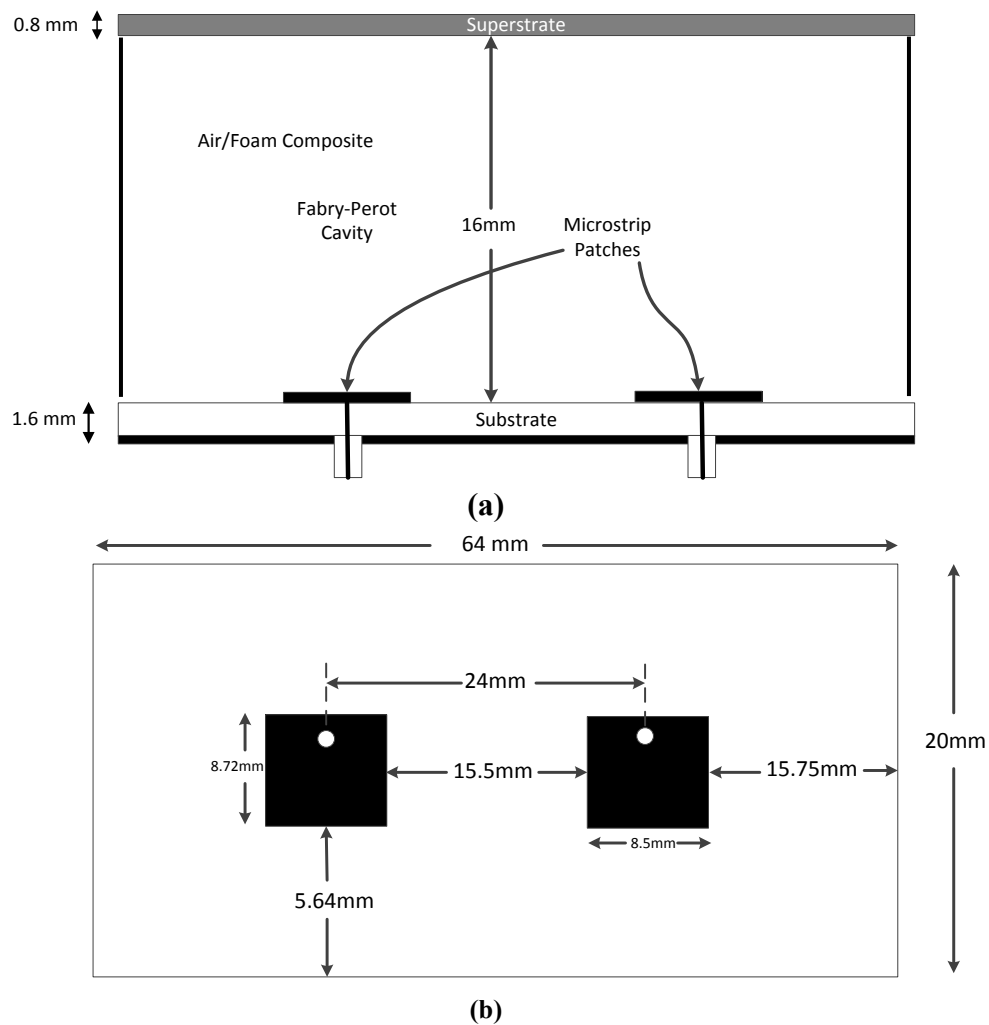
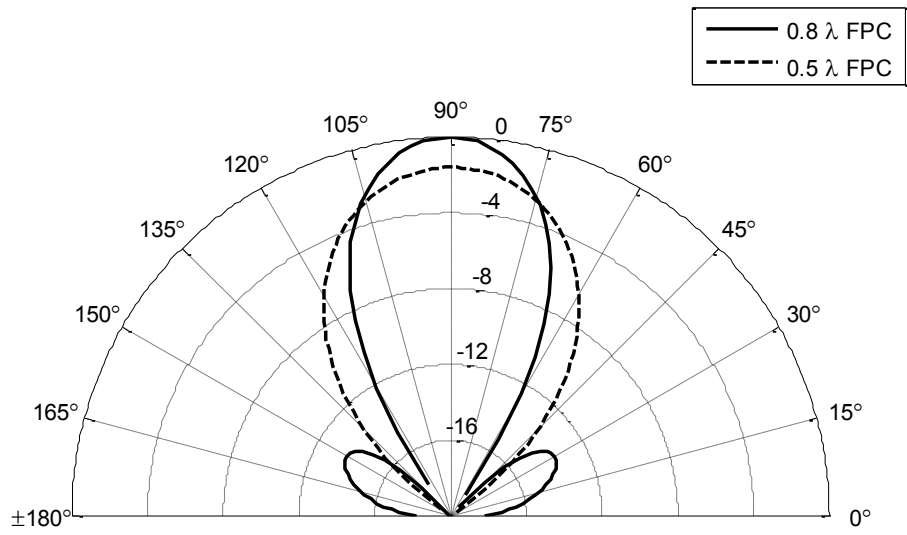
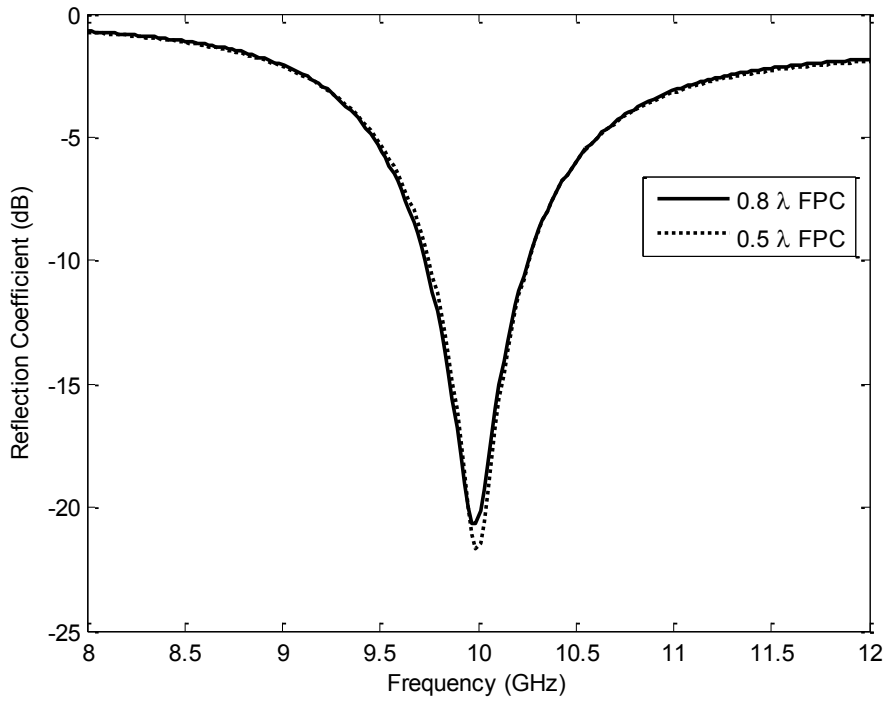


Figure 31. Schematic diagram of the FPC excited by 2x1 thinned microstrip array (a) side view, (b) top view.



(a)



(b)

Figure 32. (a) Simulated normalized radiation pattern (dB) and (b) simulated reflection response (S11), of the designed FPC with  $d=0.8\lambda$  and  $0.5\lambda$ .

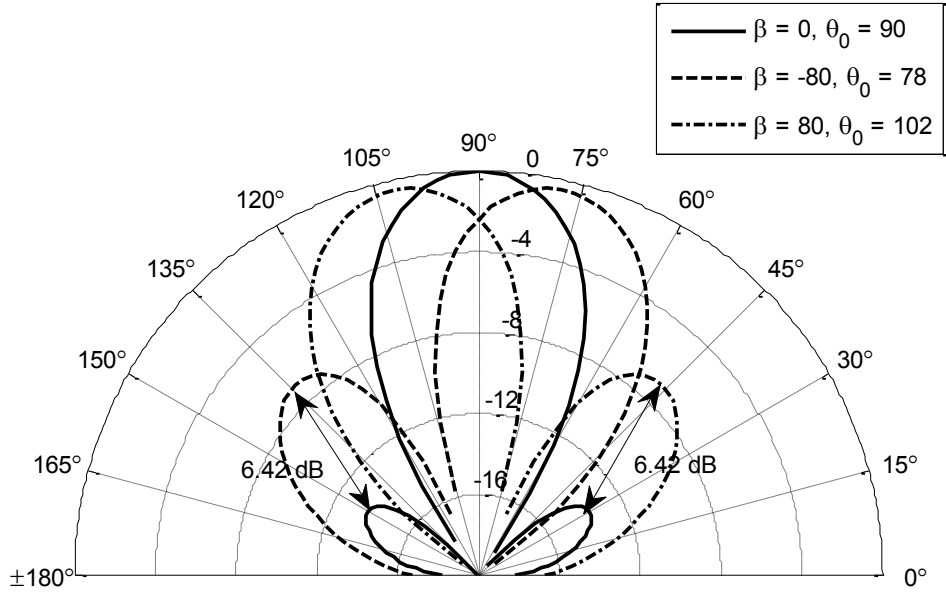


Figure 33. Normalized simulated radiation patterns of the FPC with  $d=0.8\lambda$

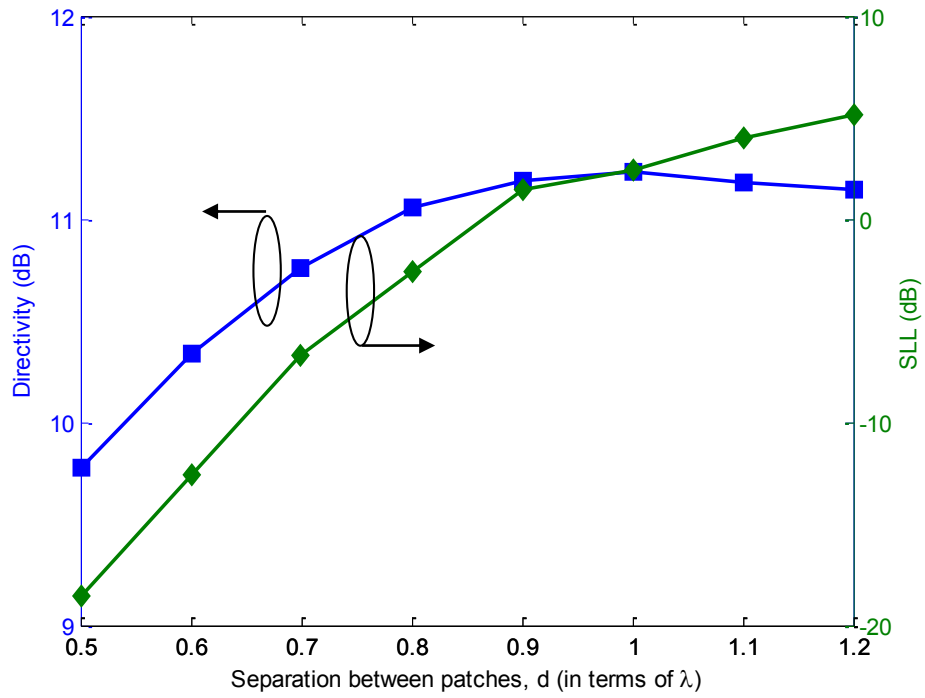


Figure 34. Patch separation distance versus the side lobe level (dB) and directivity (dB) of a FPC.

## 5.2 Simulated and Measured Results

### 5.2.1 Beam Scanning 2- Patch FPC Antenna with Uniform Superstrate

The alternative beam scanning mechanism proposed here depends on perturbing the radiated fields from the 2x1 thinned array exciter of the FPC as shown in Fig. 35. This can be achieved by loading magnetized ferrite rods within the FPC to introduce controlled perturbation of the  $E_y$  field components through gyromagnetic interaction. Optimal loading of ferrite rods require thorough understanding of the field distribution within the cavity and how they are related to the steering of the main beam. Fig. 36(a,b) plots the un-perturbed and perturbed magnitude and phase of the  $E_y$ -field along an x-axis observation line above the 2x1 traditional antenna array aperture.

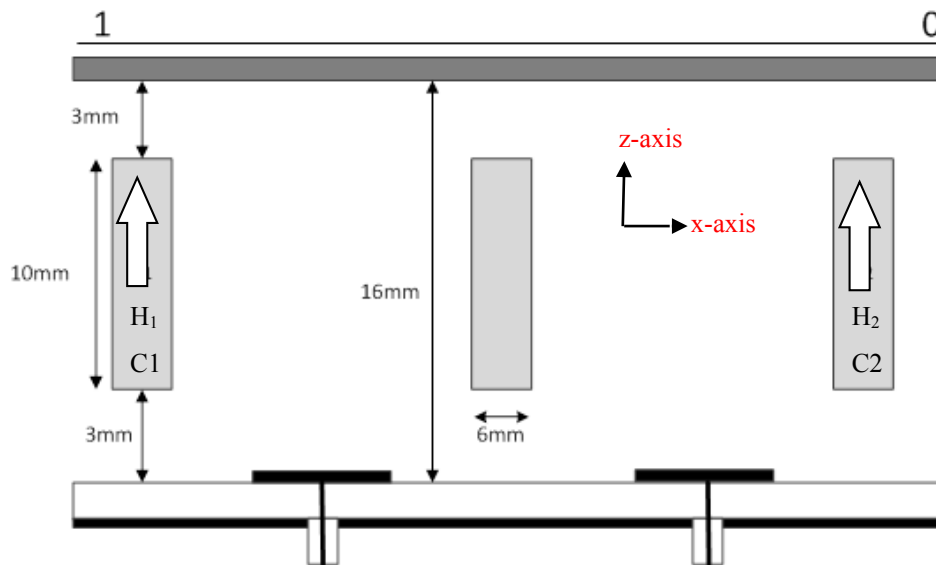
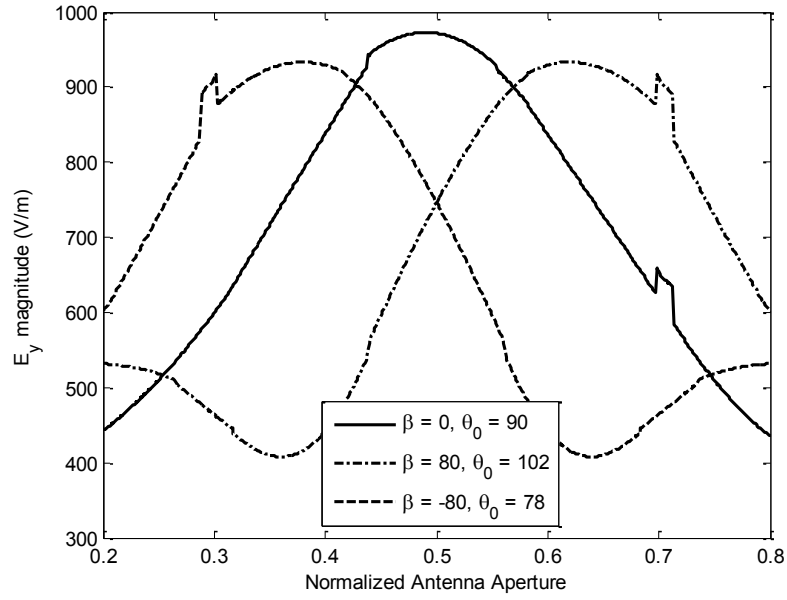


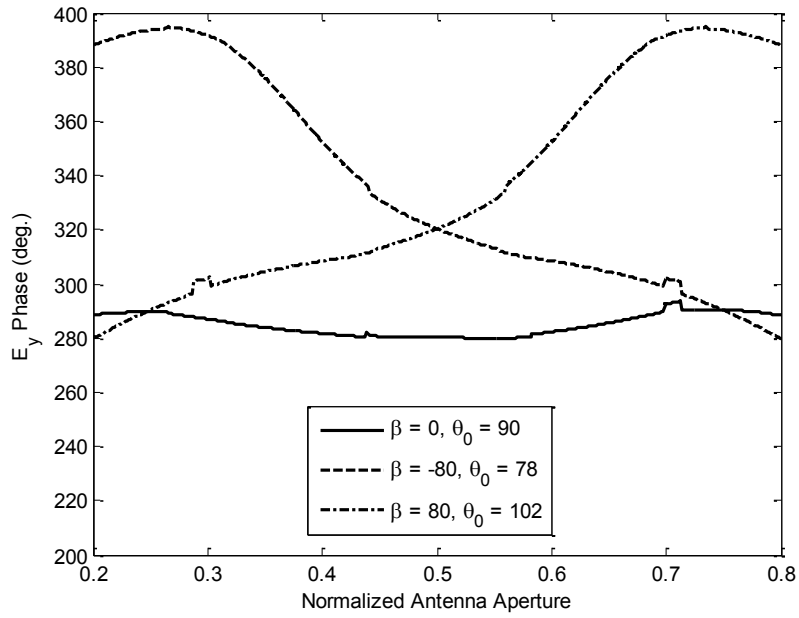
Figure 35. Side view of the FPC loaded with multilayer dielectric-ferrite composite.

Fig. 36(a) plots the magnitude of the radiated  $E_y$ -field for  $\theta_0=102^\circ$ ,  $90^\circ$  and  $78^\circ$ . The related phase distributions of the  $E_y$ -fields are plotted in Fig. 33(b). Note that these field distributions correspond to the radiation patterns plotted in Fig. 30. From the phase plots of Fig. 36(b), a phase taper is apparent as the main beam of the antenna scans in either of the azimuth directions.

Fig. 37 plots the corresponding  $E_y$  magnitude and phase for the ferrite loaded FPC. As observed, biasing one of the ferrite rods to 0.22 T (200 kA/m) results in beam scans of  $\pm 12^\circ$  with HPBW's of  $37^\circ$  and  $36^\circ$  respectively. Like Fig. 36(b), a phase taper also results; indicating the phase change caused by the ferrite rods. A 2-D directivity pattern for the ferrite supestrate based FPC for different directions of beam scan is provided in Fig. 38. During beam scanning, the SLL increases to 4.747 dB and 4.115 dB for a main beam direction of  $102^\circ$  and  $78^\circ$  respectively, as compared to 3.234 dB without beam scan.

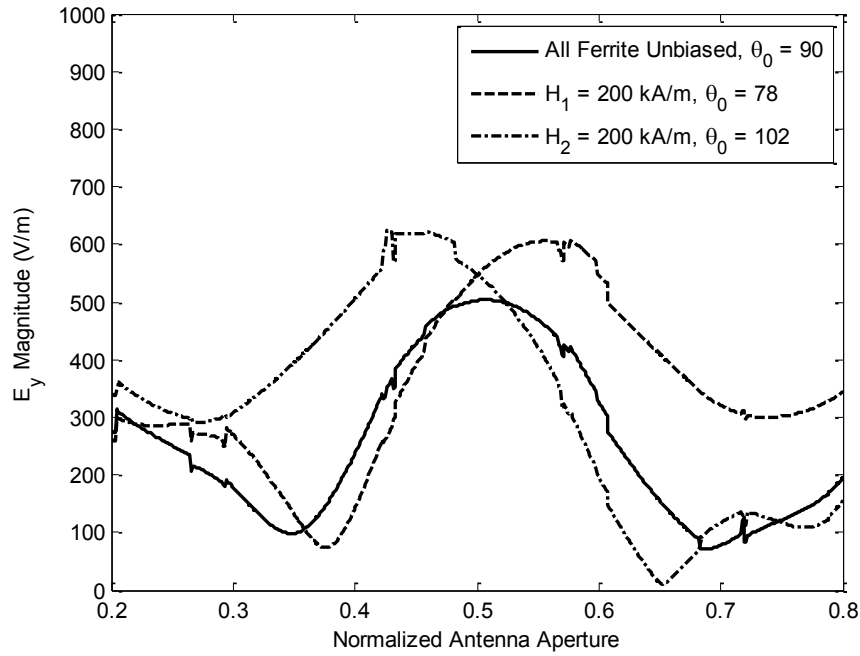


(a)

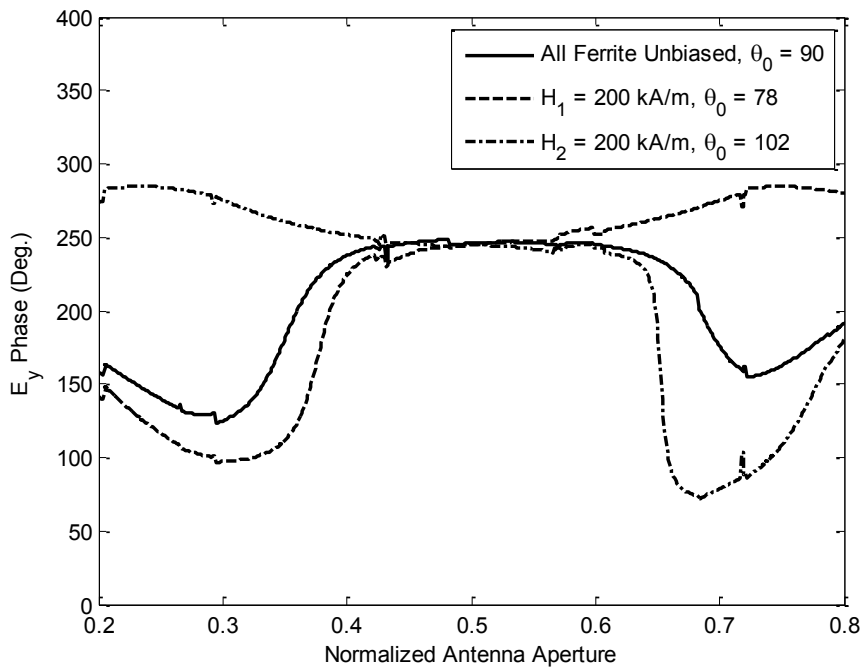


(b)

Figure 36.  $E_y$ -field distribution for the steered beams observed along a broadside x-axis line, located above the 2x1 array surface (a)  $E_y$  magnitudes, and (b)  $E_y$  phases.



(a)



(b)

Figure 37. Ferrite loaded FPC (a)  $E_y$  magnitude along the observation line (b)  $E_y$  phase along the observation line.

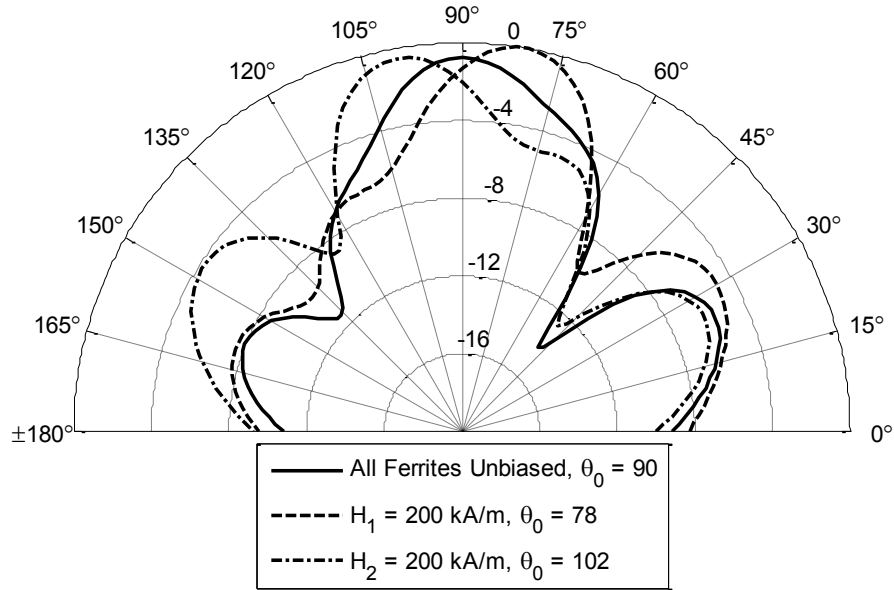


Figure 38. Simulated radiation patterns for the ferrite loaded FPC antenna for different biasing fields.

The measured S-parameters of the thinned 2-patch antenna array are presented in Fig. 39. As observed, both the elements resonate at the operating frequency of 10 GHz with respective -10 dB bandwidths of 1.16 GHz and 860 MHz.

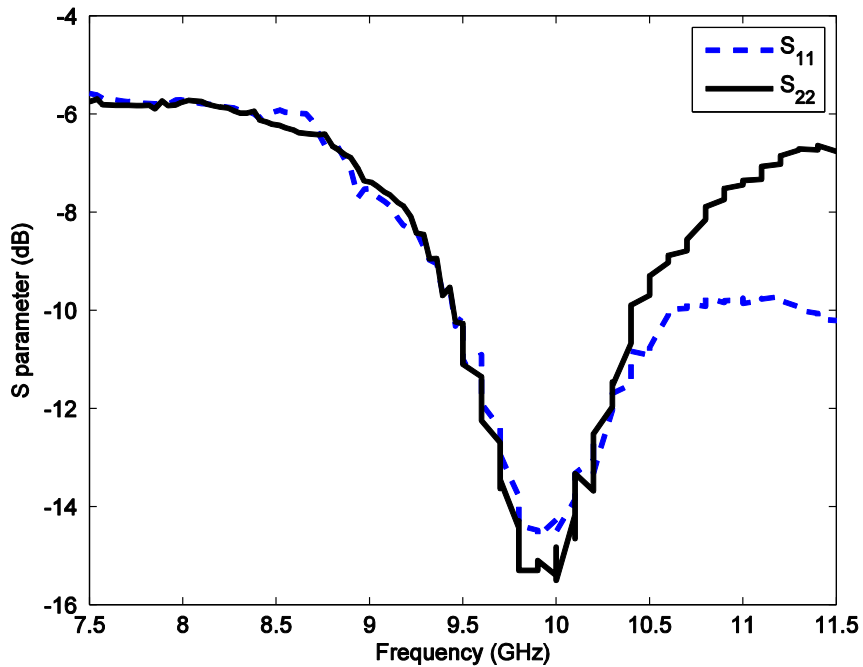


Figure 39. Measured S-parameters for both elements of the thinned 2-patch antenna array.

The FPC is also created by using a uniform Duroid superstrate and the 2-D radiation pattern measurements are successfully performed. The measured 2-D radiation patterns for the FPC excited by thinned 2-patch antenna array are provided in Fig. 40. Depending on which ferrite rod is biased (H01 or H02), a biasing of 0.22T (200 kA/m) results in a maximum beam scan of + 14° and - 12° corresponding to a directivity of 8.51 dB and 8.68 dB respectively. A snapshot of the FPC with the thinned 2-patch antenna array is presented in Fig. 41. Styrofoam is used to keep the ferrite rods and the superstrate firmly in place over the antenna array.

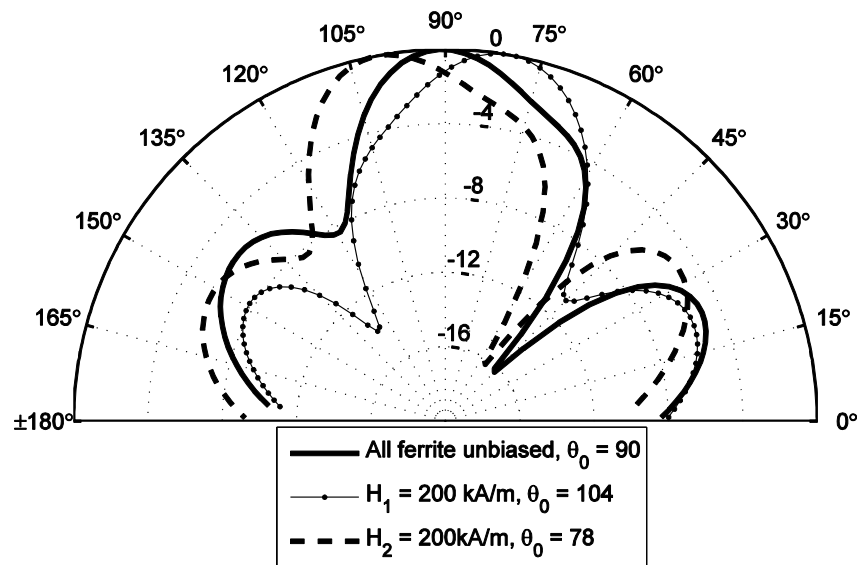


Figure 40. Normalized measured radiation patterns for the FPC excited by thinned 2-patch antenna array.

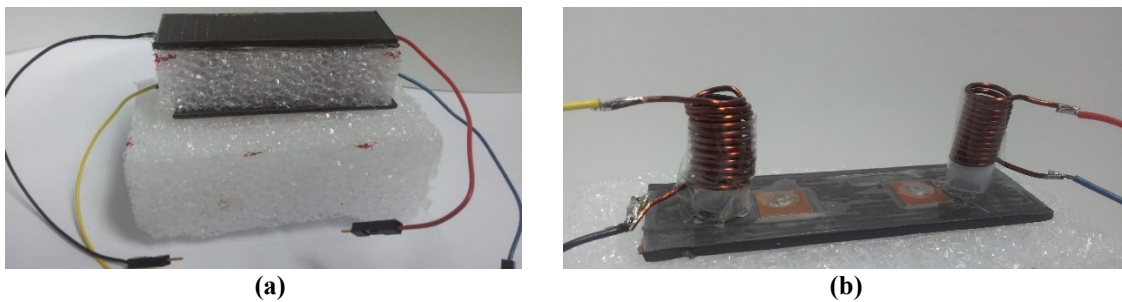


Figure 41. Snapshot of the fabricated ferrite loaded FPC excited by a thinned 2-patch antenna array with (a) Styrofoam packing, and (b) only biasing coils of the two ferrite rods.

### 5.2.3 Side-Lobe Suppression

Observing the directivity patterns of the scanned beam presented in Fig. 40, it is obvious that a significant side lobe is present in the direction of beam scan. In order to minimize this side lobe a stepped dielectric superstrate can be used. High dielectric constant materials have the property to reduce the signal intensity by attenuating the RF signals passing through it. So, by carefully designing the stepped dielectric superstrate by using high  $\epsilon_r$  materials towards the edges, spurious radiations resulting in side lobes, can be significantly reduced, resulting in a decrease in the SLL.

Fig. 42 shows the schematic diagram (side view) of the FPC with stepped dielectric superstrate consisting of two dielectric materials,  $\epsilon_{r\_D1} = 15.4$  and  $\epsilon_{r\_D3} = 15.4$ . In order to determine the exact dimensions,  $L_{d1}$  and  $L_{d2}$  of the superstrate, a parametric simulation study was performed; the aims being maximizing the gain and minimizing the SLL. The results of the parametric study are provided in Fig. 43.

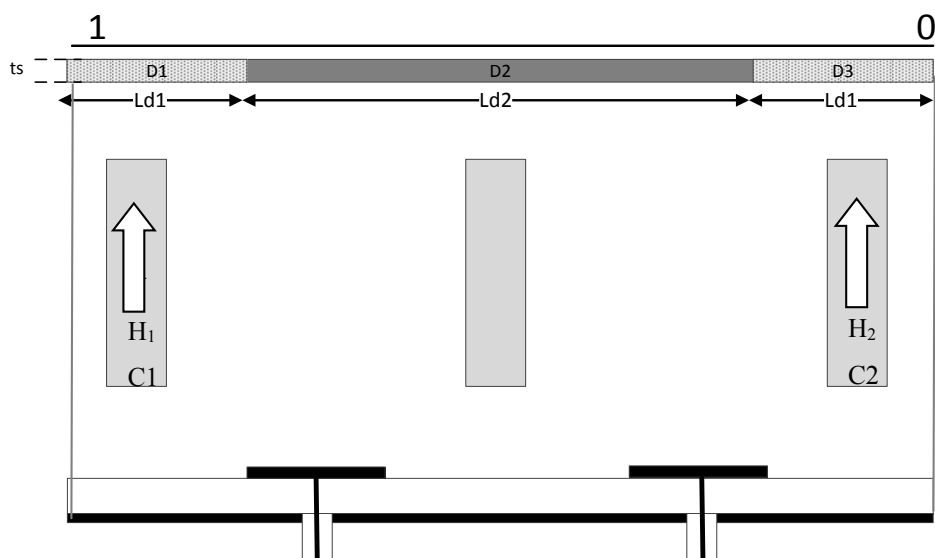
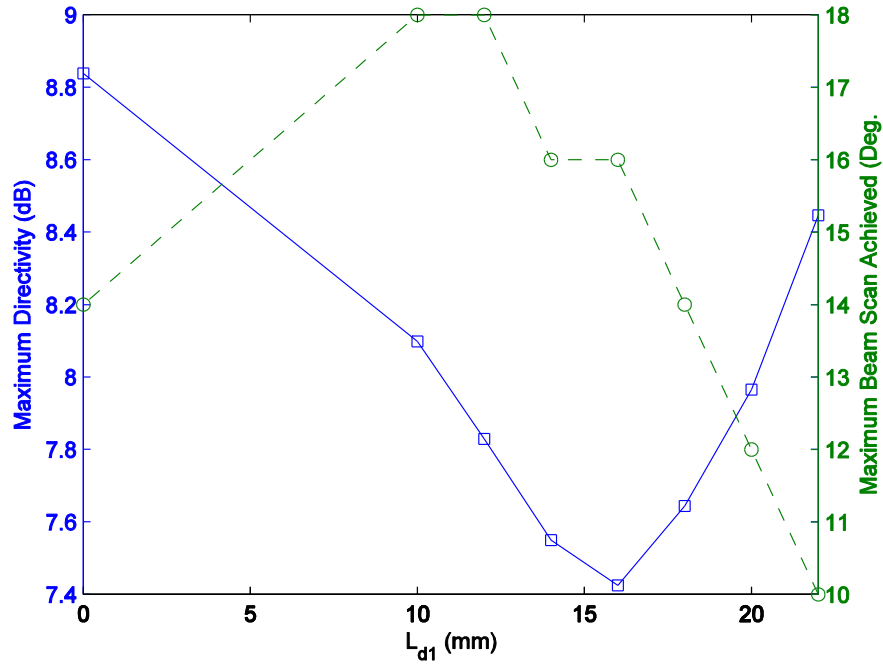
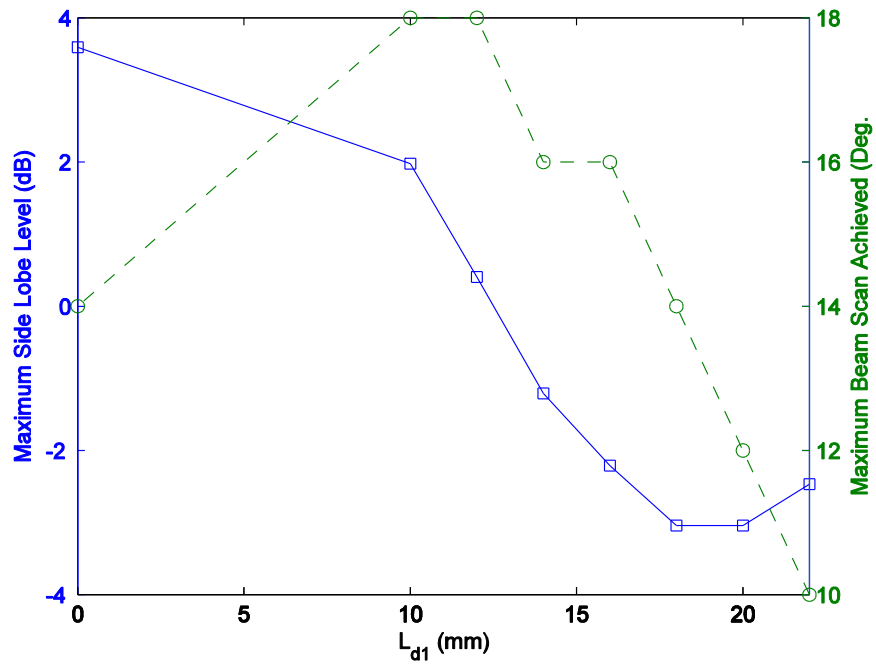


Figure 42. Schematic of an FPC antenna with air-ferrite and stepped dielectric superstrate layers.



(a)

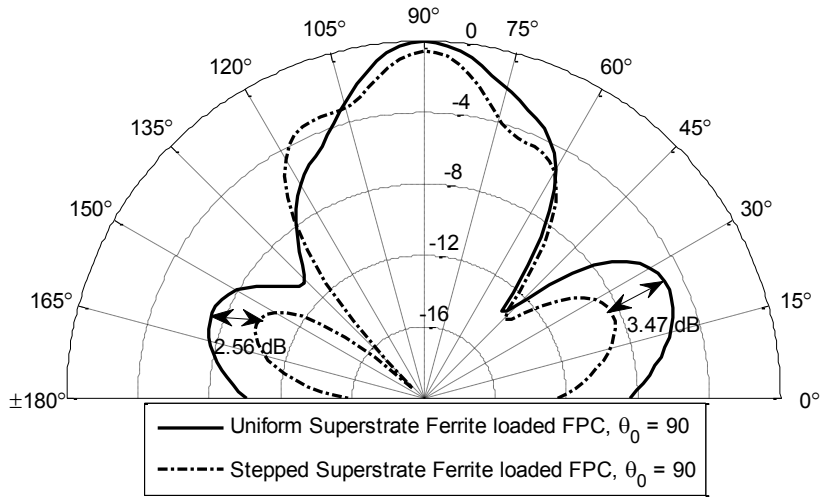


(b)

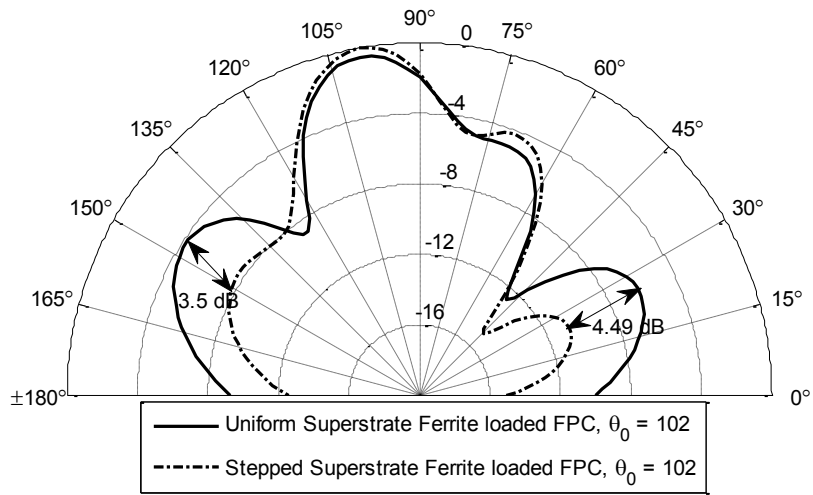
Figure 43. Parametric sweeps for the selection of stepped superstrate dimension,  $L_{d1}$ , when  $H_2 = 150$  kA/m (a) Maximum directivity and beam scan and (b) Maximum SLL and beam scan.

For the parametric study of Fig. 43,  $H_2$  was set to 0.18 T(150 kA/m); causing the main beam to move to  $114^\circ$ . The parameter  $L_{d1}$  is varied and its effects on the maximum gain, the SLL and the direction of the main beam are observed. From Fig. 43 (a) it is seen that as  $L_{d1}$  increases, the directivity of the main beam starts to decrease from 8.8384 dB (single superstrate) to 7.4249 ( $L_{d1} = 16\text{mm}$ ), a further increase results in an increase in the gain. The amount of beam scan increases initially (till  $L_{d1} = 12\text{mm}$ ) but starts to decrease as the high dielectric material length is increased further ( $L_{d1} > 12\text{mm}$ ). A view of the SLL indicates a sharp decrease until  $L_{d1} = 18\text{mm}$ , after which a slight increase is observed. Considering the SLL, the maximum beam scan and the directivity,  $L_{d1} = 18\text{mm}$  provides an acceptable directivity of 7.6438 dB with a SLL of -3.0412 (the least) with a beam scan of  $14^\circ$ .

The 2-D directivity plots of the FPC are shown in Fig. 44. In Fig. 44(a), the broad side radiation pattern related to unbiased ferrite cylinders demonstrated the reduction of main lobe by 0.6 dB. However, the related decreases in the SLL's is observed to be much higher (2.56 dB and 3.47 dB respectively). For biased ferrites with  $H_2 = 0.22\text{T}$  (200 kA/m), Fig. 41(b) shows that the stepped superstrate improved directivity by 0.5 dB due to considerable reduction of SLL's (3.5 dB and 4.49 dB).



(a)



(b)

Figure 44. Improved simulated radiation patterns of the FPC antenna with tapered dielectric superstrate, (a) unbiased ferrite and (b) ferrite biased with external magnetizing field of  $H_2 = 200$  kA/m.

## 5.3 Conclusion

Beam scanning of traditional antenna arrays requires the use of phase shifters to induce the required progressive phase shift. Thinning the antenna arrays provides higher directivity but results in higher SLLs when scanning is performed using traditional phase shifter method. In this chapter a unique antenna design employing biased ferrite cylinders contained inside an FPC is presented. By biasing one of the ferrite cylinders, the main beam

of the antenna can be scanned up to  $\pm 12^\circ$  for a biasing value of 0.22T. Measured values of the fabricated antenna show similar beam scans and HPBW values. Moreover, by carefully designing a stepped dielectric superstrate (comprising of high loss material towards the edges), the SLL can be reduced significantly ( $\approx 3.56$  dB) while maintaining acceptable directivity and beam scan.

## CHAPTER 6

# FERRITE SUPERSTRATE WITH INTEGRATED SPLIT-RING RESONATOR

The simulation and measurement results presented in Chapter 4 and 5 prove the concept that the magnetized ferrite rod loaded FPC can produce beam scan. Observing the design specifications in Chapter 4, the minimum height required for the FPC is  $0.5\lambda$ . At the operating frequency of 10GHz, this cavity height is significant ( $\approx 1.5$  cm) and makes the antenna design seems bulky. In this chapter, split-ring resonators (SRR) are integrated with the magnetized ferrite rods to reduce the height of the FPC. Section 6.1 presents the theoretical background related to the design of the split ring resonator. Section 6.2 has the SRR design specifications; Section 6.3 presents the results of the SRR embedded ferrite rods with a single 10 GHz MPA; Section 6.4 presents the details of FPC loaded with ferrite rods with integrated SRR's excited by a 2-patch antenna array; Section 6.5 has comparisons between the presented FPC designs and Section 6.6 concludes this chapter.

## 6.1 Split-Ring Resonators (SRR)

Metamaterials are periodic arrangements of metallic geometrical shapes, called unit-cells, with specific dimensions that collectively exhibit certain electromagnetic properties. The size of the individual unit-cell is comparable to the wavelength of the operating RF signal(s) and act as the atoms and molecules of the new engineered medium [72] [73]. As a transmitting RF signal passes through a metamaterial, oscillating electric and magnetic fields in the tiny unit-cells give rise to collective electromagnetic characteristics that can be tuned by modifying the dimensions of the unit-cell. Metamaterials are used to achieve negative refractive indexes [74] [75], cloaking [76] and artificial magnetism [77]. Among the different unit-cells utilized to create metamaterials, SRR [72] is the most commonly used structure to attain negative magnetic properties. Pendry proposed that negative refractive index material could be realized by utilizing arrays of microscopic SRRs. A typical SRR acts as an LC circuit with a magnetic coil of inductance  $L$  and a capacitor with capacitance  $C$ . Fig. 45 depicts this graphically,

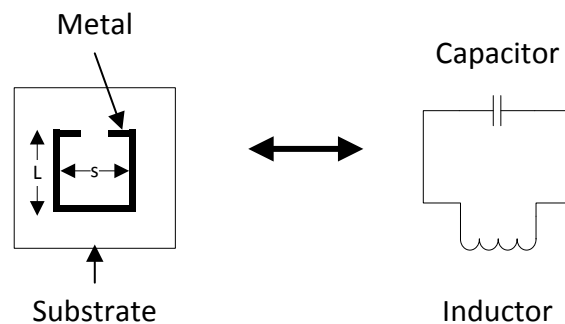


**Figure 45. A single SRR unit-cell with an equivalent LC circuit representation**

Under the influence of an incident E-field, parallel to the gap of the SRR, coupling takes place between the SRR capacitance and the E-field resulting in an oscillating current in the split-ring. This oscillating current induces a magnetic field in the base of the SRR, which also interacts with the external (RF) field generating LC resonance. For an SRR of trace length  $l$ , trace width  $w$ , trace thickness  $h$  and gap separation  $s$ , fabricated on a substrate of dielectric constant  $\epsilon_r$  as shown in Fig. 43, the equivalent capacitance and inductance is given by [78] as,

$$C = \epsilon_0 \epsilon_r \frac{wh}{s} \quad (40)$$

$$L = \mu_0 \frac{l^2}{h} \quad (41)$$

So, for an equivalent LC circuit, the LC resonance frequency is given by,

$$\omega_{LC} = \frac{1}{l} \sqrt{\frac{s}{w}} \frac{c}{\sqrt{\epsilon_r}} \quad (42)$$

where,  $c$  is the speed of light. As observed from (42), the resonance frequency of an SRR unit-cell depends only on the physical dimension and not on the conductive properties of the metal that forms the rings.

## 6.2 Design of a 10 GHz Split-Ring Resonator

An SRR, in its simplest forms, is a highly conductive metallic ring with multiple insertions [79]. When a time varying magnetic field perpendicular to the plane of the SRR is incident on the SRR surface, a current gets induced in the ring. Due to the gap/insertion and the continuously varying RF magnetic field, the current starts to change direction every

cycle storing charge in the gap. The alternating electric field build up due to this stored charge induces an alternating magnetic field within the area enclosed by the ring and hence resonates. A large number of periodic repetitions of this SRR unit-cell behave as an effective medium with a negative  $\mu_{\text{eff}}$ . Fig.46 shows a properly labelled schematic of the SRR designed to resonate at 10 GHz.

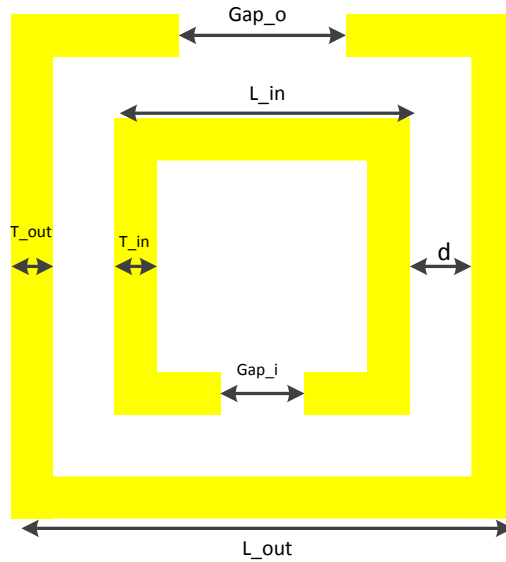


**Figure 46. Schematic of double ring based SRR with  $\text{Gap}_o = 0.3\text{mm}$ ,  $\text{Gap}_i = 0.3\text{mm}$ ,  $L_{\text{out}} = 2\text{mm}$ ,  $L_{\text{in}} = 1.5\text{mm}$ ,  $d = 0.15\text{mm}$ ,  $T_{\text{in}} = 0.2\text{mm}$  and  $T_{\text{out}} = 0.1\text{mm}$ .**

The dimensions of the designed SRR unit cell are selected based on the design procedure presented in [80], making sure that maximum transmission takes place at 10 GHz. Looking at the simulated transmission characteristics of the SRR structure in Fig. 47, we see the designed SRR has good transmission (-0.931 dB) at 10 GHz. Smith et. al in [80] have derived analytical expressions for determining the electromagnetic properties of metamaterials from the  $S$ -parameters of a structure.

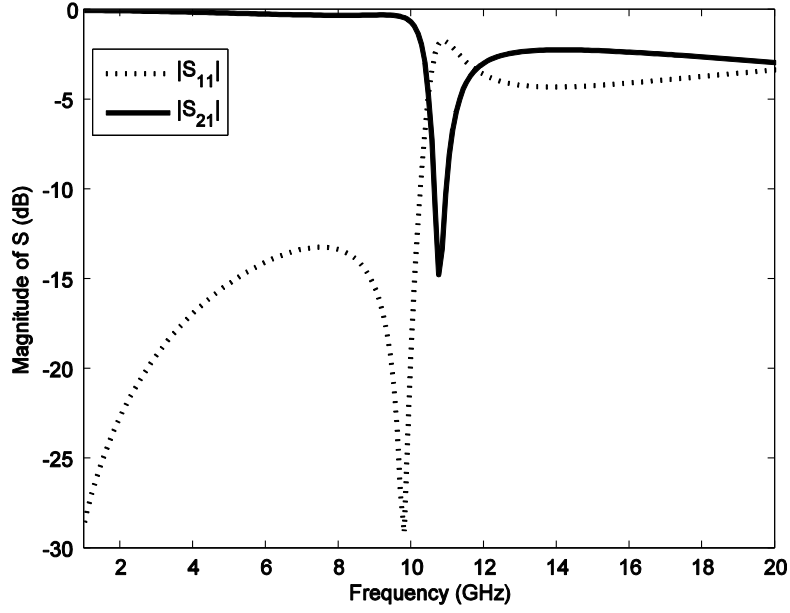


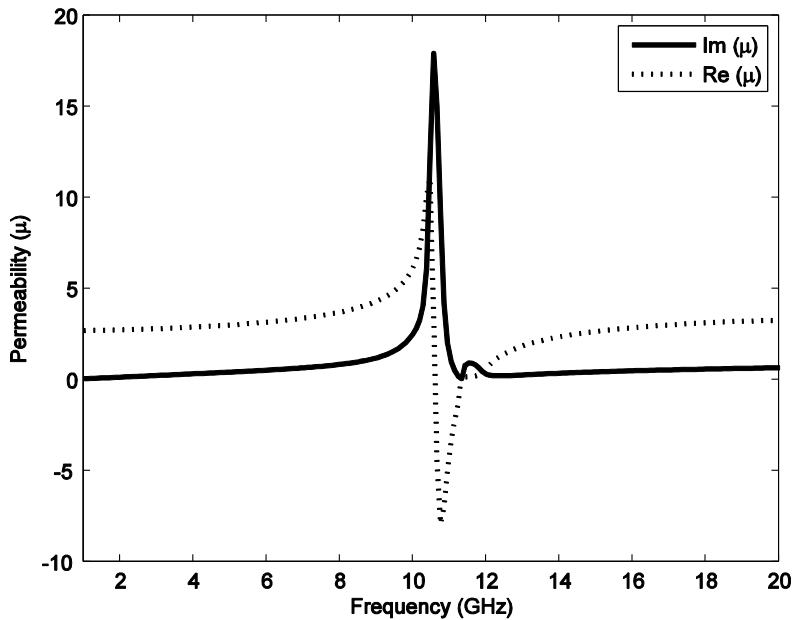
Figure 47. Simulated transmission characteristics,  $S_{11}$  and  $S_{21}$ , for the SRR.

Mathematically, the refractive index  $n$  and the impedance  $z$  of a homogeneous material is given by as,

$$n = \frac{1}{kd} \cos^{-1} \left\{ \frac{1}{2S_{21}} (1 - S_{11}^2 + S_{21}^2) \right\} \quad (43)$$

$$z = \sqrt{\frac{(1 + S_{11})^2 - S_{21}^2}{(1 - S_{11})^2 - S_{21}^2}} \quad (44)$$

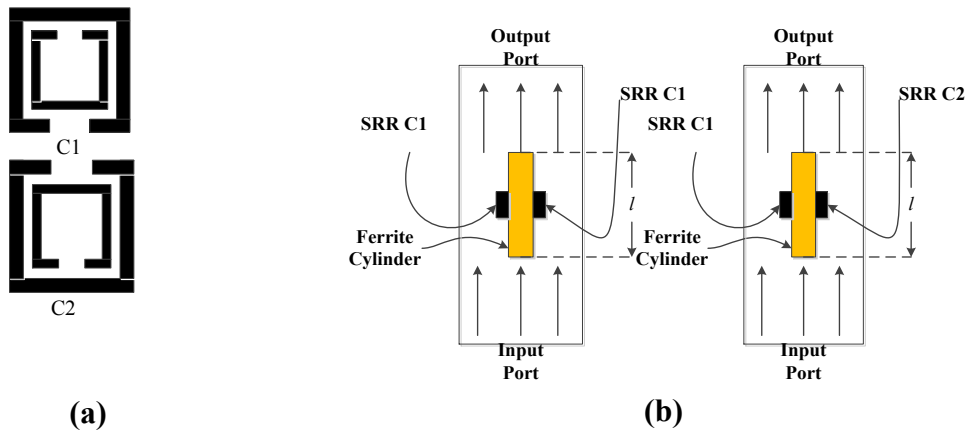
The permittivity and the permeability of the structure can be derived from (43) and (44) by substituting in  $\varepsilon = \frac{n}{z}$  and  $\mu = nz$ . For the designed dual SRR structure of Fig. 46, the permeability is calculated using the simulated  $S$ -parameter values shown in Fig. 47. A view of the calculated  $\mu$ , plotted in Fig. 48, shows that the designed structure starts to resonate at 10GHz as indicated by a sudden variation in  $\mu$ .



**Figure 48. Simulated permeability for the SRR unit-cell over a frequency sweep.**

As explained earlier in Chapter 3, superstrate based beam scan of a single 10GHz patch antenna (MPA) is achieved by introducing phase taper of the dominant component (y-component in this case) of the radiated E-field. By properly integrating SRR structure on the ferrite rods, the magnetic field induced in the SRR are made to constructively couple with the gyromagnetic properties of the magnetized ferrite. Thus, compared to normal ferrite rods, the SRR integrated ferrite rods can introduce same phase control for lesser magnetization ( $H_0$ ) requirements. On the other hand, for a certain external biasing field ( $H_0$ ), a much shorter SRR-integrated-ferrite-rod can demonstrate the same phase control as that of a longer ferrite-rod. In this research work, SRR-integrated ferrite rods are used to reduce the biasing requirements of the 10 GHz MPA to achieve beam scan. In addition, the SRR embedded FPC antenna requires a much smaller cavity height to produce same affects.

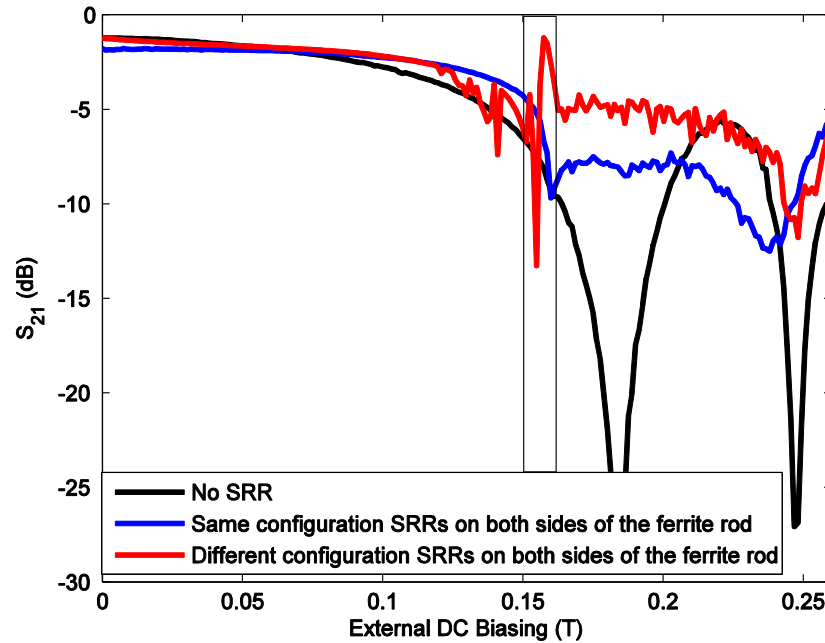
Proper integration of the SRR with the ferrite rod is essential to achieve constructive coupling of both resonances. Two different orientations (C1 and C2) of the SRR structures (of Fig. 46) are simulated. The HFSS simulation models uses plane waves to excite the SRR structures and observe the phase variation of the transmitted signal as a function of the magnetizing biasing of ferrite. Case 1 is when two SRRs, of the same configuration (C1), are placed on different sides of the ferrite rod. Case 2 is when two SRRs of different configuration (C1 & C2) are placed on either side of the ferrite rod. A schematic diagram of the SRR's, the simulation setup and the phase plots is given in Fig. 49.



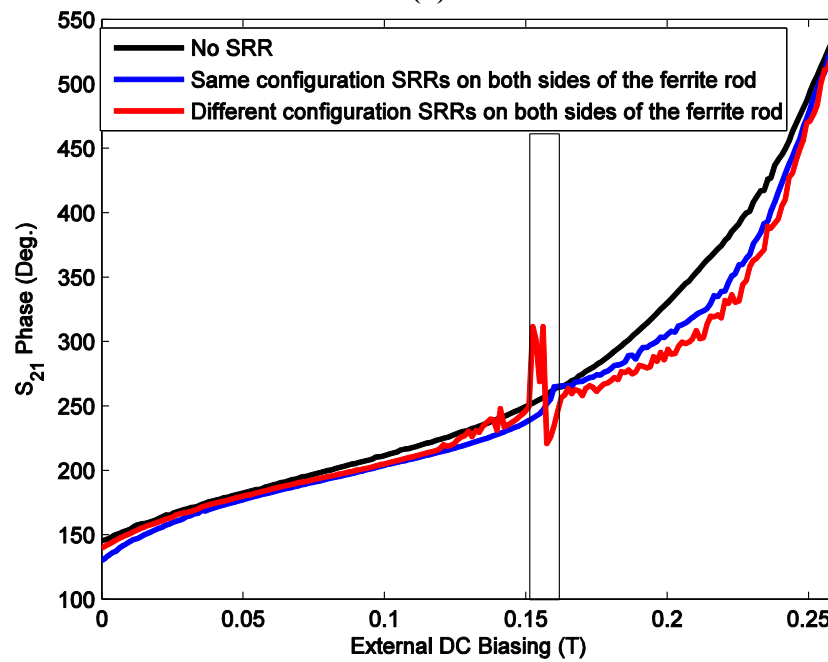
**Figure 49. Simulation setup for SRR integrated ferrite rods excited by plane waves (a) SRR configurations, C1 and C2, and (b) Two simulations scenarios; senario 1 – same SRR configuration C1 on both sides of the ferrite rod, senario 2 – different SRR combinations on both sides.**

Fig. 50 shows the simulated magnitude and phase response of the transmitted signal. It can be observed from Fig. 50 (a,b) that integration of the SRR configurations on the ferrite rod causes a second resonance like behavior between the biasing fields of 0.1511T and 0.1624T. This second resonance like behavior occurs well below the natural resonance of ferrite (0.26T) and causes a sudden variation in the phase of the transmitted signal as observed from Fig. 50 (b). The phase change is more severe for Case 2 (red curve in Fig. 50), where a small change in the biasing field causes up to  $150^\circ$  of change in the phase of

the transmitted signal. Hence by using this second resonance region of the SRR integrated ferrite structure, a phase taper of the radiated signal could be produced at much lesser biasing values as compared to the results of Chapter 4.



(a)



(b)

Figure 50. Simulated transmission characteristics for the different SRR configurations (a) magnitude, and (b) phase.

## 6.3 Single MPA with SRR Integrated Ferrite Superstrate

In this section, the ferrite loaded microstrip patch antenna (MPA) is modified to integrate SRRs with the ferrite rods. Fig. 51 shows the two different integrating methods of SRR's in the magnetized ferrite loading or superstrate. Case 1 has one SRR per side of the ferrite rod and case 2 has 2 SRRs of the same configuration on each side of the ferrite rod. These two cases are selected as they provide the best coupling between the SRR induces magnetic fields and the gyromagnetic properties of the axially biased ferrite rods.

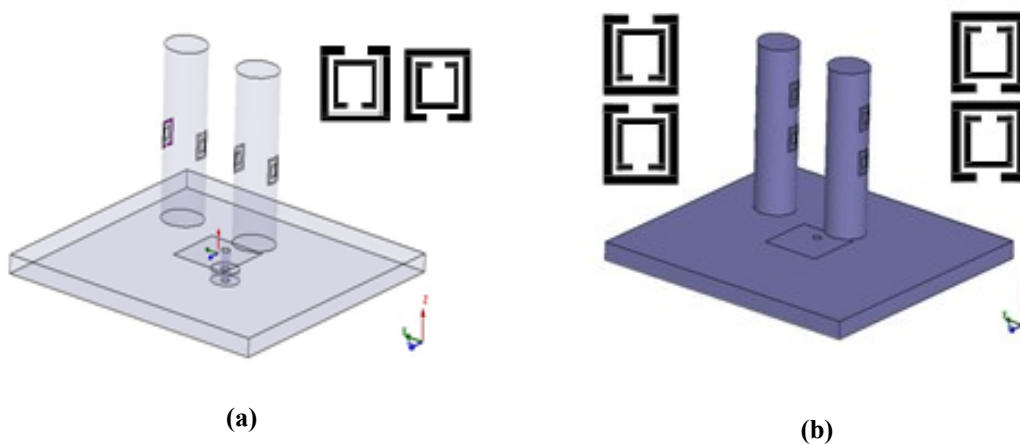


**Figure 51. HFSS simulation models for 10 GHz MPA with superstrate comprising of two ferrite rods with integrated SRRs at  $h = 2\text{mm}$  (a) case 1 - single SRR per side, and (b) case 2 - two SRRs per side of each ferrite rod.**

Similar to the discussion of Chapter 4, by changing the biasing values  $H_{01}$  and  $H_{02}$  separately, the main beam of the antenna starts to scan. For the SRR integrated MPA shown in Fig 51(a,b), the beam scan is tabulated in Table 5, where one ferrite rod is unbiased ( $H_{01}=0$ ) and the axial (+z-axis) biasing of the other ferrite rod is varied ( $H_{02}$  varied).

**Table 5. Maximum directivity and beam scan for H01 = 0 variable H02.**

<b>H02 (T)</b>	<b>Max. Directivity (dB) Case 1</b>	<b>Direction of Maximum (Deg.) Case 1</b>	<b>Max. Directivity (dB) Case 2</b>	<b>Direction of Maximum (Deg.) Case 2</b>
0	9.154	90	9.006	90
0.0315	7.012	87	8.156	90
0.0566	8.203	87	6.771	84
0.0629	8.370	88	6.685	78
0.0655	8.429	87	6.744	76
0.0679	8.483	87	6.843	74
0.0705	8.531	89	6.971	73
0.0730	8.574	90	7.112	72
0.0755	8.614	90	7.259	71
0.0780	8.645	90	7.403	71
0.0806	8.682	90	7.538	71
0.0831	8.411	92	7.663	70
0.0944	8.256	93	8.036	71
0.1259	7.933	97	8.060	91
0.1322	7.781	98	8.259	97
0.1385	7.698	99	8.486	110
0.1448	7.474	100	8.662	103
0.1511	7.272	103	8.928	104
0.1574	7.102	107	8.164	101

Note that in case 1 of Table 5, as the DC magnetizing field in +z-axis increases up to 0.0730T, the main beam remains close to the original broadside direction with maximum at 90°. However, when the biasing is varied between 0.0831T and 0.1574T a smooth beam scan of up to 17°, in the +x-direction is observed. This beam scan is due to the sudden phase variation of the transmitted signal seen in Fig. 50(red curve) due to constructive coupling of the SRR contributed fields and the pressings magnetic moments of ferrite. On the contrary, tabulated beam scan for case 2 is observed at much lower biasing; 0T to 0.0831T. Thus, for a differential magnetic biasing of  $\Delta H_0 = 0.0831\text{T}$ , the main beam scan of -20° is observed in the -x-direction. A further increase in the H02 biasing results in a beam scan in the +x-direction, similar to that of case 1. A comparison of the directivity values shows that case 1 provides higher directivity values at lower biasing as compared to case 2. This

is due to more constructive coupling of two SRR generated fields compared to one, which increases the phase control behavior at the cost of increased absorption. Thus, as the number of SRRs is increased in case 2, more of the RF signal gets absorbed leading to lesser directivity as compared to case 1 or no SRR case presented in Chapter 4. Although the results presented are for H01 unbiased, similar directivity but opposite directional (+x-axis) beam scan of the MPA is observed, when H01 is axially biased in +z-axis and H02 is kept unbiased. The simulated reflection response for both the cases are plotted in Fig. 52. Note that addition of SRRs have little effect on the center frequency of the antenna.

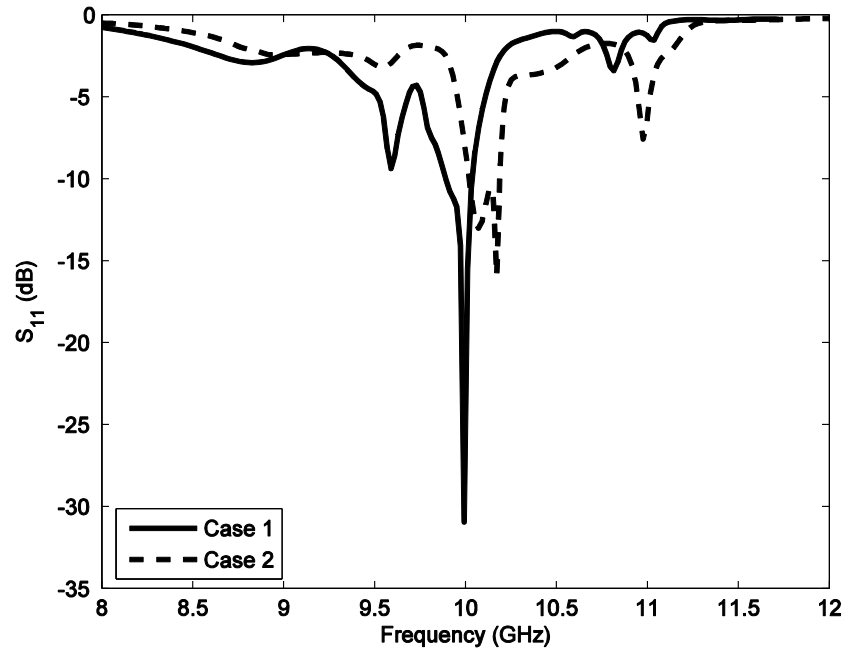


**Figure 52. Simulated S11 response for both cases of the MPA with SRR integrated ferrite rods.**

The simulated 2-D radiation patterns for the antennas shown in Fig 51 (a,b) are plotted in Fig. 53 and Fig. 54, respectively. The beam scan in both directions (+x and -x) are achieved by individually magnetizing (H01 or H02) the two ferrite rods. Thus, a HPBW of 62.3° is observed for the MPA loaded with SRR integrated ferrite rod as superstrates. Compared to the directivity patterns of Chapter 4, both the simulated cases provide a much

clearer beam scan with obvious main beam direction changes. This class of beam scannable microstrip patch antenna (MPA) with wide HPBWs ( $\cong 50^\circ$ ) can be used for sector based indoor coverage.

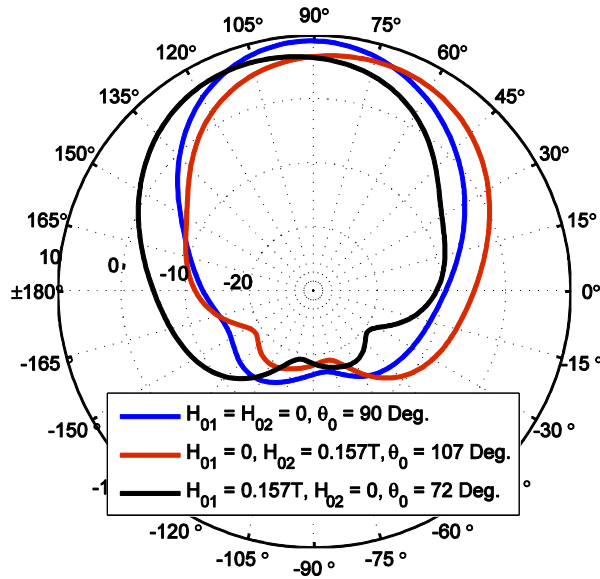


Figure 53. Simulated 2-D directivity patterns for the E-plane for maximum beam scan for case 1 – one SRR per side of the ferrite rod, and (b) case 2 – two SRRs per each side of the ferrite rod.

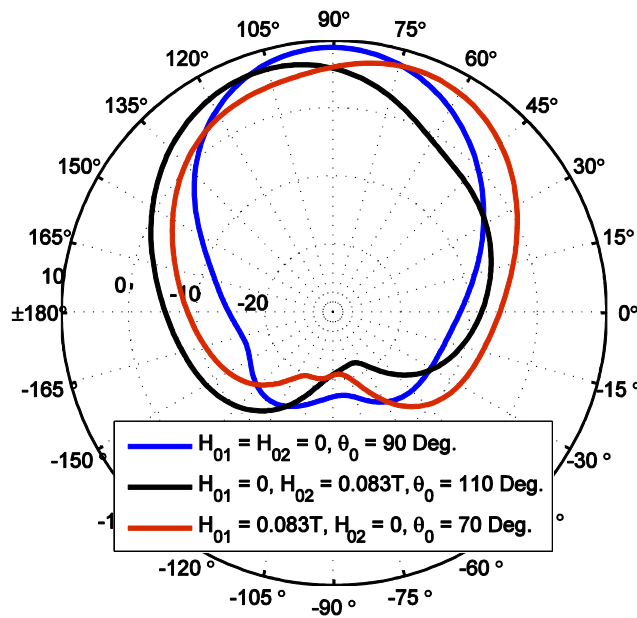
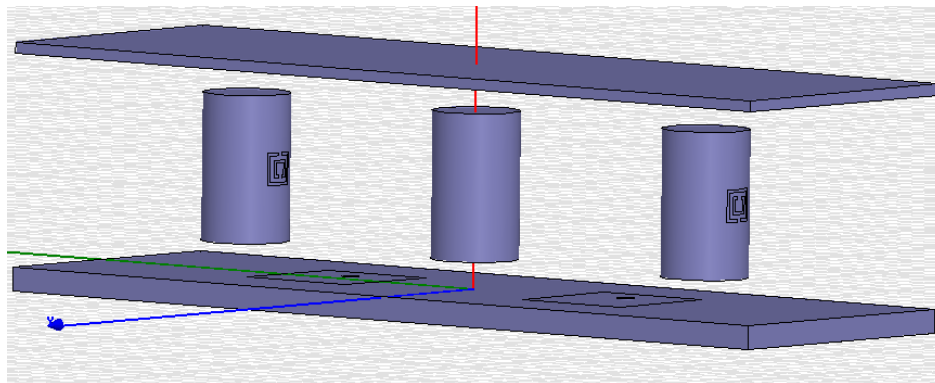


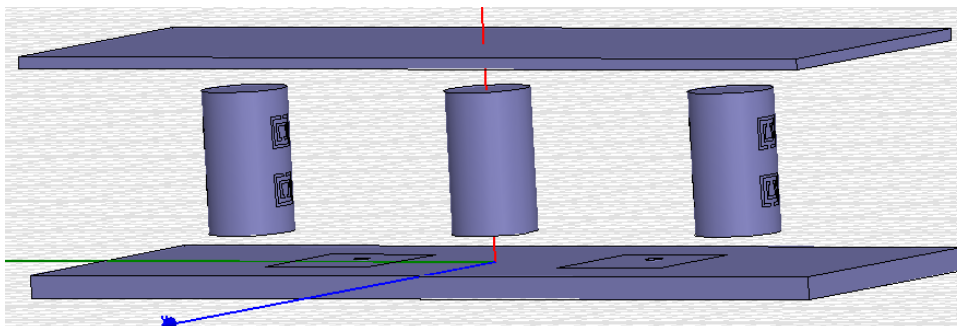
Figure 54. Simulated E-plane directivity patterns for maximum beam scan for case 2 – two SRRs per each side of the ferrite rod.

## 6.4 Ferrite Loaded FPC Antenna Array with Integrated SRRs

As observed from the results presented in Section 6.3, integrating SRRs on the ferrite rods, results in similar beam scans at much lower biasing fields. In order to extend this idea to a 2-patch FPC antenna array designed in Section 5.2, both configurations of SRR have been integrated on the ferrite rods and simulations have been performed to observe the beam scan of the resulting structure. Fig. 55 shows the HFSS simulation models for both the SRR configurations integrated on the 2-patch FPC.



(a)



(b)

Figure 55. HFSS simulation models for the 2-patch FPC with SRR integrated ferrite superstrate, (a) Case 1- single SRR on each side, and (b) Case 2 – two SRRs on each side of both ferrite rods.

A differential variation in the applied magnetizing fields, H01 and H02, results in a beam scan of the FPC antenna array. Table 6 summarizes the beam scan and directivity responses for both the integrated SRR configurations of Fig. 55.

**Table 6. Beam scan and maximum directivity values for the 2-Patch FPC antenna with integrated ferrite superstrate with varying H02 and H01=0T .**

<b>H02 (T)</b>	<b>Max. Directivity (dB) Case 1</b>	<b>Direction of Maximum (Deg.) Case 1</b>	<b>Max. Directivity (dB) Case 2</b>	<b>Direction of Maximum (Deg.) Case 2</b>
0	8.381	90	8.220	90
0.0315	8.367	92	8.318	92
0.0566	8.475	93	8.339	96
0.0629	8.644	96	8.286	99
0.0655	8.537	97	8.208	103
0.0679	8.623	99	8.245	107
0.0705	8.579	100	8.329	113
0.0730	8.663	103	8.331	109
0.0755	8.591	105	8.298	109
0.0780	8.688	110	8.248	108

Comparing the results of Table 6 with the FPC array without the integrated SRR presented in Section 5.2, it is observed that the integration of the SRRs produces beam scan at much lower biasing values. Without the SRRs a maximum simulated beam scan of  $\pm 12^\circ$  for a biasing field of 0.22T (200 kA/m) was shown in Section 5.2. Both configurations of the SRRs integrated with magnetized ferrite provide higher beam scans of  $\pm 20^\circ$  and  $\pm 23^\circ$  for magnetizing fields of 0.078T (62 kA/m) and 0.0705T (56 kA/m) for case 1 and case 2 respectively. As observed from the directivity values from Table 6, integration of the SRRs on the ferrite rods results in directivity values of 8.381 dB and 8.22 dB for the two respective cases, as compared to 8.53 dB without the SRRs. Due to the RF signal current appearing across the SRRs integrated on the ferrite rods, the efficiency of the new designs also decreases to 75.61% and 72.05% for the two respective cases of Fig. 55. A view of the simulated 2-D radiation patterns for maximum beams scans is provided in Fig. 56 and 57.

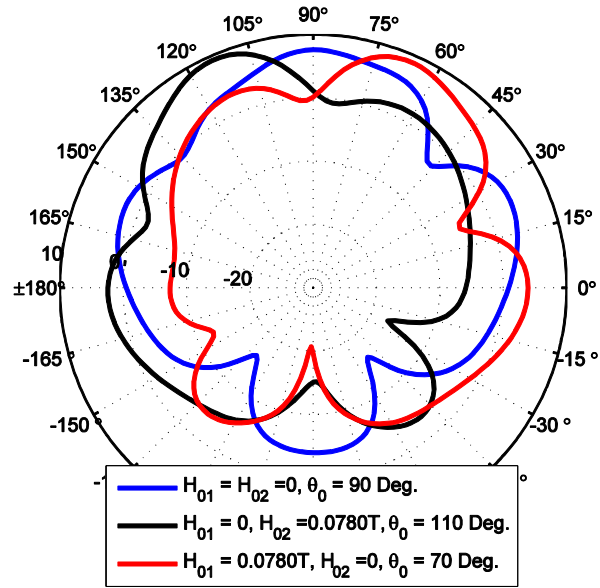


Figure 56. Simulated 2-D radiation patterns for FPC with SRR integrated ferrite rods (case 1) for no beam scan and maximum beam scan conditions.

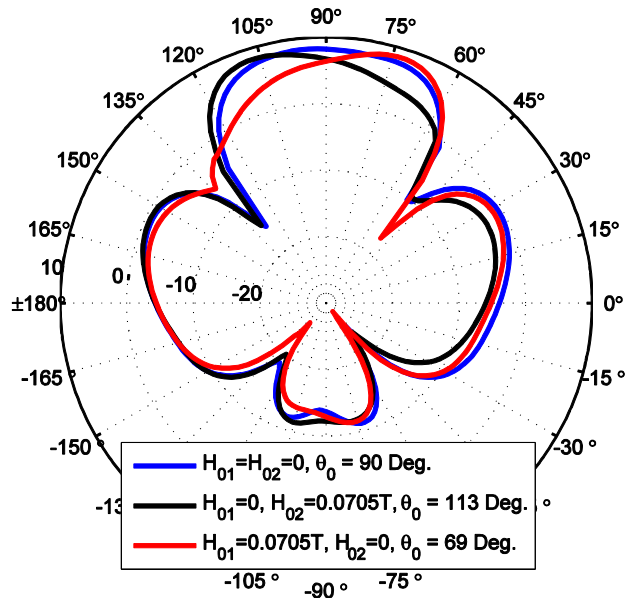


Figure 57. Simulated 2-D radiation patterns for FPC with SRR integrated ferrite rods (case 2) for no beam scan and maximum beam scan conditions.

## 6.5 Performance Comparison

Through Chapter 5 and Chapter 6, two different ferrite superstrate designs to achieve beam scans have been presented. A comparison of the performance characteristics of these designs is provided in Table 7.

**Table 7. Performance comparison of the different FPC antenna configurations with dielectric-ferrite superstrate and excited by 2x1 patch .**

<b>Antenna Design</b>	<b>HPBW (°)</b>	<b>Max. Beam Scan (°)</b>	<b>Biasing Required for Max. Beam Scan (T)</b>	<b>For a given coil, DC Current required for Magnetic Biasing (A)</b>	<b>Resonant Frequency (GHz)</b>
FPC with Ferrite	37	± 12	0.22	1.83	10.2
FPC with SRR integrated ferrite, Case 1	39.6	± 20	0.078	0.65	9.93
FPC – SRR integrated ferrite, Case 2	37.8	± 23	0.070	0.58	10.1

It is evident that the addition of SRRs on the ferrite rods decreases the biasing fields required for beam scan. A decrease in the biasing fields directly corresponds to a decrease in the current required to produce that field. In moving from no SRRs to the Case 2 of integrated SRRs, a decrease of 1.25 A in the current requirement is observed. Additionally, a higher beam scan of up to  $\pm 23^\circ$  is observed as a result of SRR integration on to the ferrite rods. The HPBW and the resonant frequencies remain almost constant regardless of the biasing values.

## 6.6 Conclusion

This chapter described the beam scanning properties of a microstrip patch antenna and the 2-patch FPC antenna, loaded with SRR integrated ferrite rods as superstrate. This ferrite based metamaterial superstrate introduced controlled phase delay to produce the tapered  $E_y$ -component of the radiated signal. This resulted in scanning the main beam of the antenna depending on the externally applied axial biasing field. Two different designs with one or two SRR integrated ferrite rods are simulated and the optimized results provided a beam scan of  $\pm 17^\circ$  and  $\pm 20^\circ$ , respectively for the single patch antenna. As the number of SRRs is increased (case 2), a larger beam scan at a much lower biasing (0.0831T) is achieved at the cost of a slightly lowered directivity (0.748dB) of the antenna. Loading FPC antenna with SRR integrated ferrite rods produced higher degrees of beam scan,  $\pm 20^\circ$  and  $\pm 23^\circ$ , for the two cases of SRR configurations. The biasing requirements for the 2-patch FPC are significantly reduced to 0.078T (62 kA/m) and 0.0705T (56 kA/m) for the two SRR configurations, respectively. Integrating SRRs on the magnetized ferrite rods resulted in a beam scan at a considerably lower biasing values. This can reduce the size of the electro-magnet/biasing coils, needed for generating the external biasing field ( $H_0$ ). In addition, integrating more SRRs or using LTCC technology allows the biasing coils to be embedded within the ferrite rods [61] to further reduce the biasing complexity and antenna dimension.

## CHAPTER 7

# CONCLUSION

### 7.1 Contribution

The main contribution of this work is the design and analysis of a SRR integrated ferrite loaded Fabry-Perot Cavity (FPC) antenna with improved beam scanning property. Initially the FPC is optimally excited with a 2x1 thinned microstrip array with large patch separation distance. The multilayer superstrate (top layer) of the cavity is made of a tapered dielectric layer and a foam-ferrite layer. The foam-ferrite layer consists of three axially magnetized ferrite rods, centrally positioned above the non-radiating edge of the patches. This layer introduces the externally controllable phase delay to the dominant  $E_y$ -component of the radiated field, which results in scanning the main beam of the FPC. The tapered dielectric layer of the superstrate improves the main lobe to side lobe ratio of the radiation pattern. Compared to traditional phase array technique, the proposed superstrate based beam scanning of an FPC is important, as it can scan the main beam with minimal effect to the side-lobe level.

Before designing the FPC, knowledge on the interaction of the propagating microwave signal and the magnetic moments within the ferrite material is essential. The characteristic equations of a ferrite-rod with magnetic side wall boundaries are plotted to determine the propagating modes. For a fixed frequency of operation (10 GHz), the mode charts allowed the determination of the low-loss operating regions that provides necessary phase control with small changes of external magnetizing field ( $H_0$ ). In addition, the field-frequency mode chart highlighted the lossy resonance regions of ferrites. Professional simulator (HFSS) is used to model scattering parameters of an axially magnetized ferrite load. Comparing the mode charts calculated using analytical technique and professional simulator, the HFSS simulation model of the ferrite rod is verified. The simulated transmission response demonstrated that a 0.052T change in the magnetizing field produced an output phase change of  $57^\circ$  with an insertion loss of 0.03 dB.

A microstrip patch antenna (MPA) loaded with axially magnetized ferrite rods (as superstrate) is initially investigated as proof of concept. The ferrite rods are positioned above the center of the non-radiating edges of MPA to interact with the magnetic field components of the radiated waves. Biasing any one of the ferrite cylinders resulted in a phase taper of the radiated E-field, hence, causing beam scan. A comprehensive parametric study concluded the exact dimensions and the placement to ensure maximum directivity and beam scan. Two ferrite rods are individually axially magnetized with  $H_{01}$  and  $H_{02}$  and by varying  $H_{01}$  with  $H_{02}=0$  provided a beam scan of  $+30^\circ$  for  $\Delta H_{01}=0.22$  Tesla. Similarly, by varying  $H_{02}$  with  $H_{01}=0$  provided a beam scan of  $-30^\circ$  for  $\Delta H_{02}=0.22$  Tesla. The loss in broadside directivity due to the presence of biasing coil and the ferrite rods is observed to be 0.25 dB. The fabricated antenna structure validated the simulated results by

demonstrating a maximum beam scans of  $+28^\circ$  and  $-26^\circ$  degrees for biasing values of  $\Delta H_{01} = 0.19\text{T}$  and  $\Delta H_{02} = 0.19\text{T}$ , respectively. To improve the directivity of this ferrite loaded microstrip patch antenna, a dielectric component of the superstrate is added. Since the cavity between the multilayer superstrate (foam-ferrite layer and dielectric layer) and the MPA has little influence in the antenna behavior, the designed antenna is called FPC antenna. This design demonstrated improved directivity at the cost of distinctive beam scanning properties.

To further improve the antenna responses, an FPC antenna is designed with multilayer superstrate consisting of tapered dielectric layer and foam-ferrite layer. The cavity formed between the antenna ground and superstrate is optimally excited with a thinned  $2 \times 1$  array of microstrip patches. Professional simulator (HFSS) is used to optimize the tapered dielectric layer of the superstrate to minimize the side-lobe level of the radiated wave. Air-ferrite layer of the superstrate is optimized to produce beam scan by introducing the required phase taper of the radiated  $E_y$  field distribution. This required the ferrite rods to be individually biased and positioned above the center of the patches non-radiating edges. The two ferrite rods are individually axially magnetized with  $H_{01}$  and  $H_{02}$ . It is by  $H_{01}$ , with  $H_{02}=0$  that a beam scan of  $+12^\circ$  for  $\Delta H_{01}=0.22$  Tesla is achieved. Similarly, by varying  $H_{02}$  with  $H_{01}=0$ , a beam scan of  $-12^\circ$  for  $\Delta H_{02}=0.22$  Tesla is achieved. The loss in broadside directivity due to the presence of biasing coil and the ferrite rods is observed to be 0.25 dB. The fabricated antenna structure validated the simulated results by demonstrating a maximum beam scans of  $+14^\circ$  and  $-12^\circ$  degrees for biasing values of  $\Delta H_{01} = 0.19\text{T}$  and  $\Delta H_{02} = 0.19\text{T}$ , respectively.

To reduce the size of the biasing coils, ferrite based metamaterial superstrate is proposed. This consisted of magnetized ferrite rods with optimally integrated split ring resonators (SRRs). When the MPA is loaded with modified foam-ferrite (SRR integrated) superstrate, the simulated results demonstrated an 86.6% decrease in the antenna height. The designed antenna also demonstrated a beam scan of  $\pm 17^\circ$  for biasing field of  $\Delta H = 0.1574\text{T}$  and  $\pm 20^\circ$  for  $\Delta H = 0.083\text{T}$ , respectively for one and two integrated SRR elements. Similarly, for an FPC antenna with modified SRR integrated foam-ferrites superstrate and excited by a thinned 2x1 microstrip patch array, a beam scan of  $\pm 20^\circ$  and  $\pm 23^\circ$  for  $\Delta H = 0.078\text{T}$  and  $\Delta H = 0.0708\text{T}$ , respectively is observed. Since embedding SRRs on the magnetized ferrite rods resulted in a beam scan at considerably lower biasing values, this can be used to reduce the size of the electro-magnet and related biasing current requirements. In addition, integrating more SRRs or the use of low temperature co-fired ceramic (LTCC) technology to embed the biasing coils within the ferrite rods can further reduce the biasing complexity and antenna dimension.

## 7.2 Future Work

Although the proposed idea has been shown to work, the design can be improved further. The following list provides some of the ideas to improving the presented work.

- 1- Recently LTCCs have been used to provide embedded biasing coils inside substrates. Use of LTCC technology with the ferrite superstrate would enable biasing without using externally wound coils, resulting in a simple design. KAUST has the facilities to embed LTCC coils inside ferrite material. This approach,

however, would require a redesign of the superstrate since not all ferrite materials can be embedded with coils.

- 2- Due to the limited conformal SRR fabrication facilities, the SRR integrated ferrite superstrate has not been successfully fabricated. The LTCC embedded ferrite with metamaterial unit-cells would result in small and highly practical superstrates that can be used easily without any external biasing setup.

# APPENDIX

## A. Derivation of Equation of Motion

The vector representation of the torque acting on a spinning electron is given by,

$$\mathbf{T} = \mu_o \mathbf{m} \times \mathbf{H}_o \quad (\text{A-1})$$

The spin angular momentum of a spinning electron,  $\mathbf{S}$ , is given by,

$$\mathbf{S} = \frac{\hbar}{2} \quad (\text{A-2})$$

Where  $\hbar$  is the reduced Plank's constant with a numerical value,  $\hbar = 1.054 \times 10^{-34}$  J.s.

The magnetic moment,  $\mathbf{m}$ , and the spin angular momentum,  $\mathbf{S}$ , are related through a constant  $\gamma$  as,

$$\mathbf{m} = -\gamma \mathbf{S} \quad (\text{A-3})$$

The negative sign shows that the angular momentum is in opposite direction to that of the magnetic moment. Rewriting (A-1) in terms of  $\mathbf{S}$ ,

$$\mathbf{T} = -\mu_o \gamma \mathbf{S} \times \mathbf{H}_o \quad (\text{A-4})$$

$$\frac{d\mathbf{m}}{dt} = -\mu_o \gamma \mathbf{m} \times \mathbf{H}_o \quad (\text{A-5})$$

For (A-5), the fact that torque is the rate of change of angular momentum

$\left(\mathbf{T} = \frac{d\mathbf{S}}{dt} = -\frac{1}{\gamma} \frac{d\mathbf{m}}{dt}\right)$  has been used. Using Cartesian coordinate system and with the supposition that the applied DC magnetic bias,  $\mathbf{H}_o$ , is directed along the z-axis,  $\mathbf{m}$  and  $\mathbf{H}_o$  can be written in terms of the components as,

$$\mathbf{m} = m_x \hat{\mathbf{x}} + m_y \hat{\mathbf{y}} + m_z \hat{\mathbf{z}} \quad (\text{A-6})$$

$$\mathbf{H}_o = H_o \hat{\mathbf{z}} \quad (\text{A-7})$$

Substituting (A-6) and (A-7) into (A-5), we get,

$$\frac{d\mathbf{m}}{dt} = -\mu_o \gamma (m_x \hat{\mathbf{x}} + m_y \hat{\mathbf{y}} + m_z \hat{\mathbf{z}}) \times H_o \hat{\mathbf{z}} \quad (\text{A-8})$$

$$\xrightarrow{(\text{A-8})} \frac{d\mathbf{m}}{dt} = -\mu_o \gamma (-m_x H_o \hat{\mathbf{y}} + m_y H_o \hat{\mathbf{x}}) \quad (\text{A-9})$$

$$\frac{dm_x}{dt} = -\mu_o \gamma m_y H_o$$

$$\frac{dm_y}{dt} = \mu_o \gamma m_x H_o \quad (\text{A-10})$$

$$\frac{dm_z}{dt} = 0$$

Taking the time derivative of the equation set (A-10), we get

$$\frac{d^2 m_x}{dt^2} = -\mu_o \gamma H_o \frac{dm_y}{dt}$$

$$\frac{d^2 m_y}{dt^2} = \mu_o \gamma H_o \frac{dm_x}{dt} \quad (\text{A-11})$$

$$\frac{dm_z}{dt} = 0$$

Substituting the respective values of  $\frac{dm_x}{dt}$  and  $\frac{dm_y}{dt}$  from (A-10) into (A-11) and for the sake of simplicity  $\omega_o = \mu_o \gamma H_o$ , (A-11) gives us the following set of second order homogeneous differential equations,

$$\frac{d^2 m_x}{dt^2} + \omega_o^2 m_x = 0$$

$$\frac{d^2 m_y}{dt^2} + \omega_o^2 m_y = 0 \quad (\text{A-12})$$

## B. Derivation of Polder Permeability Matrix

Proceeding with (26) from Section 3.3,

$$\frac{d\mathbf{M}}{dt} = -\mu_o\gamma(M_0\hat{\mathbf{z}} + \mathbf{m}) \times (H_0\hat{\mathbf{z}} + \mathbf{h}) \quad (\text{B-1})$$

$$\begin{aligned} \frac{d\mathbf{M}}{dt} = & -\mu_o\gamma\{\hat{\mathbf{x}}(M_yH_0 - H_yM_0 + M_yH_z - M_zH_y) \\ & - \hat{\mathbf{y}}(M_xH_0 - H_xM_0 + M_xH_z - M_zH_x) + \hat{\mathbf{z}}(M_xH_y - M_yH_x)\} \end{aligned} \quad (\text{B-2})$$

Ignoring the AC-field product terms (B-2) can be simplified as,

$$\begin{aligned} \frac{d\mathbf{M}}{dt} = & -\mu_o\gamma\{\hat{\mathbf{x}}(M_yH_0 - H_yM_0) - \hat{\mathbf{y}}(M_xH_0 - H_xM_0)\} \\ \xrightarrow{\text{yields}} & \frac{dM_x}{dt} = -\mu_o\gamma M_y H_0 + \mu_o\gamma H_y M_0 \end{aligned} \quad (\text{B-3})$$

$$\frac{dM_y}{dt} = \mu_o\gamma M_x H_0 - \mu_o\gamma H_x M_0 \quad (\text{B-4})$$

Substituting  $\omega_0 = \mu_o\gamma H_0$  and  $\omega_m = \mu_o\gamma M_0$  in (B-3) and (B-4),

$$\frac{dM_x}{dt} = -\omega_0 M_y + \omega_m H_y \quad (\text{B-5})$$

$$\frac{dM_y}{dt} = \omega_0 M_x - \omega_m H_x \quad (\text{B-6})$$

For time varying fields, (B-5) and (B-6) can be transformed as,

$$j\omega M_x = -\omega_0 M_y + \omega_m H_y \quad (\text{B-7})$$

$$j\omega M_y = \omega_0 M_x - \omega_m H_x \quad (\text{B-8})$$

$$j\omega M_z = 0$$

$$\xrightarrow{(\text{B-8})} M_y = \frac{\omega_0 M_x}{j\omega} - \frac{\omega_m H_x}{j\omega} \quad (\text{B-9})$$

Substituting (B-9) into (B-7) and simplifying,

$$M_x = \frac{\omega_0 \omega_m}{\omega_0^2 - \omega^2} H_x + j \frac{\omega \omega_m}{\omega_0^2 - \omega^2} H_y \quad (\text{B-10})$$

Similarly,

$$M_y = -j \frac{\omega \omega_m}{\omega_0^2 - \omega^2} H_x + \frac{\omega_0 \omega_m}{\omega_0^2 - \omega^2} H_y \quad (\text{B-11})$$

The rest of the derivation proceeds from (30) Section 3.3 onwards.

## C. Characteristic Equation Derivation for Magnetized Ferrite Rod

Ferrite is a naturally occurring anisotropic material having a tensor magnetic permeability which is a function of the applied magnetic bias. For an axially magnetized ferrite cylinder in the  $z$ -direction, the tensor permeability is given by (1).

$$\mu_r = \begin{bmatrix} \mu & -j\kappa & 0 \\ j\kappa & \mu & 0 \\ 0 & 0 & \mu_z \end{bmatrix} \quad (1)$$

where

$$\mu = 1 + \frac{\omega_0 \omega_m}{\omega_0^2 - \omega^2}$$

$$\kappa = -\frac{\omega_m \omega}{\omega_0^2 - \omega^2}$$

and  $\omega = 2\pi f$ ,  $\omega_0 = 2\pi \gamma H$  and  $\omega_m = 2\pi \gamma M$ .  $f$  is the frequency of operation,  $H$  is the applied DC biasing value in kA/m and  $M$  is the saturation magnetization of the specific ferrite (kA/m).

Using the Shul, Walke and Kales method, the field vectors can be split-up into transverse and longitudinal components. For a plane wave travelling in the +z direction, the equations can be written as (A).

$$\begin{aligned}
 \mathbf{E} &= (\mathbf{E}_t + E_z \hat{\mathbf{z}}) e^{-j\beta z} \\
 \mathbf{H} &= (\mathbf{H}_t + H_z \hat{\mathbf{z}}) e^{-j\beta z} \\
 \mathbf{B} &= (\mathbf{B}_t + B_z \hat{\mathbf{z}}) e^{-j\beta z} \\
 &= \mu \mathbf{H}_t + j\kappa(\hat{\mathbf{z}} \times \mathbf{H}_t) + \mu_z H_z \hat{\mathbf{z}} \\
 \nabla &= \nabla_t - j\beta \hat{\mathbf{z}}
 \end{aligned} \tag{A}$$

Considering the basic Maxwell's equations (2) and (3)

$$\nabla \times \mathbf{E} = -j\omega\mu_0\mu_r \mathbf{H} \tag{2}$$

$$\nabla \times \mathbf{H} = j\omega\varepsilon_0\varepsilon_r \mathbf{E} \tag{3}$$

Substituting (A) into (2) we get,

$$\begin{aligned}
 (\nabla_t - j\beta \hat{\mathbf{z}}) \times (\mathbf{E}_t + E_z \hat{\mathbf{z}}) e^{-j\beta z} &= -j\omega\mu_0\{\mu_r\}(\mathbf{H}_t + H_z \hat{\mathbf{z}}) e^{-j\beta z} \\
 (\nabla_t \times \mathbf{E}_t) - j\beta(\hat{\mathbf{z}} \times \mathbf{E}_t) + (\nabla_t \times E_z \hat{\mathbf{z}}) &= -j\omega\mu_0 \mathbf{B} \\
 (\nabla_t \times \mathbf{E}_t) - j\beta(\hat{\mathbf{z}} \times \mathbf{E}_t) + (\nabla_t \times E_z \hat{\mathbf{z}}) &= -j\omega\mu_0\{\mu \mathbf{H}_t + j\kappa(\hat{\mathbf{z}} \times \mathbf{H}_t) + \mu_z H_z \hat{\mathbf{z}}\}
 \end{aligned} \tag{4}$$

Separating the transverse and the longitudinal components

$$(\nabla_t \times \mathbf{E}_t) = -j\omega\mu_0\mu_z H_z \hat{\mathbf{z}} \tag{4.1}$$

$$-j\beta(\hat{\mathbf{z}} \times \mathbf{E}_t) + (\nabla_t \times E_z \hat{\mathbf{z}}) = -j\omega\mu_0\{\mu \mathbf{H}_t + j\kappa(\hat{\mathbf{z}} \times \mathbf{H}_t)\} \tag{4.2}$$

Substituting (A) into (3) we get

$$\begin{aligned}
 (\nabla_t - j\beta\hat{\mathbf{z}}) \times (\mathbf{H}_t + H_z\hat{\mathbf{z}}) e^{-j\beta z} &= j\omega\epsilon_0\{\epsilon_r(\mathbf{E}_t + E_z\hat{\mathbf{z}}) e^{-j\beta z}\} \\
 (\nabla_t \times \mathbf{H}_t) - j\beta(\hat{\mathbf{z}} \times \mathbf{H}_t) + (\nabla_t \times H_z\hat{\mathbf{z}}) &= j\omega\epsilon_0\epsilon_r(\mathbf{E}_t + E_z\hat{\mathbf{z}})
 \end{aligned} \tag{5}$$

Separating the transverse and the longitudinal components

$$(\nabla_t \times \mathbf{H}_t) = j\omega\epsilon_0\epsilon_r E_z \hat{\mathbf{z}} \tag{5.1}$$

$$-j\beta(\hat{\mathbf{z}} \times \mathbf{H}_t) + (\nabla_t \times H_z\hat{\mathbf{z}}) = j\omega\epsilon_0\epsilon_r \mathbf{E}_t \tag{5.2}$$

From the divergence equation

$$\nabla \cdot \mathbf{D} = 0$$

$$\nabla \cdot \epsilon \mathbf{E} = 0$$

Substituting respective relations from (A)

$$\begin{aligned}
 (\nabla_t - j\beta\hat{\mathbf{z}}) \cdot \epsilon(\mathbf{E}_t + E_z\hat{\mathbf{z}}) e^{-j\beta z} &= 0 \\
 \nabla_t \cdot \mathbf{E}_t + \nabla_t \cdot E_z\hat{\mathbf{z}} - j\beta(\hat{\mathbf{z}} \cdot \mathbf{E}_t) - j\beta E_z(\hat{\mathbf{z}} \cdot \hat{\mathbf{z}}) &= 0 \\
 \nabla_t \cdot \mathbf{E}_t - j\beta E_z &= 0
 \end{aligned} \tag{6}$$

Also

$$\nabla \cdot \mathbf{B} = 0$$

$$\nabla \cdot \epsilon \mathbf{E} = 0$$

Substituting respective relations from (A)

$$\mu(\nabla_t \cdot \mathbf{H}_t) + j\kappa\{\nabla_t \cdot (\hat{\mathbf{z}} \times \mathbf{H}_t)\} + \beta\kappa\{\hat{\mathbf{z}} \cdot (\hat{\mathbf{z}} \times \mathbf{H}_t)\} - j\beta\mu_z H_z = 0 \quad (7)$$

$$\mu(\nabla_t \cdot \mathbf{H}_t) + j\kappa\{\nabla_t \cdot (\hat{\mathbf{z}} \times \mathbf{H}_t)\} - j\beta\mu_z H_z = 0$$

Substituting  $\mathbf{E}_t$  from (5.2) into (4.2) we get

$$\begin{aligned} & -j\beta \left[ \hat{\mathbf{z}} \times \left\{ \frac{1}{j\omega\epsilon_0\epsilon_r} ((\nabla_t \times H_z \hat{\mathbf{z}}) - j\beta(\hat{\mathbf{z}} \times \mathbf{H}_t)) \right\} \right] + (\nabla_t \times E_z \hat{\mathbf{z}}) \\ & = -j\omega\mu_0\{\mu\mathbf{H}_t + j\kappa(\hat{\mathbf{z}} \times \mathbf{H}_t)\} \\ & \frac{-j\beta}{j\omega\epsilon_0\epsilon_r} [\hat{\mathbf{z}} \times ((\nabla_t \times H_z \hat{\mathbf{z}}) - j\beta(\hat{\mathbf{z}} \times \mathbf{H}_t))] + (\nabla_t \times E_z \hat{\mathbf{z}}) \\ & = -j\omega\mu_0\{\mu\mathbf{H}_t + j\kappa(\hat{\mathbf{z}} \times \mathbf{H}_t)\} \\ & \frac{-j\beta}{j\omega\epsilon_0\epsilon_r} [(\hat{\mathbf{z}} \times \nabla_t \times \hat{\mathbf{z}})H_z - j\beta(\hat{\mathbf{z}} \times \hat{\mathbf{z}} \times \mathbf{H}_t)] + (\nabla_t \times \hat{\mathbf{z}})E_z \\ & = -j\omega\mu_0\{\mu\mathbf{H}_t + j\kappa(\hat{\mathbf{z}} \times \mathbf{H}_t)\} \end{aligned} \quad (7.1)$$

Consider

$$\begin{aligned} \hat{\mathbf{z}} \times \hat{\mathbf{z}} \times \mathbf{H}_t &= \hat{\mathbf{z}}(\hat{\mathbf{z}} \cdot \mathbf{H}_t) - \mathbf{H}_t(\hat{\mathbf{z}} \cdot \hat{\mathbf{z}}) \\ &= -\mathbf{H}_t \end{aligned} \quad (I-1)$$

Also

$$\begin{aligned} \hat{\mathbf{z}} \times \nabla_t \times \hat{\mathbf{z}} &= \nabla_t(\hat{\mathbf{z}} \cdot \hat{\mathbf{z}}) - \hat{\mathbf{z}}(\hat{\mathbf{z}} \cdot \nabla_t) \\ &= \nabla_t \end{aligned} \quad (I-2)$$

Substituting (I-1) and (I-2) into (7.1) we get,

$$\begin{aligned}
& \frac{-j\beta}{j\omega\varepsilon_0\varepsilon_r} [\nabla_t H_z + j\beta \mathbf{H}_t] + (\nabla_t \times \hat{\mathbf{z}}) E_z + j\omega\mu_0\mu \mathbf{H}_t \\
& - j\mu_0\kappa(\hat{\mathbf{z}} \times \mathbf{H}_t) = 0 \\
& -j\beta[\nabla_t H_z + j\beta \mathbf{H}_t] + j\omega\varepsilon_0\varepsilon_r(\nabla_t \times \hat{\mathbf{z}}) E_z - \omega^2\mu_0\mu\varepsilon_0\varepsilon_r \mathbf{H}_t \\
& - j\mu_0\omega\varepsilon_0\varepsilon_r\kappa(\hat{\mathbf{z}} \times \mathbf{H}_t) = 0 \\
& \beta^2 \mathbf{H}_t - j\beta\nabla_t H_z + j\omega\varepsilon_0\varepsilon_r(\nabla_t \times \hat{\mathbf{z}}) E_z - \omega^2\mu_0\mu\varepsilon_0\varepsilon_r \mathbf{H}_t \\
& - j\mu_0\omega^2\varepsilon_0\varepsilon_r\kappa(\hat{\mathbf{z}} \times \mathbf{H}_t) = 0 \\
& \mathbf{H}_t(\beta^2 - \omega^2\mu_0\mu\varepsilon_0\varepsilon_r) - j\beta\nabla_t H_z + j\omega\varepsilon_0\varepsilon_r(\nabla_t \times \hat{\mathbf{z}}) E_z \\
& - j\mu_0\omega^2\varepsilon_0\varepsilon_r\kappa(\hat{\mathbf{z}} \times \mathbf{H}_t) = 0
\end{aligned}$$

Let  $K_1^2 = -\beta^2 + \omega^2\mu_0\mu\varepsilon_0\varepsilon_r$ , also using the identity  $\nabla_t \times \hat{\mathbf{z}} = -\hat{\mathbf{z}} \times \nabla_t$  the above equation can be re-written as

$$\begin{aligned}
& -K_1^2 \mathbf{H}_t - j\beta\nabla_t H_z - j\omega\varepsilon_0\varepsilon_r(\hat{\mathbf{z}} \times \nabla_t) E_z - j\mu_0\omega^2\varepsilon_0\varepsilon_r\kappa(\hat{\mathbf{z}} \times \mathbf{H}_t) = 0 \\
& K_1^2 \mathbf{H}_t + j\beta\nabla_t H_z + j\omega\varepsilon_0\varepsilon_r(\hat{\mathbf{z}} \times \nabla_t) E_z + j\mu_0\omega^2\varepsilon_0\varepsilon_r\kappa(\hat{\mathbf{z}} \times \mathbf{H}_t) = 0
\end{aligned} \tag{8}$$

Consider (5.2), taking  $\hat{\mathbf{z}} \times$  on both sides,

$$\begin{aligned}
& \hat{\mathbf{z}} \times \{-j\beta(\hat{\mathbf{z}} \times \mathbf{H}_t) + (\nabla_t \times H_z \hat{\mathbf{z}})\} = j\omega\varepsilon_0\varepsilon_r(\hat{\mathbf{z}} \times \mathbf{E}_t) \\
& -j\beta(\hat{\mathbf{z}} \times \hat{\mathbf{z}} \times \mathbf{H}_t) + (\hat{\mathbf{z}} \times \nabla_t \times \hat{\mathbf{z}}) H_z = j\omega\varepsilon_0\varepsilon_r(\hat{\mathbf{z}} \times \mathbf{E}_t)
\end{aligned}$$

Substituting identities from (I-1) and (I-2)

$$\mathbf{H}_t = \frac{\omega \varepsilon_0 \varepsilon_r}{\beta} (\hat{\mathbf{z}} \times \mathbf{E}_t) - \frac{1}{j\beta} \nabla_t H_z \quad (9)$$

Substituting (9) into (4.2)

$$\begin{aligned} & -j\beta(\hat{\mathbf{z}} \times \mathbf{E}_t) + (\nabla_t \times E_z \hat{\mathbf{z}}) \\ &= -j\omega\mu_0\mu \left\{ \frac{\omega \varepsilon_0 \varepsilon_r}{\beta} (\hat{\mathbf{z}} \times \mathbf{E}_t) - \frac{1}{j\beta} \nabla_t H_z \right\} \\ &+ \omega\mu_0\kappa \left\{ \hat{\mathbf{z}} \times \left( \frac{\omega \varepsilon_0 \varepsilon_r}{\beta} (\hat{\mathbf{z}} \times \mathbf{E}_t) - \frac{1}{j\beta} \nabla_t H_z \right) \right\} \end{aligned} \quad (9.1)$$

Solving the right hand side (R.H.S.) of (9.1)

$$\begin{aligned} &= -j\omega\mu_0\mu \left\{ \frac{\omega \varepsilon_0 \varepsilon_r}{\beta} (\hat{\mathbf{z}} \times \mathbf{E}_t) - \frac{1}{j\beta} \nabla_t H_z \right\} \\ &+ \omega\mu_0\kappa \left\{ \hat{\mathbf{z}} \times \left( \frac{\omega \varepsilon_0 \varepsilon_r}{\beta} (\hat{\mathbf{z}} \times \mathbf{E}_t) - \frac{1}{j\beta} \nabla_t H_z \right) \right\} \\ &= \frac{-j\omega^2 \varepsilon_0 \varepsilon_r \mu_0 \mu}{\beta} (\hat{\mathbf{z}} \times \mathbf{E}_t) + \frac{\omega\mu_0\mu}{\beta} \nabla_t H_z \\ &+ \omega\mu_0\kappa \left\{ \frac{\omega \varepsilon_0 \varepsilon_r}{\beta} (\hat{\mathbf{z}} \times \hat{\mathbf{z}} \times \mathbf{E}_t) - \frac{1}{j\beta} H_z (\hat{\mathbf{z}} \times \nabla_t) \right\} \\ &= \frac{1}{\beta} \left\{ -j\omega^2 \varepsilon_0 \varepsilon_r \mu_0 \mu (\hat{\mathbf{z}} \times \mathbf{E}_t) + \omega\mu_0\mu \nabla_t H_z - \omega^2 \mu_0 \kappa \varepsilon_0 \varepsilon_r \mathbf{E}_t \right. \\ &\quad \left. + j\omega\mu_0\kappa H_z (\hat{\mathbf{z}} \times \nabla_t) \right\} \end{aligned}$$

Substituting the above solution into (9.1)

$$\begin{aligned} & -j\beta^2(\hat{\mathbf{z}} \times \mathbf{E}_t) + \beta(\nabla_t \times \hat{\mathbf{z}})E_z \\ &= -j\omega^2 \varepsilon_0 \varepsilon_r \mu_0 \mu (\hat{\mathbf{z}} \times \mathbf{E}_t) + \omega\mu_0\mu \nabla_t H_z - \omega^2 \mu_0 \kappa \varepsilon_0 \varepsilon_r \mathbf{E}_t \\ &+ j\omega\mu_0\kappa H_z (\hat{\mathbf{z}} \times \nabla_t) \end{aligned}$$

$$\begin{aligned}
& -j\beta^2(\hat{\mathbf{z}} \times \mathbf{E}_t) + \beta(\nabla_t \times \hat{\mathbf{z}})E_z + j\omega^2\varepsilon_0\varepsilon_r\mu_0\mu(\hat{\mathbf{z}} \times \mathbf{E}_t) - \omega\mu_0\mu\nabla_t H_z \\
& + \omega^2\mu_0\kappa\varepsilon_0\varepsilon_r\mathbf{E}_t - j\omega\mu_0\kappa H_z(\hat{\mathbf{z}} \times \nabla_t) = 0
\end{aligned} \tag{9.2}$$

Taking the  $\hat{\mathbf{z}} \times$  on both sides of (9.2)

$$\begin{aligned}
& -j\beta^2(\hat{\mathbf{z}} \times \hat{\mathbf{z}} \times \mathbf{E}_t) + \beta(\hat{\mathbf{z}} \times \nabla_t \times \hat{\mathbf{z}})E_z + j\omega^2\varepsilon_0\varepsilon_r\mu_0\mu(\hat{\mathbf{z}} \times \hat{\mathbf{z}} \times \mathbf{E}_t) \\
& - \omega\mu_0\mu(\hat{\mathbf{z}} \times \nabla_t)H_z + \omega^2\mu_0\kappa\varepsilon_0\varepsilon_r(\hat{\mathbf{z}} \times \mathbf{E}_t) \\
& - j\omega\mu_0\kappa H_z(\hat{\mathbf{z}} \times \hat{\mathbf{z}} \times \nabla_t) = 0
\end{aligned}$$

Substituting the identities yield,

$$\begin{aligned}
& -j\beta^2\mathbf{E}_t + \beta\nabla_t E_z - j\omega^2\varepsilon_0\varepsilon_r\mu_0\mu\mathbf{E}_t - \omega\mu_0\mu(\hat{\mathbf{z}} \times \nabla_t)H_z + \omega^2\mu_0\kappa\varepsilon_0\varepsilon_r(\hat{\mathbf{z}} \times \mathbf{E}_t) \\
& + j\omega\mu_0\kappa H_z\nabla_t = 0
\end{aligned}$$

As  $K_1^2 = -\beta^2 + \omega^2\mu_0\mu\varepsilon_0\varepsilon_r$ , therefore

$$K_1^2\mathbf{E}_t + j\beta\nabla_t E_z - j\omega\mu_0\mu(\hat{\mathbf{z}} \times \nabla_t)H_z + j\omega^2\mu_0\kappa\varepsilon_0\varepsilon_r(\hat{\mathbf{z}} \times \mathbf{E}_t) - \omega\mu_0\kappa H_z\nabla_t = 0 \tag{10}$$

Taking the divergence ( $\nabla \cdot$ ) of (8)

$$\begin{aligned}
& \nabla \cdot [K_1^2\mathbf{H}_t + j\beta\nabla_t H_z + j\omega\varepsilon_0\varepsilon_r(\hat{\mathbf{z}} \times \nabla_t)E_z + j\mu_0\omega^2\varepsilon_0\varepsilon_r\kappa(\hat{\mathbf{z}} \times \mathbf{H}_t)] = 0 \\
& (\nabla_t - j\beta\hat{\mathbf{z}}) \\
& \cdot [K_1^2\mathbf{H}_t + j\beta\nabla_t H_z + j\omega\varepsilon_0\varepsilon_r(\hat{\mathbf{z}} \times \nabla_t)E_z \\
& + j\mu_0\omega^2\varepsilon_0\varepsilon_r\kappa(\hat{\mathbf{z}} \times \mathbf{H}_t)] = 0 \\
& K_1^2(\nabla_t \cdot \mathbf{H}_t) + j\beta(\nabla_t \cdot \nabla_t)H_z + j\omega\varepsilon_0\varepsilon_r\{\nabla_t \cdot (\hat{\mathbf{z}} \times \nabla_t)E_z\} \\
& + j\mu_0\omega^2\varepsilon_0\varepsilon_r\kappa\{\nabla_t \cdot (\hat{\mathbf{z}} \times \mathbf{H}_t)\} = 0
\end{aligned} \tag{10.1}$$

Using the identity that the dot product of orthogonal components is 0, (10.1)

becomes

$$\begin{aligned}
K_1^2(\nabla_t \cdot \mathbf{H}_t) + j\beta\nabla_t^2 H_z - j\mu_0\omega^2\varepsilon_0\varepsilon_r\kappa\{\hat{\mathbf{z}} \cdot (\nabla_t \times \mathbf{H}_t)\} &= 0 \\
(\nabla_t \cdot \mathbf{H}_t) &= \frac{1}{K_1^2}\{j\beta\nabla_t^2 H_z + j\mu_0\omega^2\varepsilon_0\varepsilon_r\kappa\{\hat{\mathbf{z}} \cdot (\nabla_t \times \mathbf{H}_t)\}\}
\end{aligned} \tag{11}$$

Consider (7)

$$\mu(\nabla_t \cdot \mathbf{H}_t) + j\kappa\{\nabla_t \cdot (\hat{\mathbf{z}} \times \mathbf{H}_t)\} - j\beta\mu_z H_z = 0$$

Using the dot and cross product identities (7) can be re-written as

$$\mu(\nabla_t \cdot \mathbf{H}_t) - j\kappa\{\hat{\mathbf{z}} \cdot (\nabla_t \times \mathbf{H}_t)\} - j\beta\mu_z H_z = 0 \tag{11.1}$$

Substituting  $\nabla_t \cdot \mathbf{H}_t$  from (11) and  $\nabla_t \times \mathbf{H}_t$  from (5.1) into (11.1)

$$\begin{aligned}
&\frac{\mu}{K_1^2}\{j\omega^2\varepsilon_0\varepsilon_r\mu_0\kappa(\hat{\mathbf{z}} \cdot (\nabla_t \times \mathbf{H}_t)) - j\beta H_z \nabla_t^2\} - j\kappa\{\hat{\mathbf{z}} \cdot \hat{\mathbf{z}}j\omega\varepsilon_0\varepsilon_r E_z\} - j\beta\mu_z H_z \\
&= 0 \\
&\frac{\mu}{K_1^2}\{j\omega^2\varepsilon_0\varepsilon_r\mu_0\kappa(\hat{\mathbf{z}} \cdot \hat{\mathbf{z}}j\omega\varepsilon_0\varepsilon_r E_z) - j\beta H_z \nabla_t^2\} + \kappa\{\omega\varepsilon_0\varepsilon_r E_z\} - j\beta\mu_z H_z \\
&= 0 \\
&-\omega^3\varepsilon_0^2\varepsilon_r^2\mu_0\kappa E_z\mu - j\beta\mu H_z \nabla_t^2 + \omega\varepsilon_0\varepsilon_r\kappa K_1^2 E_z - j\beta\mu_z K_1^2 H_z \\
&= 0
\end{aligned}$$

Simplifying the above equation gives the following expression

$$\nabla_t^2 H_z + \frac{K_1^2\mu_z H_z}{\mu} - j\frac{\beta^2 \omega\varepsilon_0\varepsilon_r\kappa E_z}{\beta\mu} + j\frac{\omega\varepsilon_0\varepsilon_r\kappa K_1^2 E_z}{\beta\mu} = 0$$

$$\left(\nabla_t^2 + \frac{K_1^2 \mu_z}{\mu}\right) H_z - j \frac{\omega \beta \varepsilon_0 \varepsilon_r \kappa_z}{\mu} E_z = 0 \quad (12)$$

Taking the divergence of (10),

$$\begin{aligned} \nabla \cdot (K_1^2 \mathbf{E}_t + j\beta \nabla_t E_z - j\omega \mu_0 \mu (\hat{\mathbf{z}} \times \nabla_t) H_z + j\omega^2 \mu_0 \kappa \varepsilon_0 \varepsilon_r (\hat{\mathbf{z}} \times \mathbf{E}_t) \\ - \omega \mu_0 \kappa H_z \nabla_t) = 0 \end{aligned} \quad (12.1)$$

Substituting expression of  $\nabla$  from (A), (12.1) becomes,

$$\begin{aligned} K_1^2 (\nabla_t \cdot \mathbf{E}_t) + j\beta (\nabla_t \cdot \nabla_t) E_z - j\omega \mu_0 \mu \{\nabla_t \cdot (\hat{\mathbf{z}} \times \nabla_t)\} H_z \\ + j\omega^2 \mu_0 \kappa \varepsilon_0 \varepsilon_r \{\nabla_t \cdot (\hat{\mathbf{z}} \times \mathbf{E}_t)\} - \omega \mu_0 \kappa H_z (\nabla_t \cdot \nabla_t) \\ - j\beta K_1^2 (\hat{\mathbf{z}} \cdot \mathbf{E}_t) + \beta^2 E_z (\hat{\mathbf{z}} \cdot \nabla_t) - \beta \omega \mu_0 \mu \{\hat{\mathbf{z}} \cdot (\hat{\mathbf{z}} \times \nabla_t)\} H_z \\ + \beta \omega^2 \mu_0 \kappa \varepsilon_0 \varepsilon_r \{\hat{\mathbf{z}} \cdot (\hat{\mathbf{z}} \times \mathbf{E}_t)\} + j\beta \kappa \omega \mu_0 H_z (\hat{\mathbf{z}} \cdot \nabla_t) = 0 \end{aligned}$$

Further simplification yields (13)

$$K_1^2 (\nabla_t \cdot \mathbf{E}_t) + j\beta \nabla_t^2 E_z - j\omega^2 \mu_0 \kappa \varepsilon_0 \varepsilon_r \{\hat{\mathbf{z}} \cdot (\nabla_t \times \mathbf{E}_t)\} - \omega \mu_0 \kappa H_z \nabla_t^2 = 0 \quad (13)$$

Substituting (4) and (6) into (13) and simplifying gives us,

$$\begin{aligned} j\beta K_1^2 E_z - \frac{\omega^3 \mu_0 \mu_z \kappa \varepsilon_0 \varepsilon_r H_z}{j\beta} + E_z \nabla_t^2 - \frac{\omega \mu_0 \kappa \nabla_t^2 H_z}{j\beta} = 0 \\ E_z (K_1^2 + \nabla_t^2) + \frac{j(\omega^2 \varepsilon_0 \varepsilon_r \mu_0 \mu)(\omega \mu_0 \mu_z \kappa)}{\beta \mu} H_z + \frac{j\omega \mu_0 \kappa \nabla_t^2 H_z}{\beta} = 0 \\ E_z (K_1^2 + \nabla_t^2) + \frac{j(K_1^2 + \beta^2)(\omega \mu_0 \mu_z \kappa)}{\beta \mu} H_z + \frac{j\omega \mu_0 \kappa \nabla_t^2 H_z}{\beta} = 0 \end{aligned}$$

$$E_z(K_1^2 + \nabla_t^2) + \frac{j\omega\mu_0\kappa}{\beta}H_z \left\{ \nabla_t^2 + \frac{K_1^2\mu_z}{\mu} \right\} + \frac{j\beta\omega\mu_0\mu_z\kappa H_z}{\mu} = 0$$

Substituting value of  $\nabla_t^2 + \frac{K_1^2\mu_z}{\mu}$  from (10), we get (14)

$$E_z \left( K_1^2 + \nabla_t^2 - \frac{\omega^2\varepsilon_0\varepsilon_r\mu_0\kappa^2}{\mu} \right) + \frac{j\beta\omega\mu_0\mu_z\kappa H_z}{\mu} = 0 \quad (14)$$

For the sake of simplicity, assume

$$\begin{aligned} c &= K_1^2 - \frac{\omega^2\varepsilon_0\varepsilon_r\mu_0\kappa^2}{\mu} \\ d &= \frac{\beta\omega\mu_0\mu_z\kappa}{\mu} \\ f &= \frac{K_1^2\mu_z}{\mu} \\ g &= \frac{\beta\omega\varepsilon_0\varepsilon_r\kappa}{\mu} \end{aligned} \quad (B)$$

Using the substitutions of (B), (12) and (14) can be re-written as,

$$(\nabla_t^2 + f)H_z - jgE_z = 0 \quad (14.1)$$

$$(\nabla_t^2 + c)E_z + jdH_z = 0 \quad (14.2)$$

Substituting  $E_z$  from (14.1) into (14.2) and simplifying gives us,

$$\begin{aligned} &\{(\nabla_t^2)^2 + \nabla_t^2(f + c) + (fc - dg)\}H_z = 0 \\ &\left[ \nabla_t^2 - \left\{ \frac{-(f + c) \pm \sqrt{(f + c)^2 - 4(fc - dg)}}{2} \right\} \right] H_z = 0 \end{aligned}$$

$$\left[ \nabla_t^2 + \left\{ \frac{(f+c) + \sqrt{(f+c)^2 + 4dg}}{2} \right\} \right] \left[ \nabla_t^2 + \left\{ \frac{(f+c) - \sqrt{(f+c)^2 + 4dg}}{2} \right\} \right] H_z = 0 \quad (14.3)$$

Let

$$s_1^2 = \frac{(f+c) + \sqrt{(f+c)^2 + 4dg}}{2}$$

$$s_2^2 = \frac{(f+c) - \sqrt{(f+c)^2 + 4dg}}{2}$$

(14.3) written as,

$$(\nabla_t^2 + s_1^2)(\nabla_t^2 + s_2^2)H_z = 0 \quad (15)$$

Similarly,

$$(\nabla_t^2 + s_1^2)(\nabla_t^2 + s_2^2)E_z = 0 \quad (16)$$

As observed (15) and (16) are homogeneous partial differential equations (PDE) of the second order. In order to solve (15) and (16), the separation of variables method principle has been used where  $\frac{\partial}{\partial z} = -j\beta z$  is already incorporated into the equations.

$$\stackrel{(15)}{\implies} H_z(r, \theta) = R'(r)\theta'(\theta)$$

$$\stackrel{(16)}{\implies} E_z(r, \theta) = R(r)\theta(\theta) \quad (16.1)$$

Substituting  $E_z(r, \theta)$  and  $H_z(r, \theta)$  in (15) and (16), we see that the general solution for a second order PDE is of the form,

$$\frac{d^2 R}{dr^2} + \frac{1}{r} \frac{dR}{dr} + \lambda R = 0 \quad (16.2)$$

$$\frac{d^2 \theta}{dr^2} - \lambda \theta = 0$$

For our case the equations are

$$\frac{d^2 R}{dr^2} + \frac{1}{r} \frac{dR}{dr} + \left( s_{1,2}^2 - \frac{n^2}{r^2} \right) = 0$$

$$\frac{d^2 \theta}{dr^2} + n^2 \theta = 0$$

(16.1) is a Bessel's Equation and (16.2) is an ODE of order 2, solving these two equations gives us,

$$E_z = [A_n J_n(s_1 r) + B_n J_n(s_2 r)] e^{-jn\theta} \quad (17)$$

$$H_z = [\tau_1 A_n J_n(s_1 r) + \tau_2 B_n J_n(s_2 r)] e^{-jn\theta} \quad (18)$$

where

$$\tau_1 = \frac{-jg}{s_1^2 - f}$$

and

$$\tau_2 = \frac{-jg}{s_2^2 - f}$$

To find the field components of the transverse field we have to use (8) and the fact that

$$H_t = H_r \hat{r} + H_\phi \hat{\phi}$$

$$\nabla_t = \frac{\partial}{\partial r} \hat{r} + \frac{1}{r} \frac{\partial}{\partial \phi} \hat{\phi}$$

$$\stackrel{(8)}{\Rightarrow} K_1^2 \mathbf{H}_t + j\beta \nabla_t H_z + j\omega \varepsilon_0 \varepsilon_r (\hat{\mathbf{z}} \times \nabla_t) E_z + j\mu_0 \omega^2 \varepsilon_0 \varepsilon_r \kappa (\hat{\mathbf{z}} \times \mathbf{H}_t) = 0$$

$$\begin{aligned} & K_1^2 H_r \hat{r} + K_1^2 H_\phi \hat{\phi} \\ & + j\beta \left( \frac{\partial}{\partial r} \hat{r} + \frac{1}{r} \frac{\partial}{\partial \phi} \hat{\phi} \right) H_z + j\omega \varepsilon_0 \varepsilon_r \left( \hat{\mathbf{z}} \times \left( \frac{\partial}{\partial r} \hat{r} + \frac{1}{r} \frac{\partial}{\partial \phi} \hat{\phi} \right) \right) E_z \\ & + j\mu_0 \omega^2 \varepsilon_0 \varepsilon_r \kappa (\hat{\mathbf{z}} \times (H_r \hat{r} + H_\phi \hat{\phi})) = 0 \end{aligned} \quad (18.2)$$

Simplifying (18.2) and separating the  $\hat{r}$  and  $\hat{\phi}$  components we get

$$\begin{aligned} \hat{r} \Rightarrow & K_1^2 H_r - j\mu_0 \omega^2 \varepsilon_0 \varepsilon_r \kappa H_\phi + j\beta \frac{\partial H_z}{\partial \phi} - \frac{j\omega \varepsilon_0 \varepsilon_r}{r} \frac{\partial E_z}{\partial \phi} = 0 \\ H_\phi = & \frac{1}{j\mu_0 \omega^2 \varepsilon_0 \varepsilon_r \kappa} \left\{ K_1^2 H_r + j\beta \frac{\partial H_z}{\partial \phi} - \frac{j\omega \varepsilon_0 \varepsilon_r}{r} \frac{\partial E_z}{\partial \phi} \right\} \end{aligned} \quad (19)$$

or

$$H_\phi = \frac{1}{jQ} \left\{ K_1^2 H_r + j\beta \frac{\partial H_z}{\partial \phi} - \frac{jR}{r} \frac{\partial E_z}{\partial \phi} \right\}$$

Where  $Q = \mu_0 \omega^2 \varepsilon_0 \varepsilon_r \kappa$  and  $R = \omega \varepsilon_0 \varepsilon_r$

Similarly

$$\hat{\phi} \Rightarrow K_1^2 H_\phi - jQH_r + \frac{j\beta}{r} \frac{\partial H_z}{\partial \phi} - jR \frac{\partial E_z}{\partial \phi} = 0 \quad (20)$$

Substituting (19) in to (20) and replacing  $\frac{\partial}{\partial \varphi} = -jn$

$$\frac{K_1^2}{jQ} \left[ K_1^2 H_r + j\beta \frac{\partial H_z}{\partial r} - j \frac{R}{r} \frac{\partial E_z}{\partial \varphi} - \frac{Q^2}{K_1^2} H_r - \frac{\beta Q}{r K_1^2} \frac{\partial H_z}{\partial \varphi} - \frac{QR}{K_1^2} \frac{\partial E_z}{\partial \varphi} \right] = 0$$

$$K_1^2 H_r + j\beta \frac{\partial H_z}{\partial r} - \frac{R}{r} n E_z - \frac{Q^2}{K_1^2} H_r + \frac{j\beta Q}{r K_1^2} n H_z - \frac{QR}{K_1^2} \frac{\partial E_z}{\partial r} = 0$$

Substituting  $Q, R$  and  $K_1^2$  we get,

$$\begin{aligned} (-\beta^2 + \omega^2 \mu_0 \mu \varepsilon_0 \varepsilon_r) H_r + j\beta \frac{\partial H_z}{\partial r} - \frac{\omega \varepsilon_0 \varepsilon_r}{r} n E_z - \frac{(\mu_0 \omega^2 \varepsilon_0 \varepsilon_r \kappa)^2}{-\beta^2 + \omega^2 \mu_0 \mu \varepsilon_0 \varepsilon_r} H_r \\ + \frac{j\beta \mu_0 \omega^2 \varepsilon_0 \varepsilon_r \kappa}{r(-\beta^2 + \omega^2 \mu_0 \mu \varepsilon_0 \varepsilon_r)} n H_z - \frac{(\mu_0 \omega^2 \varepsilon_0 \varepsilon_r \kappa) \omega \varepsilon_0 \varepsilon_r}{(-\beta^2 + \omega^2 \mu_0 \mu \varepsilon_0 \varepsilon_r)} \frac{\partial E_z}{\partial r} = 0 \end{aligned} \quad (20.1)$$

Let  $\bar{\beta} = \frac{\beta}{K_0}$  where  $K_0 = \omega^2 \varepsilon_0 \mu_0$

$$\begin{aligned} \stackrel{(20.1)}{\implies} H_r \{(\mu \varepsilon_r - \bar{\beta}^2) - \varepsilon_r^2 \kappa^2\} + \frac{j\bar{\beta}}{K_0} \left\{ \left( \mu \varepsilon_r - \bar{\beta}^2 \frac{\partial H_z}{\partial r} + \frac{\varepsilon_r \kappa n}{r} H_z \right) \right\} \\ - \frac{\varepsilon_r}{K_0} \sqrt{\frac{\varepsilon_0}{\mu_0}} \left\{ \frac{n}{r} (\mu \varepsilon_r - \bar{\beta}^2) E_z + \varepsilon_r \kappa \frac{\partial E_z}{\partial r} \right\} = 0 \end{aligned}$$

$$\begin{aligned} \frac{2\pi}{\lambda_0} \{(\mu \varepsilon_r - \bar{\beta}^2) - \varepsilon_r^2 \kappa^2\} H_r \\ = \frac{\varepsilon_r}{K_0} \sqrt{\frac{\varepsilon_0}{\mu_0}} \left\{ \frac{n}{r} (\mu \varepsilon_r - \bar{\beta}^2) E_z + \varepsilon_r \kappa \frac{\partial E_z}{\partial r} \right\} - \frac{j\bar{\beta}}{K_0} \left\{ \left( \mu \varepsilon_r - \bar{\beta}^2 \frac{\partial H_z}{\partial r} + \frac{\varepsilon_r \kappa n}{r} H_z \right) \right\} \end{aligned} \quad (21)$$

Similarly,

$$\begin{aligned}
& \frac{2\pi}{\lambda_0} \{(\mu\varepsilon_r - \bar{\beta}^2) - \varepsilon_r^2 \kappa^2\} H_\varphi \\
&= -j\varepsilon_r \sqrt{\frac{\varepsilon_0}{\mu_0}} \left\{ \frac{\varepsilon_r \kappa n}{r} H_z + \frac{n}{r} (\mu\varepsilon_r - \bar{\beta}^2) \frac{\partial E_z}{\partial r} \right\} \\
&\quad - \bar{\beta} \left\{ \left( \frac{n}{r} (\mu\varepsilon_r - \bar{\beta}^2) H_z + \varepsilon_r \kappa \frac{\partial H_z}{\partial r} \right) \right\}
\end{aligned} \tag{22}$$

$$\begin{aligned}
& \frac{2\pi}{\lambda_0} \{(\mu\varepsilon_r - \bar{\beta}^2) - \varepsilon_r^2 \kappa^2\} E_r \\
&= -\sqrt{\frac{\mu_0}{\varepsilon_0}} \left\{ \kappa \bar{\beta}^2 \frac{\partial H_z}{\partial r} + \frac{\mu n}{r} \left( \mu\varepsilon_r - \bar{\beta}^2 - \frac{\varepsilon_r \kappa^2}{\mu} \right) H_z \right\} \\
&\quad - j\bar{\beta} \left\{ \left( (\mu\varepsilon_r - \bar{\beta}^2) \frac{\partial E_z}{\partial r} + \frac{\varepsilon_r \kappa n}{r} E_z \right) \right\}
\end{aligned} \tag{23}$$

$$\begin{aligned}
& \frac{2\pi}{\lambda_0} \{(\mu\varepsilon_r - \bar{\beta}^2) - \varepsilon_r^2 \kappa^2\} E_\varphi \\
&= j \sqrt{\frac{\mu_0}{\varepsilon_0}} \left\{ \frac{\kappa n \bar{\beta}^2}{r} H_z + \mu \left( \mu\varepsilon_r - \bar{\beta}^2 - \frac{\varepsilon_r \kappa^2}{\mu} \right) \frac{\partial H_z}{\partial r} \right\} \\
&\quad - \bar{\beta} \left\{ \left( \frac{n}{r} (\mu\varepsilon_r - \bar{\beta}^2) E_z + \kappa n \frac{\partial E_z}{\partial r} \right) \right\}
\end{aligned} \tag{24}$$

For a fully filled ferrite circular waveguide, the boundary conditions are:  $H_z=0$  at  $r=R$  and  $H_\varphi=0$  at  $r=R$ ; all tangential components are zero at the edge of the ferrite cylinder.

Substituting the corresponding values from (17), (18)

$$\text{Let } P = \mu\varepsilon_r - \bar{\beta}^2,$$

$$\begin{aligned}
&\stackrel{(24)}{\implies} -\bar{\beta} \left\{ \frac{nP}{r} (A_n J_n(s_1 r) + B_n J_n(s_2 r)) + \kappa \varepsilon_r (A_n J_n'(s_1 r) + B_n J_n'(s_2 r)) \right\} \\
&\quad + j \sqrt{\frac{\mu_0}{\varepsilon_0}} \left[ \frac{\kappa n \bar{\beta}^2}{R} \{ \tau_1 A_n J_n(s_1 r) + \tau_2 B_n J_n(s_2 r) \} \right. \\
&\quad \left. + \mu \left( P - \frac{\varepsilon_r \kappa^2}{\mu} \right) \{ \tau_1 A_n J_n'(s_1 r) + \tau_2 B_n J_n'(s_2 r) \} \right] = 0 \tag{25}
\end{aligned}$$

Substituting  $A_n$  into (25) we get,

$$\begin{aligned}
&-\bar{\beta} \left\{ \frac{nP}{r} \left( \left( -B_n \frac{J_n(s_2 R)}{J_n(s_1 R)} \right) J_n(s_1 R) + B_n J_n(s_2 R) \right) \right. \\
&\quad \left. + \kappa \varepsilon_r \left( -B_n \left( \frac{J_n(s_2 R)}{J_n(s_1 R)} \right) J_n'(s_1 R) + B_n J_n'(s_2 R) \right) \right\} \\
&\quad + j \sqrt{\frac{\mu_0}{\varepsilon_0}} \left[ \frac{\kappa n \bar{\beta}^2}{R} \left\{ \tau_1 \left( -B_n \frac{J_n(s_2 R)}{J_n(s_1 R)} \right) J_n(s_1 R) + \tau_2 B_n J_n(s_2 R) \right\} \right. \\
&\quad \left. + \mu \left( P - \frac{\varepsilon_r \kappa^2}{\mu} \right) \left\{ \tau_1 \left( -B_n \frac{J_n(s_2 R)}{J_n(s_1 R)} \right) J_n'(s_1 R) \right. \right. \\
&\quad \left. \left. + \tau_2 B_n J_n'(s_2 R) \right\} \right] = 0 \tag{25.1}
\end{aligned}$$

Substituting the values of  $\tau_1$  and  $\tau_2$  and further simplifying (25.1) leads to,

$$\begin{aligned}
& \frac{J_n'(s_1 R)}{J_n(s_1 R)} \left\{ s_1 \frac{\beta \kappa \varepsilon_r}{K_0} \right. \\
& \quad \left. - s_1 \mu \sqrt{\frac{\mu_0}{\varepsilon_0}} \left( \varepsilon_r \mu - \frac{\beta^2}{K_0^2} - \frac{\varepsilon_r \kappa^2}{\mu} \right) \left( \frac{\frac{\omega \beta \kappa \varepsilon_0 \varepsilon_r}{\mu}}{s_1^2 - \frac{(-\beta^2 + K_0^2 \mu \varepsilon_r) \mu_z}{\mu}} \right) \right\} \\
& \quad - \frac{J_n'(s_2 R)}{J_n(s_2 R)} \left\{ s_2 \frac{\beta \kappa \varepsilon_r}{K_0} \right. \\
& \quad \left. - s_2 \mu \sqrt{\frac{\mu_0}{\varepsilon_0}} \left( \varepsilon_r \mu - \frac{\beta^2}{K_0^2} - \frac{\varepsilon_r \kappa^2}{\mu} \right) \left( \frac{\frac{\omega \beta \kappa \varepsilon_0 \varepsilon_r}{\mu}}{s_2^2 - \frac{(-\beta^2 + K_0^2 \mu \varepsilon_r) \mu_z}{\mu}} \right) \right\} \\
& \quad - \sqrt{\frac{\mu_0}{\varepsilon_0}} \frac{\kappa n \beta^2}{R K_0^2} \frac{\omega \beta \kappa \varepsilon_0 \varepsilon_r}{\mu} \left\{ \frac{s_2^2 - s_1^2}{(s_1^2 - f)(s_2^2 - f)} \right\} = 0 \tag{25.2}
\end{aligned}$$

Substituting  $\mu_{eff} = \frac{\mu^2 - \kappa^2}{\mu}$  in (25.2) and simplifying gives us,

$$\begin{aligned}
& \frac{J_n'(s_1 R)}{J_n(s_1 R)} \left\{ s_1 - (K_0^2 \mu_{eff} \varepsilon_r - \beta^2) \left( \frac{s_1}{(s_1^2 - f)} \right) \right\} \\
& \quad - \frac{J_n'(s_2 R)}{J_n(s_2 R)} \left\{ s_2 - (K_0^2 \mu_{eff} \varepsilon_r - \beta^2) \left( \frac{s_2}{(s_2^2 - f)} \right) \right\} \\
& \quad - \frac{\kappa n \beta^2}{\mu R} \left\{ \frac{s_2^2 - s_1^2}{(s_1^2 - f)(s_2^2 - f)} \right\} = 0 \\
& \quad \left( \frac{s_1^2}{(s_1^2 - f)} \right) \left[ \frac{J_n'(s_1 R)}{J_n(s_1 R)} \left\{ \frac{s_1^2 - f}{s_1} - \frac{(K_0^2 \mu_{eff} \varepsilon_r - \beta^2)}{s_1} \right\} \right] \\
& \quad - \left( \frac{s_2^2}{(s_2^2 - f)} \right) \left[ \frac{J_n'(s_2 R)}{J_n(s_2 R)} \left\{ \frac{s_2^2 - f}{s_2} - \frac{(K_0^2 \mu_{eff} \varepsilon_r - \beta^2)}{s_2} \right\} \right] \\
& \quad - \frac{\kappa n \beta^2}{\mu R} \left\{ \frac{s_2^2 - s_1^2}{s_1^2 s_2^2} \frac{s_1^2 s_2^2}{(s_1^2 - f)(s_2^2 - f)} \right\} = 0 \tag{26}
\end{aligned}$$

# REFERENCES

- [1] S. Foley, "World War II technology that changed warfare-radar and bombsights," in *Academic Symposium of Undergraduate Scholarship*, 2011.
- [2] C. Uluisik, "Antenna systems with beam forming and beam steering capabilities for HF skywave radars," *Turk Journal of Electrical Engineering and Computer Science*, vol. 18, no. 3, pp. 485-498, 2010.
- [3] A. P. Feresidis, "Artificial magnetic conductor surfaces and their application to LOS profile high-gain planar antennas," *IEEE Transactions on Antennas and Propagation*, vol. 53, pp. 209-215, 2005.
- [4] J. Che and T. Kim, "Microstrip array antenna for PCs and IMT-2000 base station," in *2000 Asia-Pacific Microwave Conference*, Seoul, 2000.
- [5] C. A. Balanis, *Antenna Fundamentals: Theory and Design*, NJ: Wiley, 2006.
- [6] T. K. Singh, P. Kumar, T. Chakravarty, G. Singh and S. Bhooshan, "A novel digital beamformer with low angle resolution for vehicle tracking radar," *Progress in Electromagnetic Research, (PIER)*, vol. 66, pp. 229-237, 2006.
- [7] R. C. Hansen, *Phased Array Antennas*, John Wiley and Sons, 1998.
- [8] Y. Li, Q. Zhu, Y. Yan and S. Xu, "Design of a 1x20 series feed network with composite right/left-handed transmission line," *Progress in Electromagnetic Research, PIER*, vol. 89, pp. 311-324, 2009.
- [9] J. Ju, D. Kim and J. Choi, "Fabry-Perot cavity antenna with lateral metallic walls for WiBro base station applications," *Electronic Letters*, vol. 45, no. 3, pp. 141-142, 2009.
- [10] R. Sauleau, "Fabry-Perot resonators," in *Encyclopedia of RF and Microwave Engineering*, Wiley, 2005, pp. 1381-1401.
- [11] J. H. Yoon, S. M. Lee, G. C. An and H. C. Lee, "Radiation characteristics of microstrip antenna on the superstrate-loaded cylindrical bianisotropic substrates," in *Proceedings of the IEEE Region 10 Conference*, 1999.

- [12] A. Kotnala, P. Juyal, A. Mittal and A. De, "Investigation of cavity reflex antenna using circular patch type FSS superstrate," *Progress in Electromagnetic Research B*, vol. 42, pp. 141-161, 2012.
- [13] V. Rabinovich and N. Alexandrov, "Typical array geometries and basic beam steering methods," in *Antenna Arrays and Automotive Applications*, New York, Springer, 2013, pp. 23-52.
- [14] D. H. Lee, R. Mittra and W. S. Park, "Design of frequency selective surface superstrates for scanning mmicrostrip patch array antenna," *MICrowave and optical technology letters*, vol. 49, no. 12, pp. 3184-3187, 2007.
- [15] H. Attia, L. Yousefi, M. M. Bait-Suwailem and M. S. Boybay, "Enhanced-gain microstrip antenna using engineered magnetic superstrates," *IEEE Antennas and Wireless Propagation Letters*, vol. 8, pp. 1198-1201, 2009.
- [16] P. Goel and K. J. Vinoy, "A low-cost phased array antenna integrated with phase shifters cofabricated on the laminate," *Progress in Electromagnetic Research B*, vol. 30, pp. 255-277, 2011.
- [17] M. F. Iskander, N. Celik and W. Kim, "Low cost phased array antennas using analog and digital phase shifter technologies," in *2007 IEEE Antennas and Propagation Society International Symposium*, Honolulu, 2007.
- [18] A. Chauraya, C. Panagamuwa and J. Vardaxoglou, "Beam scanning antenna with photonicly tuned EBG phase shifters," in *IEEE Antennas and Propagation Society International Symposium*, Albuquerque, 2006.
- [19] Y. Hao and R. Mittra, *FDTD Modelling of Metamaterials: Theory and Applications*, Artech House, 2009.
- [20] C.-C. Hu, C. F. Jou and J.-J. Wu, "A two-dimensional beam-scanning linear active leak-wave antenna array," *IEEE Microwave and Guided Wave Letters*, vol. 9, no. 3, pp. 102-104, 1999.
- [21] R. Harrington, "Reactively controlled directive arrays," *IEEE transactions on Antennas and Propagation*, vol. 26, no. 3, pp. 390-395, 1978.
- [22] H. Kawakami and T. Ohira, "Electrically steerable passive array radiator (ESPAR) antennas," *IEEE Antennas and Propagation Magazine*, vol. 47, no. 2, pp. 43-49, 2005.

- [23] R. J. Dinger, "A planar version of a 4.0 GHz reactively steered adaptive array," *IEEE Transactions on Antennas and Propagation*, Vols. AP-34, no. 3, pp. 427-431, 1986.
- [24] Y. Yusuf and X. Gong, "A low-cost patch antenna phased array with analog beam steering using mutual coupling and reactive loading," *IEEE Antennas and Wireless Propagation Letters*, vol. 7, pp. 81-84, 2008.
- [25] Y.-G. Kim, T.-H. Kim, S.-G. Kang and I.-G. Choi, "Electronically beam scanning array antenna for 5.8 GHz ISM band application," in *Proceedings of 40th European Microwave Conference*, Paris, 2010.
- [26] W. Cao, Y. Xiang, B. Zhang, A. Liu, T. Yu and D. Guo, "A low-cost compact patch antenna with beam steering based on CSRR-loaded ground," *IEEE Antennas and Wireless Propagation Letters*, vol. 10, pp. 1520-1523, 2011.
- [27] M. S. Sharawi, F. Sultan and D. N. Aloi, "A comparative performance analysis of two printed circular arrays for power-based vehicle localization applications," *International Journal of Antennas and Propagation*, vol. 2012, pp. 1-8, 2012.
- [28] M. S. Sharawi, F. Sultan and D. N. Aloi, "An 8-element printed V-shaped circular antenna array for power based vehicular localization," *IEEE Antennas and Wave Propagation Letters*, vol. 11, pp. 1133-1136, 2012.
- [29] M. T. Ali, T. A. Rahman, M. R. Kamarudin, M. N. Md Tan and R. Sauleau, "A novel of reconfigurable planar antenna array (RPAA) with beam steering control," *Progress In Electromagnetics Research B*, vol. 20, pp. 125-146, 2010.
- [30] A. Hammami, R. Ghayoula and A. Gharsallah, "Design of planar array antenna with chebyshev method and genetic algorithm," *International Journal of Research and Reviews in Applied Sciences*, vol. 8, no. 2, pp. 227-233, 2011.
- [31] M. A. Abdalla, K. Phang and G. V. Eleftheriades, "A planar electronically steerable patch array using tunable PRI/NRI phase shifters," *IEEE Transactions on Microwave Theory and Techniques*, vol. 57, no. 3, pp. 531-541, 2009.
- [32] Precision Photonics Corporation, "Basic Physics and Design of Etalons," 2003.
- [33] R. Bacon, "Fabry-Perto Interferometer," University of Surrey, 2010.
- [34] G. V. Trentini, "Partially reflecting sheet array," *IRE Transactions of Antennas and Propagation*, vol. 4, no. 4, pp. 666-671, 1956.

- [35] D. Jackson and A. A. Oliner, "A leaky wave analysis of the high gain printed antenna configuration," *IEEE Transactions on Antennas and Propagation*, vol. 36, pp. 905-910, 1988.
- [36] Z.-G. Liu and T.-H. Liu, "Comparative study of Fabry-Perot resonator antenna with PMC and PEC ground plane," *Progress in Electromagnetic Research B*, vol. 32, pp. 299-317, 2011.
- [37] Y. Li, K. Yoo, R. Mittra, G. Lu, D. Zeng and Y. Guan, "Directivity enhancement of microstrip antennas using dielectric superstrates," in *International Conference on Applications of Electromagnetism and Student Innovation Competition Awards*, 2010.
- [38] F. Sultan, S. S. Iqbal and R. Hussain, "Design of a reduced size 7-patch antenna array with FSS based directivity enhancement," in *2013 IEEE International Symposium on Phased Array Systems and Technology*, Waltham, 2013.
- [39] R. Gardelli, M. Albani and F. Capolino, "EBG superstrates for dual polarized sparse arrays," in *Proceedings of IEEE International Symposium of Antenna Propagation Society*, 2005.
- [40] R. Gardelli, M. Albani and F. Capolino, "Array thinning by using antennas in a Fabry-Perot cavity for gain enhancement," *IEEE Transactions on Antennas and Propagation*, vol. 54, no. 7, pp. 1979-1990, 2006.
- [41] J. R. Kelly and A. P. Feresidis, "Array antenna with increased element separation based on Fabry-Perot resonant cavity with AMC walls," *IEEE Transactions on Antennas and Propagation*, vol. 57, no. 3, pp. 682-687, 2009.
- [42] Y. J. Guo and J. L. Gomez-Tornero, "Reconfigurable Fabry-Perot leaky-wave antennas," in *2013 International Workshop on Antenna Technology*, Karlsruhe, 2013.
- [43] H. Attia, O. Siddiqui and O. Ramhi, "Theoretical and experimental demonstration of beam-steering of patch antenna with superstrate," in *2012 International Symposium of Antenna and Propagation Society*, 2012.
- [44] Z. Liu, W. Zhang, D. Fu, Y. Gu and Z. Ge, "Broadband fabry-perot resonator printed antennas using FSS superstrate with dissimilar size," *Microwave and Optical Technology Letters*, vol. 50, no. 6, pp. 1623-1627, 2007.

- [45] H. Bukhari and K. Sarabandi, "Ultra-wideband printed slot antenna with graded index superstrate," *IEEE Transactions on Antennas and Propagation*, vol. 61, no. 10, pp. 5278-5282, 2013.
- [46] A. Ghasemi, S. N. Burokur, A. Dhouibi and A. Lustrac, "High beam steering Fabry-Perot leaky-wave antennas," *IEEE Antennas and Wireless Propagation Letters*, vol. 12, pp. 261-264, 2013.
- [47] A. Foroozesh and L. Shafai, "Investigation into the effects of the patch-type FSS superstrate on the high-gain cavity resonance antenna design," *IEEE Transactions on Antennas and Propagation*, vol. 58, no. 2, pp. 258-270, 2010.
- [48] N. Zhu and R. Ziolkowski, "Photoconductive THz antenna designs with high radiation efficiency, high directivity, and high aperture efficiency," *IEEE Transactions on Terahertz Science and Technology*, vol. 3, no. 6, pp. 721-730, 2013.
- [49] R. Pourush, G. S. Tyagi, G. P. Srivastava and P. K. S. Pourush, "Radiation performance of switchable ferrite microstrip antenna array," *IEEE Antennas and Wireless Propagation Letters*, vol. 5, 2006.
- [50] J. Lee, Y. -K. Hong, S. Bae, G. S. Abo, W. -M. Seong and G. H. Kim, "Mineature long-term evollution (LTE) MIMO ferrite antenna," *IEEE Antennas and Wireless Propagation Letters*, vol. 10, 2011.
- [51] J. Lee, Y. -K. Hang, W. Lee, G. S. Abo and J. Park, "Role of small permability in gegahertz ferrite antenna performance," *IEEE Magnetics Letters*, vol. 4, 2013.
- [52] M. I. Kitra, C. J. Panagamuwa, P. McEnvoy, J. C. Vardaxoglov and J. R. James, "Low SAR ferrite handset antenna designs," *IEEE Transactions on Antennas and Propagation*, vol. 55, no. 4, 2077.
- [53] W.-K. Lin, L.-S. Chen and C.-H. Wang, "Effect of Ba-Co ferrite on bandwidth of a monopole antenna," *Microwave and Optical Technology Letters*, vol. 56, no. 5, pp. 1181-1184, 2014.
- [54] M. Sigalov, R. Shavit, R. Joffe and E. O. Kamenetskii, "Manipulation of the radiation characteristics of a patch antenna by small ferrite disks inserted in its cavity domain," *IEEE Transactions on Antennas and Propagation*, vol. 61, no. 5, pp. 2371-2379, 2013.

- [55] A. A. Mavridis, G. A. Kyriacou and J. N. Sahalos, "Analysis of circular patch antenna tuned by a ferrite post," *Microwave and Optical Technology Letters*, vol. 46, no. 3, pp. 234-237, 2005.
- [56] A. A. Mavridis and G. A. Kyriacou, "On the design of patch antennas tuned by transversely magnetized lossy ferrite including a novel resonating mode," *Progress in Electromagnetics Research (PIER)*, vol. 62, pp. 165-192, 2006.
- [57] A. Henderson, J. R. James, A. Fray and G. D. Evans, "New ideas for beam scanning using magnetized ferrite," *IEE Colloquium on Electronically Scanned Antennas*, 1988.
- [58] J. C. Batchelor and R. J. Langley, "Beam scanning using microstrip line on biased ferrite," *Electronic Letters*, vol. 33, no. 8, pp. 645-646, 1997.
- [59] I. Wolff, "From antennas to microwave systems - LTCC as an integration technology for space applications," in *3rd European Conference on Antennas and propagation*, 2009.
- [60] T. Tajima, H. J. Soug, K. Ajito, M. Yaita and N. Kukutsu, "300 GHz step-profiled corrugated horn antennas integrated in LTCC," *IEEE Transactions on Antennas and Propagation*, vol. 62, no. 11, 2014.
- [61] A. Shamim, J. R. Bray, N. Hojjat and L. Roy, "Ferrite LTCC-based antennas for tunable SoP applications," *IEEE Transactions on Components, Packaging and Manufacturing*, vol. 1, no. 7, 2011.
- [62] C. Kittel, *Introduction to Solid State Physics*, Wiley, 1996.
- [63] U. Ozgur and Y. A. a. H. Morkoc, "Microwave ferrites, part 1: fundamental properties," *Journal of Materials Science: Materials in Electronics*, vol. 20, no. 9, pp. 789-834, 2009.
- [64] W. D. C. a. D. G. Rethwisch, *Material Science and Engineering: An Introduction*, John Wiley and Sons, 2014.
- [65] H. V. Keer, *Principles of Solid State*, New Age International Publishers, 1993.
- [66] A. J. B. Fuller, *Ferrites at Microwave Frequencies*, Peter Peregrinus, 1987.
- [67] H. Suhl and L. R. Walker, "Faraday rotation of guided waves," *Physics Review*, vol. 86, 1952.

- [68] A. G. Melkov, *Magnetization Oscillations and Waves*, CRC Press, 1996.
- [69] D. Kim, J. Ju and J. Choi, "A mobile communication base station antenna using a genetic algorithm based Fabry-Perot resonance optimization," *IEEE transactions on antennas and propagation*, vol. 60, no. 2, 2012.
- [70] L. C. Godara, "Applications of antenna arrays to mobile communications, PART II: Beam-forming and direction-of-arrival considerations," *IEEE*, vol. 85, no. 8, pp. 1195-1245, 1997.
- [71] H. Boutayed, K. Mahdjoubi, A. -C. Tarot and T. A. Denidni, "Directivity of an antenna wmbded inside a Fabry-Perot cavity: analysis and design," *Microwave and Optical Technology Letters*, pp. 12-17, 2006.
- [72] J. B. Pendry, A. J. Holden, D. J. Robbins and W. J. Stewart, "Magnetism from conductors and enhanced non-linear phenomena," *IEEE Transactions on Microwave Theory technology*, pp. 2075-2084, 1999.
- [73] S. Linden, C. Enkrich, W. Wegener, J. Zhou, T. Koschny and C. M. Soukoulis, "Magnetic response of metamaterials at 100 THz," *Science*, vol. 306, pp. 1353-1361, 2004.
- [74] K. Bi, G. Dong, X. Fu and J. Zn, "Ferrite based metamaterials with thermo-tunable negative refractive index," *Applied Physics Letters*, vol. 103, no. 13, 2013.
- [75] D. R. Smith, J. B. Pendry and M. C. K. Wiltshire, "Metamaterial and negative refractive index," *Science*, vol. 305, 2004.
- [76] G. Zhun, "Designing a square invisibility cloak using metamaterials made of stacked positive and negative index slabs," *Journal of Applies Physics*, vol. 113, no. 16, 2013.
- [77] S. Palit, T. Driscoll, T. Ren and J. Mock, "Towards artificial magnetism using THz split ring resonator meta materials," in *19th Annual Meeting of the IEEE Lasers and Electro-optics Society*, 2006.
- [78] S. Linden, C. Enkrich and G. Dolling, "Photonic metamaterials; magnetism at optical frequencies," *Journal of Selected Topics in Quantum Electronics*, vol. 12, no. 6, 2006.
- [79] J. Zhou, T. Koschny and C. M. Soukoulis, "Magnetic and electric excitations in split-ring resonators," *Optics Express*, vol. 15, no. 26, 2007.

- [80] D. R. Smith, D. C. Vier, T. Koschny and C. M. Soukoulis, "Electromagnetic parameter retrieval from inhomogeneous metamaterials," *Physics Rev. E*, vol. 71, no. 3, 2005.
- [81] Z.-G. Liu, Z.-C. Ge and X.-Y. Chen, "Research Progress on Fabry-Perot resonator antenna," *Journal of Zhejiang University*, vol. 10, no. 4, pp. 583-588, 2009.

# VITAE

- Farooq Sultan
- Born in Dammam, Saudi Arabia on 30<sup>th</sup> July, 1986
- Nationality: Pakistani
- Received B.S. in Telecommunications Engineering from COMSATS Institute of Information Technology (CIIT) in August 2008
- Completed M.S. in Telecommunications Engineering from King Fahd University of Petroleum and Minerals (KFUPM), Dhahran, Saudi Arabia in January 2011
- Completed Ph.D. in Electrical Engineering from King Fahd University of Petroleum and Minerals (KFUPM), Dhahran, Saudi Arabia in December 2014
- Published 5 ISI listed journal papers along with 11 conference papers
- Owns the rights to 3 US patents in the domains of wireless sensor networks and antennas
- Held the Chair position at IEEE KFUPM Student Section – from Dec. 2013 to Dec. 2014
- E-mail: [farooqstn@hotmail.com](mailto:farooqstn@hotmail.com)
- Phone: 0561505634
- Present Address: KFUPM Box 1661, Dhahran 31261, Saudi Arabia
- Permanent Address: House No. 81, Street 35A, Sector I-9/4, Islamabad 44000, Pakistan